

**Application of Electron Energy-Loss
Spectroscopy
to
Ferroelectric Thin Films**

Dissertation

zur Erlangung des akademischen Grades
doctor rerum naturalium (Dr. rer. nat.)

vorgelegt der
Mathematisch-Naturwissenschaftlich-Technischen Fakultät
(mathematisch-naturwissenschaftlicher Bereich)
der Martin-Luther-Universität Halle-Wittenberg

von Herrn
Jingmin Zhang

geb. am 12.08.1973 in Shandong, China

Gutachter:

1. PD Dr. Hartmut S. Leipner, Martin-Luther-Universität, Halle
2. PD Dr. Dietrich Hesse, Max-Planck-Institut für Mikrostrukturphysik, Halle

verteidigt am 16.12.2004

Halle (Saale), December 2004

urn:nbn:de:gbv:3-000007663

[<http://nbn-resolving.de/urn/resolver.pl?urn=nbn%3Ade%3Agbv%3A3-000007663>]

Abstract

High-resolution electron energy-loss spectroscopy (HR-EELS) and scanning transmission electron microscopy (STEM) have been applied to investigate BaTiO₃/SrTiO₃ ferroelectric multilayers and high- κ gate dielectric Y₂O₃/Si(001). The experiments are mainly concentrated on interface reactions and interface defects. The preparation of the STEM specimens and various experimental parameters which have strong effects on the acquisition of electron energy-loss spectra from the interface are discussed.

In BaTiO₃/SrTiO₃ multilayers, oxygen vacancies have been found to preferably aggregate at the rough upper interface (SrTiO₃/BaTiO₃) while the lower interface (BaTiO₃/SrTiO₃) is nearly defect free. This finding has been explained in terms of misfit strain and oxygen vacancy ordering. The space charges formed by the aggregation of oxygen vacancies decrease the dielectric constant of ferroelectric multilayers. The crystal splitting of the Ti L₂₃ edges is revealed to sensitively reflect the misfit strains. The lattice parameters of the BaTiO₃ thin layer have been determined by selected-area electron diffraction, which confirm the presence of the strong misfit strains.

In the high- κ gate dielectric Y₂O₃/Si(001), the interfacial SiO_{*x*} ($1 \leq x \leq 2$) layer and yttrium silicates formed by interface reactions between the deposited Y₂O₃ film and the silicon substrate have been investigated by HR-EELS. The interfacial SiO_{*x*} layer is nearly pure amorphous SiO₂, which is attributed to the silicon oxidation at the initial stage of the deposition. Yttrium silicates are revealed to form at the Y₂O₃/SiO₂ interface. The formation of yttrium silicates is interpreted by direct chemical reactions between the deposited Y₂O₃ film and the interfacial SiO₂. Additionally, electron beam induced diffusion of SiO₂ is found to form yttrium silicates. According to the results of EELS and HRTEM, the possible interpretation is given in this work. The formation of yttrium silicates has been confirmed by the full multiple-scattering (FMS) calculations. The orientation relationships between the Y₂O₃ film and the silicon substrate are interpreted in terms of surface free energy and lattice match.

The band-structure and full multiple-scattering methods have been combined to interpret the electron energy-loss near-edge structures (ELNES) of the ceramics involved in this thesis, including SiO₂, TiO₂, SrTiO₃, BaTiO₃, Y₂O₃, Y₂SiO₅, and Y₂Si₂O₇. The ligand-field atomic multiplet method is also briefly discussed to interpret the white-line structures in the transition-metal compounds. The theoretical calculations have been concentrated on the Ti L₂₃, Y M₄₅, Si L₂₃ edges, and especially the O K edge. In comparison with the measured electron energy-loss (EEL) spectra, the main features of these core-loss edges have been reproduced fairly well by the Ab-Initio calculations. The combination of these different Ab-Initio methods gives the clear relationships between the EEL fine structures and the atomic microstructures around the absorbing atom. The theoretical calculations reveal that the low-energy features of the EEL core-loss spectrum are dominated by cation-oxygen interactions in a short range, and the high-energy features are interpreted by oxygen-oxygen interactions in a relative long range.

Zusammenfassung

Das Ziel der vorliegenden Arbeit war die Untersuchung von ferroelektrischen BaTiO₃/SrTiO₃ Mehrschichtsystemen und von Schichtsystemen aus 'high- κ ' Gate-Dielektrika Y₂O₃/Si(001) mittels hoch aufgelöster Elektronenenergieverlustspektroskopie (HR-EELS) in Verbindung mit Rastertransmissionselektronenmikroskopie (STEM). Der Fokus der durchgeführten Experimente und zugehörigen Simulationen lag dabei auf dem Studium der Reaktionen an den Grenzflächen der Schichtstrukturen und der Auswirkung von Defekten auf die Elektronenenergieverlustspektren (EEL-Spektren). Daneben wird auch der Einfluss der STEM Probenpräparation sowie verschiedener experimenteller Parameter bei der Spektrenaufnahme diskutiert.

In BaTiO₃/SrTiO₃ Mehrschichtsystemen konnten Sauerstoffleerstellen nachgewiesen werden, die bevorzugt an der oberen raueren Grenzfläche (SrTiO₃/BaTiO₃) agglomerieren, während die untere Grenzfläche (BaTiO₃/SrTiO₃) nahezu defektfrei ist. Dieses Verhalten wird durch lokal unterschiedliche Verzerrungen innerhalb der Schichten hervorgerufen. Die Raumladung, die durch die Leerstellenagglomerate entsteht, vermindert die Dielektrizitätskonstante der ferroelektrischen Schichtsysteme. In den EEL-Spektren spiegelten sich die internen Gitterverzerrungen in einer Änderung der Kristallfeldaufspaltung der Ti L₂₃ Ionisationskante wider. Die Gitterkonstante der BaTiO₃-Schichten wurde über lokale Elektronenbeugung bestimmt. Dabei konnte das Vorhandensein der starken internen Verzerrungen bestätigt werden.

Bei den Y₂O₃/Si(001)-Schichtsystemen bilden sich durch die Oxidation des Siliziums zu Beginn des Y₂O₃-Schichtwachstums eine SiO_x ($1 \leq x \leq 2$) Grenzflächenschicht sowie zusätzlich durch Grenzflächenreaktionen Yttriumsilikate. Bei der Untersuchung dieses komplexen Grenzflächensystems mittels HR-EELS ergab sich, daß die SiO_x-Grenzflächenschicht nahezu vollständig aus amorphem SiO₂ besteht. Die sich an der Grenzfläche zwischen diesem amorphen SiO₂-Film und dem darauf abgeschiedenen Y₂O₃ durch chemische Reaktion erzeugten Yttriumsilikate konnten nachgewiesen und charakterisiert werden. Zusätzlich wurde - sowohl bei den EELS als auch bei den HRTEM-Experimenten - eine Bildung von Yttriumsilikat durch die elektronenstrahlinduzierte Diffusion von SiO₂ beobachtet. Die Änderung in den EEL-Spektren bei der Silikatbildung wurde durch Berechnungen mit der 'full multiple-scattering'-Methode reproduziert.

Zur Interpretation der kantennahen Feinstruktur der Ionisationskanten (ELNES) wurden die Ergebnisse von elektronischen Bandstrukturrechnungen und Vielfachstremethoden miteinander verknüpft. Die theoretischen Rechnungen und Simulationen konzentrierten sich dabei auf die Ti L₂₃, Y M₄₅, Si L₂₃ Kanten sowie insbesondere die O K Kante der untersuchten Keramiken: TiO₂, SrTiO₃, BaTiO₃, Y₂O₃, Y₂SiO₅, Y₂Si₂O₇ und SiO₂. Zur Diskussion der 'white-line' Strukturen in den Spektren der Übergangsmetallverbindungen wurde zusätzlich die 'ligand-field atomic multiplet'-Methode eingesetzt. Auf diese Weise ließen sich in den Simulationen die charakteristischen Peaks der gemessenen Energieverlustspektren im Allgemeinen gut reproduzieren. Die Kombination der verschiedenen ab-initio Methoden ermöglicht damit die Herstellung klarer Zusammenhänge zwischen der EEL-Feinstruktur und der atomaren Mikrostruktur in der Umgebung des jeweilig angeregten Atoms. Dabei zeigte sich, daß der Verlauf der ELNES-Spektren direkt oberhalb der Absorptionskanten von den Kation-Sauerstoff Wechselwirkungen dominiert ist, während die Intensitätsmodulationen bei höheren Energieverlusten durch Sauerstoff-Sauerstoff-Wechselwirkungen bestimmt werden.

Contents

1	Introduction	1
2	Theory of Ab-Initio Methods to Simulate ELNES	4
2.1	Multiple-Scattering Method	5
2.2	Band-Structure Method	15
2.3	Ligand-Field Atomic Multiplet Method	18
2.4	Comparison of Different Calculation Methods	21
3	Details of EELS Experiments	28
3.1	EELS/STEM Instruments	28
3.2	Specimen Preparation	30
3.2.1	General Procedures	30
3.2.2	High Quality EELS Specimens with Interfacial Structures	31
3.3	Acquiring Spectra from Interfaces	32
3.3.1	Spatial Resolution	32
3.3.2	Convergence Angle	35
3.3.3	Collection Angle	36
3.3.4	Beam Stability	37
3.3.5	Spatial Drift	39
3.3.6	Ghost Features	39
3.3.7	Orientation of the Interface	39
4	HR-EELS Investigation of BaTiO₃/SrTiO₃ Multilayers	42
4.1	Introduction	42
4.2	Experiment	43
4.3	Results and Discussion	43
4.3.1	Ti L ₂₃ Edges	44
4.3.2	O K Edge	49
4.3.3	[Ti]/[O] Ratio	51
4.4	Explanation of Fine Structures of the O K Edge	52
4.4.1	Bulk SrTiO ₃	52
4.4.2	Bulk BaTiO ₃	58
4.5	Summary	62
5	Y₂O₃ Films on Si (001) Substrate	64
5.1	Introduction	64
5.2	Experiments	64
5.3	Results and Discussions	65
5.3.1	Si L ₂₃ Edges	67
5.3.2	Y M ₄₅ Edges	71
5.3.3	O K Edge	71

5.4	Electron Beam Induced Chemical Reactions	74
5.5	FMS Calculations of Yttrium Silicates	76
5.6	Ab-Initio Calculations of Y_2O_3	79
5.6.1	Y M_{45} Edges	81
5.6.2	O K Edge	83
5.7	Summary	85
6	Summary and Conclusion	87

Acronyms and Symbols

BS	Band structure
BST	(Ba,Sr)TiO ₃
BTO	BaTiO ₃
CCD	Charge-coupled device
CFEG	Cold field emission gun
CI	Configuration interaction
DFT	Density functional theory
DOS	Density of states
DRAM	Dynamic random-access memory
EEL	Electron energy-loss
EELS	Electron energy-loss spectroscopy
EFTEM	Energy-filtered TEM
ELNES	Electron energy-loss near-edge structures
EXAFS	Extended X-ray absorption fine structures
EXELFS	Extended energy-loss fine structures
FLAPW	Full-potential linearized-augmented plane-wave
FEG	Field emission gun
FIB	Focused ion beam
FMS	Full multiple-scattering
FWHM	Full width at half maximum
GGA	Generalized gradient approximation
HF	Hartree-Fock
HR-EELS	High-resolution electron energy-loss spectroscopy
HRTEM	High-resolution TEM
IBZ	Irreducible Brillouin zone
KKR	Korringa-Kohn-Rostoker
LDA	Local density approximation
<i>l</i> DOS	<i>l</i> -projected density of states
LDOS	Local density of states
LFAM	Ligand-field atomic multiplet
LO	Local orbitals
LSDA	Local spin density approximation
LSW	Localized spherical wave
MFP	Mean free path
MOS	Metal-oxide semiconductor
MOSFETs	Metal-oxide-semiconductor field-effect transistors
MS	Multiple-scattering
MT	Muffin-tin
NES	Near-edge structures
OLCAO	Orthogonalized linear combinations of atomic orbitals
PLD	Pulsed laser deposition

PIPS	Precision ion polishing system
RDF	Radius distribution function
ROA	Radius of objective aperture
RUM	Rigid unit mode
SCF	Self-consistent-field
STEM	Scanning transmission electron microscopy
STO	SrTiO ₃
TEM	Transmission electron microscopy
XAS	X-ray absorption spectroscopy
YAG	Yttrium aluminum garnet
$\mathcal{H}, \mathcal{K}, \mathcal{L}$	Miller indices of crystallographic planes
a, b, c, β'	Lattice parameters of crystal structure
κ	Dielectric constant
l, m	The angular momentum and magnetic quantum numbers
L ₂₃	L ₂₃ edges
M ₄₅	M ₄₅ edges
\hbar	Planck's constant
E	Energy loss
E_i	Initial state energy
E_f	Final state energy
E_F	Fermi energy
E_0	Incident beam energy
E_{xc}	Exchange-correlation energy function
$\mu(E)$	Transition rate from initial to final states
$\mu_0(E)$	Absorption background of the near-edge fine structures
ψ_i	Wave function of the initial state
ψ_f	Wave function of the final state
$\psi_j(\mathbf{r})$	Wave function of the j th electron
ϵ	X-ray polarization vector
\mathbf{r}	Distance to the atomic center
χ	Normalized oscillatory part of EXAFS
k	Wave number
δ	Phase shift of the photoelectron wave
δ_c	Phase shift constant related to the central atom
δ_l	Phase shift of l -component electron wave
θ, ϕ	Latitudinal and longitudinal coordinates
ξ	Constant coefficient of the phase shift
$f(k), f(\theta)$	Backscattering amplitude
R_j	Radius of the j th shell
N_j	Number of atoms in j th shell
λ	Mean free path
σ_j^2	Debye-Waller factor
$j_l(kr)$	Spherical Bessel function
$P_l(\cos \theta)$	Legendre polynomial

$h_l^{(1)}(k\mathbf{r})$	First kind of Hankel function
$h_l^{(2)}(k\mathbf{r})$	Second kind of Hankel function
e	Electron charge
m_e	Electron mass
$\lambda(k)$	Energy-dependent mean free path
F_{eff}	Effective scattering amplitude
ξ	Bond vector
$\rho(E)$	Charge density
i, j	Index number
I_0	Intensity of the incident beam
Γ	Net lifetime of the photoelectron
$\epsilon_{xc}(\rho)$	Exchange-correlation energy for the electron-gas system
μ	Chemical potential
ϵ_j	Energy eigenvalue of the j th state
\mathbf{K}_n	n th reciprocal lattice vector
$u_l(r, E_l)$	Radial solution of Schrödinger equation
$\sigma(E)$	Absorption cross-section
O_h	Octahedral symmetry
D_{4h}	Tetrahedral symmetry
e_g	e_g orbitals
t_{2g}	t_{2g} orbitals
q	Charge transfer
t, T	Scattering matrix
t_0	Thickness of the specimen
t'	Thickness of the interface layer
G_0	Green's function of the free electron wave propagator
G_c	Green's function of the propagator at the central atom
G_{sc}	Green's function of the scattering propagator
$s\text{DOS}$	s -projected partial DOS
$p\text{DOS}$	p -projected partial DOS
$d\text{DOS}$	d -projected partial DOS
$f\text{DOS}$	f -projected partial DOS
Dq, ds, dt	Crystal field parameters
α	Convergence semiangle
β	Divergence semiangle
ϑ	Tilt angle of the interface
d	Spatial resolution
d_0	Probe diameter
d_{max}	Maximum of the probe diameter
L_0	Intensity profile width
h	Distance from the objective aperture to the specimen
R_{nm}	Norman radius
R_{OA}	Radius of objective aperture
S	Sensitive volume ratio

S_{\max}	Maximum of the sensitive volume ratio
$v(\mathbf{r})$	External potential
$Y_{lm}(\theta, \phi)$	Spherical harmonics
Z	Atomic number

Chapter 1

Introduction

The integration densities of dynamic random-access memory (DRAM) and metal-oxide semiconductor (MOS) have increased by a factor of two every couple of years during the past three decades, and this trend continues today. High integration requires a nanosize of the dielectric units. Thin films and multilayers are suitable for this purpose since a sufficiently high electric field can be achieved by a relative low voltage. Many new techniques for depositing thin films on certain substrates have been developed in recent years. Among them, pulsed laser deposition (PLD) and ion beam sputtering are widely used. Generally, the ideal thin films should be defect-free since the defects always lead to a decreased dielectric permittivity. Even though high-quality ceramic thin films might be obtained through carefully optimized oxygen partial pressure, substrate temperature, annealing process, as well as other parameters like deposition rate, the general growth mechanism and the effect of defects in thin films are not yet clear. On the other hand, in many existing materials the dielectric properties of thin films are significantly different from those of bulk materials due to the effects of nanoscale dimensions, interface states, vacancies, and stress-strain conditions. In order to grow high-quality thin films, investigations of those conditions are very important.

Higher capacitance of DRAMs can be achieved by thinner capacitor dielectrics and higher-permittivity capacitor dielectric materials. Thin films of barium-strontium titanate (Ba,Sr)TiO₃ (BST) have been investigated for use as a capacitor dielectric for future generations of DRAMs because its high permittivity is in the range 200-350. Nevertheless, grain boundaries result in a significant leakage current as the thickness of the thin film is decreased. One possible solution is BaTiO₃/SrTiO₃ multilayers. Two possible orientation relationships between the BaTiO₃ thin film and the SrTiO₃ substrate were found: BaTiO₃ (001) || SrTiO₃ (001), BaTiO₃ [100] || SrTiO₃ [100]; or, BaTiO₃ (100) || SrTiO₃ (001), BaTiO₃ [001] || SrTiO₃ [100]. Previously, the exact orientation relationship has not been given because the limited resolution of the diffraction pattern makes it difficult to resolve the tetragonality of the BaTiO₃ lattice, i.e., to differentiate between [h00] and [00l] BaTiO₃ reflections [1]. Due to the very similar lattice parameters (BaTiO₃, $a=3.994$ Å, $c=4.038$ Å; SrTiO₃, $a=3.905$ Å), defect-free BaTiO₃ thin films can be deposited on a SrTiO₃ substrate up to a critical thickness of 5-6 nm by the PLD technique [1, 2]. This defect-free thin layer has been roughly explained by the misfit strain induced by the small misfit at the interface. However, the lattice parameters of the BaTiO₃ thin layer are not yet given. Moreover, although the dielectric constant linearly decreased with the decreasing thickness of BaTiO₃/SrTiO₃ multilayers [1], the physical mechanism is not yet clear.

Silicon dioxide has been used for more than 30 years as a gate dielectric for metal-oxide-semiconductor field-effect transistors (MOSFETs) since the SiO₂/Si material system was first applied in the 1970s. The lateral dimensions of the MOSFETs have been reduced from 10 μm to the present size of 90 nm. Ultrathin (1.2 nm) SiO₂ gate dielectric has been successfully implemented at today's 90 nm process node [3], and a 0.8 nm thick SiO₂ gate oxide has

already been prepared in the laboratory [4]. However, low- κ SiO₂ (permittivity $\kappa=3.9$) used as gate dielectric almost reaches its physical limits (leakage current, thermal stability, etc.). As MOS scales to this point, the traditional silicon dioxide gate dielectric becomes only four atomic layers thick. Tunneling current leakage and the resulting increase in power dissipation and heat become critical issues. Further gate dielectric scaling requires high- κ materials as replacements for SiO₂. Yttrium oxide has recently attracted more attention due to its high dielectric constant ($\kappa=14-18$), thermal stability and small lattice misfit with respect to silicon substrate [5]. Si (001) substrate is usually chosen in the standard silicon technology. The reduction of tunnel current is much more pronounced with high- κ dielectrics, especially for those with barrier heights slightly greater than the supply voltage. To reduce the leakage current and the thickness of gate dielectrics, the applicable high- κ dielectrics should be defect-free and have a sharp interface with the silicon substrate. Most of the experiments and discussions focused on two critical problems: (1) oxygen defects in as-deposited Y₂O₃ films; (2) interface reactions, i.e., chemical reactions at the interface between Y₂O₃ film and silicon substrate. The major defects in as-deposited Y₂O₃ thin film are oxygen vacancies. This is the reason why the deposition process needs to be performed under appropriate oxygen or oxygen ion environment in order to achieve stoichiometric (or oxygen-defect-free) Y₂O₃ thin films [6]. Subsequently a post-deposition annealing is performed for reducing the defects in the as-deposited films in vacuum or under certain ambient conditions. An interface layer between the deposited yttria thin film and the silicon substrate is always found in previous investigations, even though a lower substrate temperature was used and the oxygen partial pressure was kept low. Similar reactions can be found in most of the metal oxides deposited on Si substrate, such as Gd₂O₃ [7], La₂O₃ [8], Ta₂O₅ [9], etc. The thickness of the interface layer varies with experimental conditions, such as oxygen partial pressure, pretreatment of the silicon substrate, and post-deposited annealing process. Because the interface layer has a lower- κ than that of the Y₂O₃ film, this layer is usually unwanted. The control and optimization of the interface layer become very important prior to substitution of SiO₂ gate dielectrics. The chemical composition of the interface layer was revealed to be SiO_{*x*} ($1 \leq x \leq 2$) [10] and yttrium silicates [11, 12, 13]. However, those investigations were based on the HRTEM image [11, 13] or X-ray diffraction [12]. Straightforward techniques need to be applied to analyze the chemical composition of the interface layer. Although a few papers have reported investigations of Y₂O₃/Si structures by electron energy-loss spectroscopy (EELS) [14, 15, 16], a lower energy resolution was used, and only the Si L₂₃ edges have been discussed at the interface. No systematic investigations have been carried out. That makes the formation mechanism of the interface layer still a subject to dispute.

The electron energy-loss spectrum is sensitive to the bond length, coordinations, vacancies, and crystal symmetries. The change of atomic structure around the excited atoms will be reflected in the variation of fine structures in the EEL spectrum. Due to the nanosize of thin films, the electron energy-loss spectrometer coupled with a scanning transmission electron microscope is becoming an important nanoanalytical technique in these materials. Due to an identical underlying physical mechanism (the excitation of core electrons into unoccupied states) as in X-ray absorption spectroscopy (XAS), EELS can be used as a complementary technique, especially in the low-energy region (< 2000 eV), i.e., EELS has similar abilities as soft XAS. But the most promising advantages of EELS/STEM are the nanosize probe and the high intensity of the signals by comparison to XAS or EELS in a conventional transmission electron microscope. Therefore, EELS/STEM has been widely used for investigations of electric properties and chemical composition in nanoscale regions, such as interfaces [17, 18, 19], grain boundaries [20, 21, 22], and dislocation cores [23, 24].

In this thesis, both BaTiO₃/SrTiO₃(001) multilayers and high- κ Y₂O₃/Si(001) dielectrics are investigated systematically by high-resolution EELS/STEM, HRTEM, and Ab-Initio calculations. The works mainly concentrate on effects of misfit strain, oxygen vacancies and interface reactions. The relationship between atomic structures and the fine structures of EEL spectra will be elucidated by Ab-Initio calculations in comparison with the experimental

results. Firstly, the theoretical background of Ab-Initio methods is briefly introduced in **Chapter 2**. The comparison between different Ab-Initio methods is given by calculating the Ti L_{23} and O K edges of rutile TiO_2 . Secondly, due to the challenging problems (mainly related to the interfaces) presented in the EELS experiments for such brittle and insulating specimens, **Chapter 3** describes and discusses the details of the experimental procedures including the preparation of STEM specimens. In **Chapter 4**, HR-EELS investigation of $BaTiO_3/SrTiO_3(001)$ multilayers is discussed. The determination of the lattice parameters of the $BaTiO_3$ layers as well as the orientation relationship between the $BaTiO_3$ layer and the $SrTiO_3$ substrate is established. Then, the fine structures of the Ti L_{23} edges and the O K edge are discussed across the $BaTiO_3/SrTiO_3$ interface. The influence of misfit strain and the aggregation of oxygen vacancies will be addressed. Successively, the fine structures of the O K edge in $SrTiO_3$ and $BaTiO_3$ are interpreted by the FMS and band-structure calculations. The experimental and theoretical results of high- κ $Y_2O_3/Si(001)$ dielectric structures are presented in **Chapter 5**. The experimental results from the Si L_{23} , Y M_{45} and O K edges across the interface layer are illustrated. The chemical composition and the formation mechanism of the interface layer are discussed. The evidences of yttrium silicates formed at the Y_2O_3/SiO_2 interface will be given by the experimental Si L_{23} and O K edges and the theoretical calculations. The electron-beam-induced chemical reactions are investigated by EELS and HRTEM. The possible interpretation will be given in this chapter. Again, Ab-Initio simulations are given for the Y M_{45} and O K edges in bulk Y_2O_3 . Clear interpretations of those fine structures are given by the excellent simulations. Summary and conclusions are given in **Chapter 6**.

Chapter 2

Theory of Ab-Initio Methods to Simulate ELNES

The extended fine structure, that appears on the high-energy side of X-ray absorption edge (Extended X-ray absorption fine structure, EXAFS), had ever tantalized physicists for many years [25]. The first observation of a complicated structure in absorption edges was reported by Fricke (1920) who worked on the K edges of Mg, Fe and Cr compounds [26]. The first reasonable theoretical explanation for the EXAFS in crystalline solids was proposed by Kronig in 1931 [27]. Kronig's theory predicts that the absorption energy extremities occurring in cubic crystals are proportional to $(\mathcal{H}^2 + \mathcal{K}^2 + \mathcal{L}^2)/a^2$ where $\mathcal{H}, \mathcal{K}, \mathcal{L}$ are the Miller indices of crystallographic planes, a is the lattice parameter. This suggests that a relation between the X-ray absorption process and a diffraction phenomenon obeying Bragg's law exists. Bragg reflections of the ejected electrons are responsible for oscillations of fine structures which would be a monotonic absorption curve for a isolated atom. The main features of EXAFS in solids could be explained by the distribution of density of states which is modulated by the allowed and forbidden transition probabilities. This is referred to "long-range order theory" in the literature. In the latter extension of his long-range theory, Kronig considered the case of a small molecule and assumed that the ejected electrons were scattered by the neighboring atoms [28]. By suitably combining the wave functions of the initial and final states, he showed how the transition probabilities can be calculated. It is the so-called "short-range order theory" in the literature. Thus, Kronig suggested that the EXAFS can be explained in two somewhat different ways by considering variations in the unoccupied density of states (DOS), or by calculating the transition probabilities between the initial and final states of photoelectrons scattered by neighboring atoms.

The multiple-scattering method is derived from Kronig's short-range order theory. It has undergone a very long way from the single-scattering theory to currently full multiple-scattering theory. The band-structure (BS) method is derived from Kronig's long-range order theory. Especially in the case of K edge structures of ceramics, l -projected density of states (l DOS) is usually compared with the ELNES directly because only the $s \rightarrow p$ transition is allowed according to the dipole selection rule. Since the multiple-scattering (MS) and BS methods neglect the multiplet effects which dominate the profile of white-line structures in ELNES of transition-metal elements, the ligand-field atomic multiplet (LFAM) method is also briefly described. The term "white-line" indicates the sharp fine structures in the transition-metal element L_{23} edges just several eVs above the threshold energy. In this thesis, the dipole selection rule is always adopted in the calculations because the high energy of used electron beam (100 keV) guarantees the validity of this rule [29].

2.1 Multiple-Scattering Method

Most of the multiple-scattering codes are based on muffin-tin (MT) approximation: the potential inside the muffin-tin sphere is spherical as the atomic-like potential, and the potential in the interstitial region (muffin-pan) between the muffin-tin spheres is flat and constant. The shape of potential is called “muffin-tin potential”. The muffin-tin radius is determined by the spatial integration of electron density to the number of electrons.

2.1.1 Point-Scattering Approximation

Before the 1970s, a confusion over the short range vs. the long range order nature of EXAFS persisted until Sayers and Stern reported a point-scattering theory in 1971, which gave an excellent agreement with the experimental structure [30]. In their point-scattering theory, the excited photoelectron was treated as a spherical wave which propagates in the lattice and is partially scattered by neighbors of the excited atom. The neighboring atoms are treated as point scatterers and the total scattered wave is summed from the waves scattered by each atom. According to the perturbation theory, the effect of incident particles can be considered as a perturbation hamiltonian which contributes to the excitation from initial to final states. The transition rate in the dipole approximation is given by the Golden Rule,

$$\mu(E) = \frac{2\pi}{\hbar} \sum_f |\langle \psi_f | \boldsymbol{\epsilon} \cdot \mathbf{r} | \psi_i \rangle|^2 \delta(E + E_i - E_f), \quad (2.1)$$

where E is the energy loss, E_i the initial state energy, E_f the final state energy, ψ_f the wave function of the final state, ψ_i the wave function of the initial state, and $\boldsymbol{\epsilon}$ the X-ray polarization vector, \hbar the Planck’s constant, \mathbf{r} the distance to the atomic center. The summation is over all of the final states. If the atom is isolated, the final state is a simple outgoing wave, and the EXAFS should be a smooth function $u_0(E)$ of the photon energy above the threshold energy. In a solid the final state results from the interference between the backscattering waves and the outgoing wave. The normalized oscillatory part of EXAFS is expressed

$$\chi(E) = \frac{\mu(E) - \mu_0(E)}{\mu_0(E)}. \quad (2.2)$$

Sayers, Stern and Lytle derived the above equation with the basic assumptions: (1) The outgoing wave can be approximated by $[-ie^{ikr+\delta(k)}/kr]Y_{lm}(\theta, \phi)$, where $-i$ is responsible for sine waves instead of cosine waves, k the wave number of the photoelectron, $Y_{lm}(\theta, \phi)$ the spherical harmonics, and θ the polar (latitudinal) coordinate, and ϕ the azimuthal (longitudinal) coordinate. This assumption is necessary to ensure that the phase shift δ equals to zero in a isolated atom. (2) The radius of the excited atom is neglected, i.e., the outgoing wave at the neighboring atom position can be approximated to a plane wave. (3) Only single scattering by the surrounding atoms is considered. (4) The phase shift δ is a linear function of the photoelectron wave number, i.e., $\delta(k) = \eta k + \delta_c$ where η is the constant coefficient and δ_c the constant related to the central atom. Then the final expression with these assumptions is given [31],

$$\chi(k) = \sum_j \frac{N_j f(k)}{R_j^2} e^{-R_j/\lambda} e^{-2\sigma_j^2 k^2} \sin[2kR_j + 2\delta(k)], \quad (2.3)$$

where $f(k)$ is the backscattering amplitude, R_j the distance from the absorbing atom to the j th coordination shell, N_j the number of atoms in j th shell, λ the mean free path, and $e^{-2\sigma_j^2 k^2}$ is a general Debye-Waller factor, where σ_j^2 is the mean square amplitude of the relative displacement of the atoms in j th shell with respect to the absorbing atom including thermal and disorder contributions. The summation is over all of the atom shells with

different R_j . Up to date, the EXAFS is theoretically recognized to be a measure of short-range order involving scattering from neighboring atoms. The experimental evidence for the success of short-range order theory is that the strong oscillations can be observed in amorphous samples.

2.1.2 Spherical-Wave Approximation

Lee and Pendry relaxed the assumptions (1), (2) and (3) mentioned above and proposed a spherical-wave theory [32]. Many-body effects were included via a self-energy correction to the Green's function. The most important is that the spherical-wave theory takes into account the finite size of the central atom. The incident wave (along quantization z-axis) can be expanded as a sum of component waves,

$$e^{ikz} = e^{ikr\cos\theta} = \sum_{l=0}^{\infty} (2l+1) i^l j_l(kr) P_l(\cos\theta), \quad (2.4)$$

where $j_l(kr)$ is the spherical Bessel function, $P_l(\cos\theta)$ the Legendre polynomial. After scattered by the neighboring atom, each component wave yields a phase shift δ_l due to the interaction with the central-force potential. Then the total scattering amplitude is given by

$$f(\theta) = \frac{1}{k} \sum_{l=0}^{\infty} (2l+1) e^{i\delta_l} P_l(\cos\theta) \sin\delta_l. \quad (2.5)$$

Within one-electron and muffin-tin approximations, the l -component phase shift δ_l can be calculated by assuming the core-hole absolutely screened by conduction electrons. The core state wave functions are normalized to the number of core electrons inside the muffin-tin sphere, while the charge density is represented as a uniform distribution in the interstitial region with keeping the atom neutral [33]. The photoelectron also distorts the conduction and valence states since it can also excite plasma modes. This results in a complex correlation self-energy correction. The real part causes an energy shift to the high-energy side, and the imaginary component of this correction produces a broadening of the spectrum. Both the real and imaginary parts depend on the energy of the photoelectron, but the energy dependence is weak and can be neglected.

The next step is to calculate the modification of the final state using the phase shifts. Assuming the excited atom at the origin of the coordinate system, the unperturbed final state is only an outgoing spherical wave described by

$$\psi_0(\mathbf{r}) = \sum_{l,m} A_{lm} h_l^{(1)}(k\mathbf{r}) Y_{lm}(\Omega(\mathbf{r})), \quad (2.6)$$

where $h_l^{(1)}(k\mathbf{r})$ is the the first kind of Hankel function, l and m the angular momentum and magnetic quantum numbers, $Y_{lm}(\Omega(\mathbf{r}))$ the spherical harmonics represented by the solid angle $\Omega(\mathbf{r})$ at \mathbf{r} , and A_{lm} the expansion coefficient. First, $\psi_0(\mathbf{r})$ is expanded about the surrounding atom's coordinations \mathbf{R}_j using spherical harmonics (denoted by the quantum numbers l'' and m'') if $|\mathbf{r} - \mathbf{R}_j| < |\mathbf{R}_j|$,

$$\psi_0(\mathbf{r}) = \sum_{l''m''} B_{l''m''} j_{l''}(k|\mathbf{r} - \mathbf{R}_j|) Y_{l''m''}(\Omega(\mathbf{r} - \mathbf{R}_j)), \quad (2.7)$$

where

$$B_{l''m''} = \sum_{l'm',lm} R_{l''m'',l'm'}^{lm} V_{l'm'}(\mathbf{R}_j) A_{lm}, \quad (2.8)$$

where the matrix

$$R_{l''m'',l'm'}^{lm} = 4\pi i^{l-l''-l''} (-1)^{m'+m''} \int Y_{lm}(\Omega(\mathbf{r})) Y_{l'm'}(\Omega(\mathbf{R}_j)) Y_{l''-m''}(\Omega(\mathbf{r} - \mathbf{R}_j)) d\Omega(\mathbf{r}), \quad (2.9)$$

and the vector

$$V_{l'm'}(\mathbf{R}_j) = h_{l'}^{(1)}(kR_j)Y_{l'-m'}(\Omega(\mathbf{R}_j)). \quad (2.10)$$

The spherical harmonics around \mathbf{R}_j is indicated by the quantum numbers l' and m' .

Once $\psi_0(\mathbf{r})$ is expanded as spherical waves about the atom at \mathbf{R}_j , the scattered wave $\psi_s^j(\mathbf{r})$ emanating from \mathbf{R}_j is obtained simply in terms of the scattering matrix $T_{LMl''m''}$

$$\psi_s^j(\mathbf{r}) = \sum_{LMl''m''} T_{LMl''m''} B_{l''m''} h_L^{(1)}(k|\mathbf{r} - \mathbf{R}_j|) Y_{LM}(\Omega(\mathbf{r} - \mathbf{R}_j)), \quad (2.11)$$

where L and M are the quantum numbers indicating the expansion of scattered wave around the atom at \mathbf{R}_j , the matrix

$$T_{LMl''m''} = \frac{1}{2} \delta_{Ll''} \delta_{Mm''} (e^{i2\delta_L} - 1). \quad (2.12)$$

Now $\psi_s^j(\mathbf{r})$ is an outgoing wave from the atomic position \mathbf{R}_j and can be expanded about the origin again

$$\psi_s^j(\mathbf{r}) = 2 \sum_{L''M''} C_{L''M''} j_{L''}(kr) Y_{L''M''}(\Omega(\mathbf{r})), \quad (2.13)$$

where the coefficient

$$\begin{aligned} C_{L''M''} &= V(-\mathbf{R}_j) S_{L'M',LM}^{L''M''} T_{LMl''m''} B_{l''m''} \\ &= \sum_{lm} V(-\mathbf{R}_j) S_{L'M',LM}^{L''M''} T_{LMl''m''} R_{l''m'',l'm'}^{lm} V_{l'm'}(\mathbf{R}_j) A_{lm}, \end{aligned} \quad (2.14)$$

where the matrix

$$S_{L'M',LM}^{L''M''} = 2\pi i^{L-L'-L''} (-1)^{M'+M''} \int Y_{LM}(\Omega(\mathbf{r} - \mathbf{R}_j)) Y_{L'M'}(\Omega(\mathbf{r})) Y_{L''-M''}(\Omega(\mathbf{r})) d\Omega(\mathbf{r}). \quad (2.15)$$

In above equations (2.11)-(2.15), the quantum numbers L , M , L' and M' indicate the expansion of the backscattering wave around the origin.

Summing over all of the neighboring atoms around the central atom, and defining a matrix

$$Z_{L''M'',lm} = \sum_j V(-\mathbf{R}_j) S_{L'M',LM}^{L''M''} T_{LMl''m''} R^{lm} V(\mathbf{R}_j), \quad (2.16)$$

then the coefficient $C_{L''M''}$ can be rewritten by

$$C_{L''M''} = \sum_{lm} Z_{L''M'',lm} A_{lm}. \quad (2.17)$$

More generally, we can think of a core electron in the initial state $|l_0 m_0\rangle$ making a transition to an outgoing wave $|l' m'\rangle$ via the dipole matrix $\langle l' m' | \mathbf{r} | l_0 m_0 \rangle$. The outgoing wave is scattered by the surrounding atoms resulting in an incoming wave $|lm\rangle$ about the absorbing atom. The amplitude of the backscattering wave is given by the $Z_{lm,l'm'}$ matrix, and coupled back to the core state by the matrix element $\langle l_0 m_0 | \mathbf{r} | lm \rangle$. The photoelectron suffers a phase shift of $e^{i\delta_{l'}}$ on its outgoing trip and $e^{i\delta_l}$ on its incoming trip. Therefore, the final expression of the absorption rate can be written

$$\begin{aligned} \mu(E) - \mu_0(E) &= \frac{2\pi}{\hbar} \left(\sum_{l_0 m_0} \langle l_0 m_0 | e \boldsymbol{\epsilon} \cdot \mathbf{r} | lm \rangle e^{i\delta_l} \right. \\ &\quad \left. \times Z_{lm,l'm'} e^{i\delta_{l'}} \langle l' m' | e \boldsymbol{\epsilon} \cdot \mathbf{r} | l_0 m_0 \rangle \right) \delta(E + E_i - E_f), \end{aligned} \quad (2.18)$$

where e is the electron charge.

If the above equation is divided by $u_0(E)$, the normalized oscillation of EXAFS within the dipole transition rule ($\Delta l = \pm 1, \Delta m = 0, \pm 1$) is obtained,

$$\chi(k) = \frac{2\text{Re}(\sum_{m_0} \sum_{lm'l'm'} P_{l_0m_0,lm} Z_{lm'l'm'} P_{l'm',l_0m_0} e^{i(\delta_l + \delta_{l'})})}{\sum_{m_0} \sum_{lm} |P_{l_0m_0,lm}|^2}, \quad (2.19)$$

where

$$P_{l_0m_0,lm} = \langle l_0m_0 | e\boldsymbol{\epsilon} \cdot \mathbf{r} | lm \rangle \quad (2.20)$$

is the dipole matrix element between the core state $|l_0m_0\rangle$ and the final state $|lm\rangle$.

For unpolarized excitation, by averaging over the diagonal elements of $Z_{lm,l'm'}$, the above equation simplifies to

$$\chi(k) = \frac{2}{3} \sum_{lm} \text{Re}(Z_{lm,lm} e^{i2\delta_l}). \quad (2.21)$$

Introducing the point-scattering approximation and assuming $kR_j \gg 1$, the outgoing and incoming waves can be approximated to plane waves. The simplified form of Eq. (2.21), including the thermal effect, results in the Sayers' point-scattering equation (2.3). Lee et al. compared the point-scattering approximation (plane-wave approximation) with the spherical-wave approximation [32]. They found that point-scattering approximation works well only if the photoelectron energy >100 eV and overestimates the amplitude of the backscattering waves at small k . In this thesis, for simplification Sayers' theory is classified as "plane-wave theory", and Lee's theory as "spherical-wave theory". In the last decade, a more accurate approximation named "curved-wave theory" was introduced into the simulation of the X-ray absorption fine structures by Rehr and Albers [34], which will be discussed later.

2.1.3 Multiple-Scattering Theory

Comparing the theoretical spectra (calculated by the spherical-wave method only including single-scattering events) to experimental results, Lee et al. found that the 4th peak had a reversed intensity in the radius distribution function (RDF) of copper [32]. The single-scattering theory can not explain this discrepancy. They extended the single-scattering theory to multiple-scattering theory within spherical-wave approximation and got an excellent agreement with the experiment for all of the features in the EXAFS region.

The photoelectron can be scattered by several atoms at $\mathbf{R}_j (j = 1 \cdots n - 1)$ before returning to the central atom. Both of \mathbf{R}_0 and \mathbf{R}_n are used to denote the coordinate of the central atom. The outgoing wave starts from \mathbf{R}_0 and finally is scattered back to \mathbf{R}_n . This process can be done by constructing the scattering matrix for each atomic shell with the same distance and then summing up all possible scattering shells. However, enumerating all of the possible scattering paths is rather cumbersome and inefficient [35]. Lee and Pendry introduced an effective radius for n -order scattering [32],

$$r_{\text{eff}} = \frac{1}{2} \sum_{j=0}^n |\mathbf{R}_{j+1} - \mathbf{R}_j|, \quad (2.22)$$

where the factor 2 indicates the photoelectron undergoing outgoing and incoming trips. All of the multiple-scattering paths are classified by r_{eff} . For each group with a same r_{eff} , it only a finite number of paths need to be considered within a finite radius around the central atom. The effective radius is cut at a certain value as the sum of the rest of paths converging to a negligible contribution.

The result can be summarized as an extension to the single-scattering matrix $Z_{lm,l'm'}$. The multiple-scattering matrix

$$Z_{lm,l'm'}^{\text{tot}} = \sum_{j=1}^{n-1} Z_{lm,l'm'}^j + \sum_{j=1}^{n-2} Z_{lm,l'm'}^{(j+1)j} + \cdots, \quad (2.23)$$

where $Z^{n \cdots (j+1)j}$ describes the scattering of the photoelectron by atoms at \mathbf{R}_j , \mathbf{R}_{j+1}, \dots , and finally back to the central atom at \mathbf{R}_n . The first term on the right-hand side of the equation is the single-scattering contribution, and the second term is the double-scattering contribution, and so on. The illustration of a double scattering by atoms at \mathbf{R}_j and \mathbf{R}_{j+1} is shown in Fig. 2.1. The amplitude of the electron wave is decreasing during the propagation.

The propagation of the photoelectron is described by a matrix K at the scatters and a matrix Q at the central atom. The scattering process around the scatters is described by a matrix T which contains the phase shift term caused by the scattering. The simplified definitions of these matrixes are given as,

$$\begin{aligned} Z_{lm,l'm'}^{n \cdots (j+1)j} &= Q(\mathbf{R}_n)T \cdots TK(\mathbf{R}_{j+1} - \mathbf{R}_j)TK(\mathbf{R}_j) \\ K_{lm'l'm'}(\mathbf{r}) &= \sum_{l''m''} R_{l''m''l'm'}^{lm} V_{l''m''}(\mathbf{r}) \\ Q_{lm'l'm'}(\mathbf{r}) &= \sum_{l''m''} V_{l''m''}(-\mathbf{r})S_{l''m''l'm'}^{lm} \\ T_{lm'l'm''} &= \frac{1}{2} \delta_{ll''} \delta_{mm''} (e^{i2\delta_l} - 1). \end{aligned} \tag{2.24}$$

In the case of unpolarized excitation, the Z matrix can be defined by the effective radius r_{eff} similar to

$$\tilde{Z}(r_{\text{eff}}) = \frac{1}{3} e^{-i2kr_{\text{eff}}} \sum_{\text{path}} \sum_m Z_{lm,lm}, \tag{2.25}$$

where the first sum is over all paths with the same r_{eff} .

In multiple-scattering theory, the single scattering dominates the primitive portion of the structures in the absorption spectrum, and the forward scattering refines the detailed structures as an additional correction. In some cases, the high-order (double, triple, ...) scatterings significantly change the fine structures of the spectrum since forward scattering introduces additional phase shifts, eg., the 4th shell of copper [32].

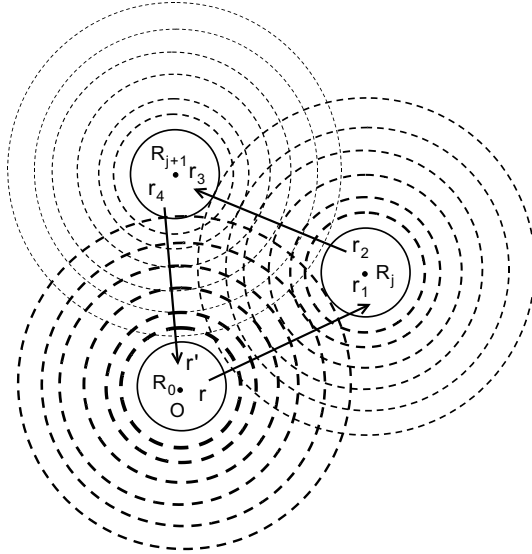


Fig. 2.1: Illustration of a double scattering by atoms at \mathbf{R}_j and \mathbf{R}_{j+1} . The central atom is located at \mathbf{R}_0 and \mathbf{R}_n . The thickness of circle stands for the amplitude of the scattering wave. The arrows indicate the propagating direction.

2.1.4 Green's Function Representation of Multiple-Scattering Expansion

The Green's function technique is very important for the multiple-scattering theory. It can naturally incorporate inelastic losses and other quasi-particle effects without the necessity of explicit calculations of wave functions. The outline of the calculation on the X-ray absorption coefficient $\mu(E)$ using Green's function is given in this section. In the real space, the Green's function formulation of final states is given by [36]

$$\begin{aligned} G(\mathbf{r}, \mathbf{r}', E) &= \sum_f G(\mathbf{r}, \mathbf{r}', V) \\ &= \sum_f \frac{\psi_f^*(\mathbf{r}')\psi_f(\mathbf{r})}{V - E_f + i\Gamma}, \end{aligned} \quad (2.26)$$

where ψ_f are the final states with energies E_f , and Γ a net lifetime of the electron including effects of extrinsic and intrinsic losses. This Green's function denotes that the electron wave propagates from \mathbf{r} to \mathbf{r}' in the total muffin-tin potentials $V = \sum_j v_j(\mathbf{r} - \mathbf{R}_j)$ where v_j is the single muffin-tin potential of the neighboring atom at \mathbf{R}_j . For effective calculations, except the excited atom the muffin-tin potentials of the same elements are approximated to a same distribution even for inequivalent atoms. This approximation is reasonable because only core electrons are included in the muffin-tin radius. The solid-state effect on core electrons is ignored as in pseudo-potential theory. The muffin-tin potential of the central atom is handled particularly with a core hole, and screening effects are taken into account. In the case of double scattering (cf. Fig. 2.1), the Green's function can be expanded in terms of the outgoing free propagator $G_0(\mathbf{r}_i, \mathbf{r}_{i+1})$,

$$\begin{aligned} G(\mathbf{r}, \mathbf{r}', V) &= G_0(\mathbf{r}, \mathbf{r}_1)T(\mathbf{r}_1, \mathbf{r}_2, V)G_0(\mathbf{r}_2, \mathbf{r}_3)T(\mathbf{r}_3, \mathbf{r}_4, V)G_0(\mathbf{r}_4, \mathbf{r}'), \\ G_0(\mathbf{r}_i, \mathbf{r}_{i+1}) &= -\frac{e^{ik|\mathbf{r}_i - \mathbf{r}_{i+1}|}}{4\pi k|\mathbf{r}_i - \mathbf{r}_{i+1}|}, \end{aligned} \quad (2.27)$$

where the matrix $T(\mathbf{r}_i, \mathbf{r}_{i+1}, V)$ contains the detail of scattering process caused by the total scattering potential V . \mathbf{r}_i denotes the scattering location in the muffin-tin spheres. Furthermore, the matrix $T(\mathbf{r}_i, \mathbf{r}_{i+1}, V)$ can be expanded as

$$T(\mathbf{r}_i, \mathbf{r}_{i+1}, V) = \sum_j t_j(\mathbf{r}_i, \mathbf{r}_{i+1}, v_j). \quad (2.28)$$

The summation is over all of the neighboring atoms. The scattering matrix $t_j(\mathbf{r}_i, \mathbf{r}_{i+1}, v_j)$ of the single muffin-tin potential v_j is given by

$$t_j(\mathbf{r}_i, \mathbf{r}_{i+1}, v_j) = v_j(\mathbf{r}_i)\delta(\mathbf{r}_i - \mathbf{r}_{i+1}) + v_j(\mathbf{r}_i)G_0(\mathbf{r}_i, \mathbf{r}_{i+1})v_j(\mathbf{r}_{i+1}). \quad (2.29)$$

The Green's function at the central atom with the scattering potential v_0 is introduced by

$$G_c(\mathbf{r}, \mathbf{r}') = \frac{\psi_c^*(\mathbf{r}')\psi_c(\mathbf{r})}{v_0 - \epsilon_k + i\Gamma}, \quad (2.30)$$

where the wave function of core state

$$\psi_c(\mathbf{r}) = \begin{cases} \sqrt{\frac{2\pi}{R}}\psi_0(\mathbf{r}) & (r < R_{\text{MT}}) \\ i^l \sqrt{\frac{1}{2R}}kY_{lm}(\Omega)[h_l^{(1)}(kr)e^{i\delta_l} + h_l^{(2)}(kr)e^{-i\delta_l}] & (r > R_{\text{MT}}), \end{cases} \quad (2.31)$$

where $h_l^{(1)}(kr)$ and $h_l^{(2)}(kr)$ are the first and second kinds of Hankel function. The wave function outside the muffin-tin radius R_{MT} is a stationary solution appropriate for a free

electron with energy $\epsilon_k = k^2/2m_e$ (m_e , the electron mass) which normalized within a large enough radius R . The phase shift δ_l is determined by matching the wave function $\psi_0(\mathbf{r})$ inside the muffin-tin sphere. Substituting $G(\mathbf{r}, \mathbf{r}', V)$ into Eq. (2.26), one obtains

$$\begin{aligned} G(\mathbf{r}, \mathbf{r}', E) &= G_c(\mathbf{r}, \mathbf{r}') + G_{sc}(\mathbf{r}, \mathbf{r}') \\ &= G_c(\mathbf{r}, \mathbf{r}') + \sum_j G_c(\mathbf{r}, \mathbf{r}_1) t_j(\mathbf{r}_1 - \mathbf{r}_j, \mathbf{r}_2 - \mathbf{r}_j) G_c(\mathbf{r}_2, \mathbf{r}') \\ &\quad + \sum_j G_c(\mathbf{r}, \mathbf{r}_1) t_{j+1}(\mathbf{r}_1 - \mathbf{r}_j, \mathbf{r}_2 - \mathbf{r}_j) G_0(\mathbf{r}_2, \mathbf{r}_3) t_j(\mathbf{r}_3 - \mathbf{r}_j, \mathbf{r}_4 - \mathbf{r}_j) G_c(\mathbf{r}_4, \mathbf{r}') + \dots \end{aligned} \quad (2.32)$$

For simplicity, we denote above equation as

$$\begin{aligned} G(\mathbf{r}, \mathbf{r}', E) &= G_c + G_{sc} \\ &= G_c + \sum_j G_c t_j G_c + \sum_j G_c t_{j+1} G_0 t_j G_c + \sum_j G_c t_{j+2} G_0 t_{j+1} G_0 t_j G_c + \dots \end{aligned} \quad (2.33)$$

Using the spectral representation

$$\sum_f |\psi_f\rangle \delta(E - E_F) \langle \psi_f| = -\frac{1}{\pi} \text{Im} G(\mathbf{r}', \mathbf{r}, E), \quad (2.34)$$

the absorption coefficient $\mu(E)$ can also be calculated from Fermi's Golden rule using Green's function with the dipole approximation

$$\begin{aligned} \mu(E) &= 4\pi^2 \zeta \omega \sum_f |\langle \psi_f | \boldsymbol{\epsilon} \cdot \mathbf{r} | \psi_i \rangle|^2 \delta(E - E_F) \\ &= 4\pi^2 \zeta \omega \sum_f \langle \psi_i | \hat{\boldsymbol{\epsilon}}^* \cdot \mathbf{r} | \psi_f \rangle \delta(E - E_F) \langle \psi_f | \boldsymbol{\epsilon} \cdot \mathbf{r} | \psi_i \rangle \\ &\simeq -\frac{1}{\pi} \text{Im} \langle \psi_i | \hat{\boldsymbol{\epsilon}}^* \cdot \mathbf{r} G(\mathbf{r}', \mathbf{r}, E) \boldsymbol{\epsilon} \cdot \mathbf{r} | \psi_i \rangle, \end{aligned} \quad (2.35)$$

where $\zeta \cong 1/137$ is the fine structure constant, ω is the X-ray energy in the units of Hartree atomic units ($e = m_e = \hbar = 1$). In the case of the single scattering, the Green's function $G(r', r, E)$ can be substituted by the dipole matrix elements $P_{lm, l_0 m_0}$ between the core state and the final states, and then the same expression as Eq. (2.19) is obtained. When the multiple scattering is taken into account, the same series of amplitudes of scattered waves as Eq. (2.24) are obtained.

2.1.5 Curved-Wave Multiple-Scattering Theory

In the standard multiple-scattering theory [32] which is based on perturbation theory, the spherical muffin-tin potentials without overlapping are adopted inside the muffin-tin spheres around each atom, and the uniform potential in the interstitial regions between muffin-tin spheres. This method is referred to a "path" approach since the perturbation can be expressed in terms of a free propagator from atom to atom. The path approach works well in the high-energy region above the threshold energy. Its major drawback is the difficulty to enumerate all of the possible paths for high-order scatterings. Rehr and Albers proposed a curved-wave multiple-scattering theory to overcome this limitation in the standard MS theory to permit arbitrary order scattering calculations [34].

In the curved-wave multiple-scattering theory, the Green's function of the outgoing free propagator $G_0(\mathbf{r}, \mathbf{r}')$ can be expanded in a separable Green's function $G_{lm, l' m'}(\boldsymbol{\xi})$ about fixed

sites \mathbf{R} and \mathbf{R}' ,

$$\begin{aligned} G_0(\mathbf{r}, \mathbf{r}') &= -\frac{e^{ik|\mathbf{r}-\mathbf{r}'|}}{4\pi k|\mathbf{r}-\mathbf{r}'|} \\ &= \sum_{lm, l'm'} j_{lm}(\mathbf{r}-\mathbf{R}) j_{l'm'}^*(\mathbf{r}'-\mathbf{R}') G_{lm, l'm'}(\boldsymbol{\xi}), \end{aligned} \quad (2.36)$$

where

$$j_{lm}(\mathbf{r}-\mathbf{R}) = i^l j_l(kr) Y_{lm}(\mathbf{r}) \quad (2.37)$$

is the free spherical wave that is defined in terms of spherical Bessel functions $j_l(kr)$ and spherical harmonics functions $Y_{lm}(\mathbf{r})$, and the Green's function propagator $G_{lm, l'm'}(\boldsymbol{\xi})$ is defined by a separable representation,

$$\begin{aligned} G_{lm, l'm'}(\boldsymbol{\xi}) &= \frac{e^{i\rho}}{\rho} \sum_{\lambda_j} \tilde{\Gamma}_{\lambda_j}^{lm}(\boldsymbol{\xi}) \Gamma_{\lambda_j}^{l'm'}(\boldsymbol{\xi}), \\ \tilde{\Gamma}_{\lambda_j}^{lm}(\boldsymbol{\xi}) &= R_{m\mu}^l(\Omega_{\boldsymbol{\xi}^{-1}}) \tilde{\gamma}_{\mu\nu}^l(\boldsymbol{\xi}), \\ \Gamma_{\lambda_j}^{l'm'}(\boldsymbol{\xi}) &= R_{\mu m}^l(\Omega_{\boldsymbol{\xi}}) \gamma_{\mu\nu}^l(\boldsymbol{\xi}), \end{aligned} \quad (2.38)$$

where $\boldsymbol{\xi} = k(\mathbf{R}-\mathbf{R}')$ is a dimensionless bond vector, and λ_j indexes the scattering center at \mathbf{R}_j . $R_{m\mu}^l(\Omega_{\boldsymbol{\xi}})$ is a rotation matrix which rotates the bond direction $\boldsymbol{\xi}$ onto the z -axis. The rotation matrix $R_{\mu m}^l(\Omega_{\boldsymbol{\xi}})$ can be constructed by first rotating $\boldsymbol{\xi}$ onto z -axis and then rotating back from z -axis to $\boldsymbol{\xi}$. $\Omega_{\boldsymbol{\xi}^{-1}}$ denotes the inverse rotation operation Euler angles $(\alpha, \beta, \gamma)^{-1} = (-\gamma, -\beta, -\alpha)$. The spherical expansion coefficients $\tilde{\gamma}_{\mu\nu}^l(\boldsymbol{\xi})$ and $\gamma_{\mu\nu}^l(\boldsymbol{\xi})$ are given as

$$\begin{aligned} \tilde{\gamma}_{\mu\nu}^l(\rho) &= \frac{(2l+1)}{N_{l\mu}} \frac{C_l^{(\nu)}(z)}{\nu!} z^\nu, \\ \gamma_{\mu\nu}^l(\rho) &= (-1)^\mu N_{l\mu} \frac{C_l^{(\mu+\nu)}(z)}{(\mu+\nu)!} z^{\mu+\nu}, \\ z &= \frac{1}{i\xi}, \\ C_l^{(\nu)}(z) &= \frac{d^\nu}{dz^\nu} C_l(z), \\ N_{l\mu} &= \sqrt{\frac{(2l+1)(l-\mu)!}{(l+\mu)!}}, \end{aligned} \quad (2.39)$$

where $-l \leq \mu \leq l$ and $0 \leq \nu \leq \min(l, l'-\mu)$. $\min(l, l')$ denotes the minimum of l and l' . The spherical wave correction factor $C_l(z)$ can be generated efficiently by the recurrence relation,

$$\begin{aligned} C_{l+1}(z) &= C_{l-1}(z) - (2l+1)zC_l(z) \quad (l > 1), \\ C_0(z) &= 1, \quad C_1(z) = 1 - z. \end{aligned} \quad (2.40)$$

With the separable representation of $G_{lm, l'm'}(\boldsymbol{\xi})$ described above, the multiple-scattering expansion can be rewritten in terms of scattering matrices. In the case of n -leg scattering (i.e., $n-1$ scatters), the exact multiple-scattering expansion is

$$\begin{aligned} G_{l_n m_n, l_0 m_0}^{(n-1)}(\mathbf{R}_1, \dots, \mathbf{R}_n) &= \sum_{lm} G_{l_n m_n, l_{n-1} m_{n-1}}(\boldsymbol{\xi}_n) \cdots t_2(\mathbf{R}_2) G_{l_2 m_2, l_1 m_1}(\boldsymbol{\xi}_2) t_1(\mathbf{R}_1) G_{l_1 m_1, l_0 m_0}(\boldsymbol{\xi}_1) \\ &= \frac{e^{i(\rho_1 + \rho_2 + \dots + \rho_n)}}{\rho_1 \rho_2 \cdots \rho_n} \sum_{\lambda_i} M_{\lambda_1, \lambda_n}^{l_0 m_0, l_n m_n}(\boldsymbol{\xi}_1, \boldsymbol{\xi}_n) F_{\lambda_n, \lambda_{n-1}}(\boldsymbol{\xi}_n, \boldsymbol{\xi}_{n-1}) \\ &\quad \times \cdots \times F_{\lambda_3, \lambda_2}(\boldsymbol{\xi}_3, \boldsymbol{\xi}_2) F_{\lambda_2, \lambda_1}(\boldsymbol{\xi}_2, \boldsymbol{\xi}_1), \end{aligned} \quad (2.41)$$

where $l_0 m_0$ and $l_n m_n$ denote the initial and final angular momenta. The summation over λ_j means that all of the n -leg paths are taken into account. $F_{\lambda_{i+1}, \lambda_i}(\boldsymbol{\xi}_{i+1}, \boldsymbol{\xi}_i)$ are the so-called “scattering-amplitude matrices” which are defined by the partial wave expansion

$$\begin{aligned} F_{\lambda_{i+1}, \lambda_i}(\boldsymbol{\xi}_{i+1}, \boldsymbol{\xi}_i) &= \sum_{lm} t_i \Gamma_{\lambda_{i+1}}^{lm}(\rho_{i+1}) \Gamma_{\lambda_i}^L(\boldsymbol{\xi}_i) \\ &= \sum_l t_i \gamma_{\mu\nu}^l(\boldsymbol{\xi}_{i+1}) R_{\mu\mu'}^l(\Omega_{\boldsymbol{\xi}_{i+1}, \boldsymbol{\xi}_i}) \tilde{\gamma}_{\mu'\nu'}^l(\boldsymbol{\xi}_i). \end{aligned} \quad (2.42)$$

The termination matrix $M_{\lambda_1, \lambda_n}^{l_0 m_0, l_n m_n}(\boldsymbol{\xi}_1, \boldsymbol{\xi}_n)$ is defined as

$$M_{\lambda_1, \lambda_n}^{l_0 m_0, l_n m_n}(\boldsymbol{\xi}_1, \boldsymbol{\xi}_n) = \Gamma_{\lambda_0}^{l_0 m_0}(\boldsymbol{\xi}_1) \tilde{\Gamma}_{\lambda_n}^{l_n m_n}(\boldsymbol{\xi}_n). \quad (2.43)$$

A general Debye-Waller factor $e^{-2k^2 \sigma_j^2}$ can be added into the above equation in order to include thermal effects on the j th path. Then the spectrum contribution from a given j th path with n -leg scattering is given in terms of the curved-wave MS expansion,

$$\begin{aligned} \chi_j(k) &= \text{Im} S_0^2 e^{2i\delta_i} G_{l_n m_n, l_0 m_0}^{(n-1)}(\mathbf{R}_1, \dots, \mathbf{R}_n) e^{-2k^2 \sigma_j^2} \\ &= \text{Im} S_0^2 \frac{e^{i(\rho_1 + \rho_2 + \dots + \rho_n + 2i\delta_i)}}{\rho_1 \rho_2 \dots \rho_n} \sum_{\lambda_j} M_{\lambda_1, \lambda_n}^{l_0 m_0, l_n m_n}(\boldsymbol{\xi}_1, \boldsymbol{\xi}_n) F_{\lambda_n, \lambda_{n-1}}(\boldsymbol{\xi}_n, \boldsymbol{\xi}_{n-1}) \times \dots \\ &\quad \times F_{\lambda_3, \lambda_2}(\boldsymbol{\xi}_3, \boldsymbol{\xi}_2) F_{\lambda_2, \lambda_1}(\boldsymbol{\xi}_2, \boldsymbol{\xi}_1) e^{-2k^2 \sigma_j^2}, \end{aligned} \quad (2.44)$$

where S_0^2 is an amplitude reduction factor due to many-body effects.

For simplicity, Eq. (2.44) can be rewritten in terms of the energy-dependent mean free path $\lambda(k)$ and the effective scattering amplitude F_{eff}

$$\chi^R(k) = S_0^2 \frac{N_R |F_{\text{eff}}|}{k R^2} \sin(2kR + \phi_{\text{eff}} + 2\delta_c) e^{-2R/\lambda(k)} e^{-2k^2 \sigma_R^2}, \quad (2.45)$$

where N_R is the number of atoms in the path with the effective length R , F_{eff} the effective backscattering amplitude for this path, ϕ_{eff} the effective phase shift, and δ_c the phase shift caused by the central atom, the factor 2 before δ_c indicates the twice phase shift during outgoing and incoming propagations.

Finally, one can obtain the total absorption coefficient by a summation over all of the scattering paths with a different effective scattering length R ,

$$\begin{aligned} \chi(k) &= \sum_R \chi^R(k) \\ &= S_0^2 \sum_R \frac{N_R |F_{\text{eff}}|}{k R^2} \sin(2kR + \phi_{\text{eff}} + 2\delta_c) e^{-2R/\lambda(k)} e^{-2k^2 \sigma_R^2}. \end{aligned} \quad (2.46)$$

2.1.6 Full Multiple-Scattering Theory

In the previous section the multiple-scattering expansion in Green’s function has been reviewed. The Green’s function propagator $G(\mathbf{r}, \mathbf{r}', E)$ was expanded in terms of the separable representation $G_{lm, l'm'}(\boldsymbol{\xi})$. In real calculations, a criterion (or path filter) is employed to cutoff those paths where the effective amplitude is lower than a certain value. When the kinetic energy of the photoelectron is high (>50 eV), the calculated spectrum can be well consistent with the experimental spectrum including only some important scattering paths. But in the near edge structure (NES) region, the photoelectron waves are scattered many times within a small cluster radius. The summation of the scattering paths which have a small amplitude might be larger than the contribution of the single scattering. In this case

the result may be not convergent correctly. Ideally, one might want to sum up the expansion to an infinite order to obtain an exact solution. But in practice, the matrix $F_{\lambda_{i+1}, \lambda_i}(\boldsymbol{\xi}_{i+1}, \boldsymbol{\xi}_i)$ in Eq. (2.42) yields a (1×1) matrix (vector) for the single scattering, a (3×3) matrix for the double scattering, a (6×6) matrix for the triple scattering, and so on. So, the limitation is the computing power for high-order scattering in the NES region. Therefore, the infinite summation requires a change in the method to calculate the effective scattering amplitude in Eq. (2.46).

Fortunately, the infinite summation of G_{sc} in Eq. (2.33) can be reformulated in terms of matrix inversion which implicitly includes all scattering orders,

$$G_{sc} = G_0(1 - tG_0)^{-1} = (1 - G_0t)^{-1}G_0. \quad (2.47)$$

For a larger cluster, one can combine full multiple-scattering and multiple-scattering methods to overcome the computational bottleneck. One can use a FMS calculation within a small cluster surrounding the absorbing atom and a MS calculation outside the FMS cluster but inside a much larger cluster. At the end of calculations, the two contributions are summed up to obtain the total spectrum. This method has been implemented in the commercial MS code Feff8.20 by Ankudinov et al. [37].

The spatial and energy dependence of the electron charge density can be expressed in terms of the imaginary part of the one-electron Green's function operator $G(\mathbf{r}, \mathbf{r}', E)$ which is an analytic function in the upper half of energy plane. The total DOS $\rho(E)$ for real energy is given by the integral of imaginary part of $G(\mathbf{r}, \mathbf{r}', E)$ in the real space,

$$\rho(E) = -\frac{2}{\pi} \text{Im} \int_{-\infty}^{\infty} G(\mathbf{r}, \mathbf{r}', E) d\mathbf{r}, \quad (2.48)$$

where the factor 2 accounts for spin degeneracy. Since both of the charge density and $\chi(k)$ can be calculated from $G(\mathbf{r}, \mathbf{r}', E)$, the *l*DOS and the EXAFS can be calculated by a single self-consistent-field (SCF) loop simultaneously. The SCF loop is described as the following.

Initially, the Fermi energy E_F can be found by integrating $\rho(E)$ below E_F to the electron numbers from the relationship

$$\sum_j N_j \int_C^{E_F} \rho_j(E) dE = N_{el}, \quad (2.49)$$

where N_j is the number of sites of the j th atom type, N_{el} the total number of electrons in the system, C the contour of integration, and $\rho_j(E)$ the DOS of j th atom type.

On the other hand, one can obtain the local Fermi energy E_F^j of the j th atom type in terms of the charge transfer q_j ,

$$\int_C^{E_F^j} \rho_j(E) dE = Z_j - q_j. \quad (2.50)$$

q_j can be calculated from the previous iteration,

$$q_j = Z_j - \int_0^{R_{nm}^j} 4\pi r^2 \rho_j^{old}(r) dr. \quad (2.51)$$

Z_j is the atomic number of the j th atom type, $\rho_j^{old}(r)$ the charge density of previous iteration, and the Norman radius R_{nm}^j is given by

$$\int_0^{R_{nm}^j} 4\pi r^2 \rho_j(r) = Z_j. \quad (2.52)$$

The new charge density in the new iteration is subsequently computed by

$$\begin{aligned}\rho_j^{new}(r) &= (1 - c)\rho_j^{old}(r) - c\rho_j(r) \\ \rho_j(r) &= -\frac{2}{\pi} \text{Im} \int_C^{E_F} G_j(\mathbf{r}, \mathbf{r}', E) dE,\end{aligned}\tag{2.53}$$

where c is the mixing factor. Once the new density is calculated, the new iteration starts to calculate new scattering potentials until $E_F = E_F^j$. After the above SCF loop, Both Fermi energy and charge transfer are obtained. An excellent review of FMS theory has been given by Rehr and Albers [36].

2.2 Band-Structure Method

In principle, the path approach (or MS-expansion method) is mathematically equivalent to the band-structure method as summing the path formalism to infinite order in an infinite cluster, i.e., the short-range order theory is equivalent to the long-range order theory [38]. The main discrepancy between these two methods is attributed to the truncation of cluster to a finite size. This contrast is most transparent in the Korringa-Kohn-Rostoker (KKR) band-structure method for calculating the electronic structure of periodic solids.

2.2.1 Density Functional Theory

The density functional theory (DFT) is one of many Ab-Initio techniques which attempt to solve the many-body Schrödinger equation,

$$H\Psi_j = E_j\Psi_j \quad (j = 1, 2, 3, \dots, N),\tag{2.54}$$

where H is the Hamiltonian of a quantum mechanical system composed of N particles. Ψ_j the j th wave function and E_j the energy eigenvalue of the j th state. For a N -electron system without the relativistic effect, the Hamiltonian is given by

$$H = -\frac{1}{2} \sum_{i=1}^N \nabla_i^2 + \sum_{i>j}^N \frac{1}{|\mathbf{r}_i - \mathbf{r}_j|} + \sum_{i=1}^N v(\mathbf{r}_i),\tag{2.55}$$

in the atomic units ($e = m_e = \hbar = 1$), where \mathbf{r}_i and \mathbf{r}_j are the coordinates of electrons. The first term of the right-side represents the electron kinetic energy. The second one is the electron-electron Coulomb interaction, and the third one is the Coulomb potential generated by the nuclei. This equation also assumes that the nuclei are effectively stationary with respect to the electron motions (Born-Oppenheimer approximation).

Initial approaches to this problem attempted to transform the full N -body equation into N single-particle equations by using the Hartree-Fock (HF) approximation. The accuracy of this approximation basically depends on the accuracy of the “exchange-correlation” contribution to the total energy. The exchange contribution is a direct consequence of Pauli’s exclusion principle, which prohibits two fermions from occupying the same quantum state. This reduces the probability of one electron being near another electron of the same spin. The correlation contribution is related to the reduction of the probability of an electron being near another electron due to the strong electron-electron Coulomb repulsion. The HF approximation only includes the correlation contribution for similar spin electrons, but neglects entirely the contribution for opposite spin electrons.

In contrast to these methods which try to determine the approximations of the electron density or many-electron wave function, DFT can “exactly” calculate the ground state property from the electron density $\rho(\mathbf{r})$. In 1964, Hohenberg and Kohn [39] considered the

ground state of the electron-gas system in an external potential $v(\mathbf{r})$, and proved that the following density functional theorem holds exactly: there is an universal functional $F[\rho(\mathbf{r})]$ of the electron charge density $\rho(\mathbf{r})$ that defines the total energy of the electronic system as

$$E_{tot} = \int v(\mathbf{r})\rho(\mathbf{r})d\mathbf{r} + F[\rho(\mathbf{r})]. \quad (2.56)$$

The total energy of the system can be minimized to find the true electron charge density in this external potential. This theory is exact for a non-degenerate ground state. Unfortunately, as yet an exact general form of the functional $F[\rho(\mathbf{r})]$ has not been found, so approximations must be introduced to obtain the explicit formula in practical calculations.

2.2.2 Local Density Approximation

The most commonly used and successful approximation of $F[\rho(r)]$ is the local density approximation (LDA), which first formulated by Kohn and Sham in 1965 [40]. If the total kinetic energy of the electrons can be written as $T[\rho(\mathbf{r})]$, then the universal functional is given by

$$F[\rho(\mathbf{r})] = T[\rho(\mathbf{r})] + \frac{1}{2} \int \frac{\rho(\mathbf{r})\rho(\mathbf{r}')}{|\mathbf{r} - \mathbf{r}'|} d\mathbf{r}d\mathbf{r}' + E_{xc}[\rho(\mathbf{r})], \quad (2.57)$$

where $E_{xc}[\rho(\mathbf{r})]$ is the exchange-correlation energy function and is given as

$$E_{xc}[\rho(\mathbf{r})] = \int \rho(\mathbf{r})\epsilon_{xc}(\rho)d\mathbf{r}, \quad (2.58)$$

where $\epsilon_{xc}(\rho)$ is the exchange-correlation energy for the electron-gas system which has a homogeneous charge density $\rho = \rho(\mathbf{r})$. Although this approximation had been thought to be valid only when the inhomogeneity of $\rho(\mathbf{r})$ is small at the beginning of investigations, in practice the LDA is proved to be applied even if the inhomogeneity is large.

By applying the variational principle to Eq. (2.56) with a constraint of

$$\int \rho(\mathbf{r})d\mathbf{r} = N \quad (2.59)$$

for a N -electron system, the following equation is obtained,

$$\int \left\{ \frac{\delta T[\rho(\mathbf{r})]}{\delta \rho(\mathbf{r})} + v(\mathbf{r}) + \int \frac{\rho(\mathbf{r}')}{|\mathbf{r} - \mathbf{r}'|} d\mathbf{r}' + \frac{\delta E_{xc}[\rho(\mathbf{r})]}{\delta \rho(\mathbf{r})} - \mu \right\} \delta \rho(\mathbf{r})d\mathbf{r} = 0, \quad (2.60)$$

where μ is the Lagrangian multiplier equivalent to the chemical potential. Using the wave function $\psi_j(\mathbf{r})$ of the j th electron, the total charge density is defined as

$$\rho(\mathbf{r}) = \sum_{j=1}^N |\psi_j(\mathbf{r})|^2, \quad (2.61)$$

which allows the kinetic energy to be written as

$$T[\rho(\mathbf{r})] = -\frac{1}{2} \sum_{j=1}^N \int \psi_j^*(\mathbf{r})\nabla^2 \psi_j(\mathbf{r})d\mathbf{r}. \quad (2.62)$$

The solution of equation (2.60) is subsequently given by solving the following effective one-electron Schrödinger equation for $\psi_j(\mathbf{r})$,

$$\left\{ -\frac{1}{2}\nabla^2 + v(\mathbf{r}) + \int \frac{\rho(\mathbf{r}')}{|\mathbf{r} - \mathbf{r}'|} d\mathbf{r}' + \frac{\delta E_{xc}[\rho(\mathbf{r})]}{\delta \rho(\mathbf{r})} \right\} \psi_j(\mathbf{r}) = \epsilon_j \psi_j(\mathbf{r}). \quad (2.63)$$

This equation is called the Kohn-Sham equation. The energy eigenvalue of the j th state ϵ_j is usually identified as the one-electron energy level [41]. If Eq. (2.63) is self-consistently solved, the electron charge density (cf. Eq. 2.61) and kinetic energy density (cf. Eq. 2.62) can be obtained via the solution $\psi_j(\mathbf{r})$.

2.2.3 Full-potential Linearized-Augmented Plane-Wave

The deviation of the real potential from the muffin-tin potential can be corrected by some methods, the corrected potential is often called the “full potential”. The full-potential linearized-augmented plane-wave (FLAPW) method has been proven to be one of the most accurate methods for calculating the electronic structure of solids within density functional theory. The FLAPW theory based on the LDA method has been developed for more than twenty years. For valence states, relativistic effects can be included either in a scalar relativistic treatment or with the second variational method including spin-orbit coupling. Meanwhile, core states can be treated fully relativistically. The various FLAPW formalism and programming methods can be found in many references [42].

Like most of the band-structure methods, the FLAPW method is a procedure for solving the Kohn-Sham equations for the ground state density, the total energy, and the band energy of a many-electron system by introducing a basis set which is especially adapted to the problem. This adaptation is achieved by dividing the unit cell into non-overlapping atomic spheres around the atomic sites and the interstitial region between the muffin-tin spheres. In the two regions different basis sets are used.

Inside the muffin-tin sphere, the wave function is described by a linear combination of radial functions times spherical harmonics,

$$\phi_{\mathbf{k}_n}^{In}(\mathbf{r}) = \sum_{lm} [A_{lm}(\mathbf{k}_n)u_l(r, E_l) + B_{lm}(\mathbf{k}_n)\dot{u}_l(r, E_l)]Y_{lm}(\hat{\mathbf{r}}), \quad (2.64)$$

where $\mathbf{k}_n = \mathbf{k} + \mathbf{K}_n$, \mathbf{k} is the wave vector inside the irreducible Brillouin zone (IBZ), \mathbf{K}_n the n th reciprocal lattice vector, $u_l(r, E_l)$ the radial solution of Schrödinger equation with energy E_l , $\dot{u}_l(r, E_l)$ is the energy derivative of $u_l(r, E_l)$.

Outside the muffin-tin sphere (interstitial region), the wave function is given as an augmented plane wave

$$\phi_{\mathbf{k}_n}^{Out}(\mathbf{r}) = W_{\mathbf{k}}(K_n)e^{i\mathbf{k}_n \cdot \mathbf{r}}. \quad (2.65)$$

The exponential function can be expanded in terms of products of spherical Bessel function and spherical harmonics,

$$e^{i\mathbf{k}_n \cdot \mathbf{r}} = 4\pi \sum_{lm} i^l j_l(k_n r) Y_{lm}(\mathbf{k}_n) Y_{lm}(\hat{\mathbf{r}}). \quad (2.66)$$

Therefore the wave function (Bloch state) in the interstitial region is described as a superposition of plane waves inside the muffin-tin sphere. The coefficient $A_{lm}(\mathbf{k}_n)$, $B_{lm}(\mathbf{k}_n)$ and $W_{lm}(\mathbf{K}_n)$ are determined by matching the inside and outside wave functions at the boundaries of muffin-tin spheres.

The solutions of the Kohn-Sham equations are expanded in the combined basis set according to the linear variation method,

$$\psi_{\mathbf{k}}(\mathbf{r}) = \sum_n c_n \phi_{\mathbf{k}_n}(\mathbf{r}), \quad (2.67)$$

where the coefficient c_n is determined by the Rayleigh-Ritz variational principle. The summation is over all of the reciprocal lattice vectors. The convergence of the basis set is controlled by a cutoff parameter $R_{\text{MT}} * K_{\text{nmax}} = 6 - 9$, where R_{MT} is the smallest muffin-tin radius in the unit cell and K_{nmax} the maximum of K_n . Because no shape approximations are made, the procedure described above is frequently called the “full-potential LAPW” method.

In order to improve upon the linearization and to make a consistent treatment of semicore and valence states possible in one energy window, additional basis functions $\phi_{\mathbf{k}_n}^{lo}(\mathbf{r})$ can be added. They are called “local orbitals (LO)” which consist of a linear combination of two

radial functions at two different energies (e.g, at the 3s and 4s energy levels) and one energy derivative (at one of these energies),

$$\phi_{\mathbf{k}_n}^{l\sigma}(\mathbf{r}) = \sum_{lm} [A_{lm}u_l(r, E_{1,l}) + B_{lm}\dot{u}_l(r, E_{1,l}) + C_{lm}u_l(r, E_{2,l})]Y_{lm}(\hat{\mathbf{r}}). \quad (2.68)$$

The coefficients A_{lm} , B_{lm} and C_{lm} are not dependent on \mathbf{k}_n . They can be determined by the requirement that the local orbitals are zero at the sphere boundaries and normalized.

2.2.4 Generalized Gradient Approximation (GGA)

In the LDA method, the spin-polarization can also be taken into account for the magnetic materials. This referred to the local spin density approximation (LSDA). Several forms of LSDA potentials exist in the literature. Many modern DFT codes use more advanced approximations to improve accuracy for certain physical properties. As stated above, the LDA uses the exchange-correlation energy for the uniform electron gas at every point in the system, regardless of the homogeneity of the real charge density. For nonuniform charge densities, the exchange-correlation energy can deviate significantly from the uniform result. This deviation can be corrected in terms of the gradient and high-spatial derivatives of the total charge density for those systems where the charge density is slowly varying. In recent progress, the LDA has been improved by adding some gradient terms of the electron density to the exchange-correlation energy or its corresponding potential [43, 44]. This improved approximation has been referred to the generalized gradient approximation (GGA) in the literature. The DFT calculations in this thesis have been performed by the GGA method.

2.3 Ligand-Field Atomic Multiplet Method

As mentioned before, the multiple-scattering and band-structure methods neglect multiplet effects which dominate the white-line features in the near edge structure of transition-metal elements. The term “white-line” denotes the sharp peaks just several eV above the threshold energy in the L_{23} edges of transition-metal elements. The atomic-multiplet theory is focused on multiplet effects in terms of ligand field or crystal field. This method is very successful to describe the core-to-3d excitations in transition metal elements and the core-to-4f excitations in rare earth elements [45]. The theoretical and experimental results are in good agreement not only in the crystal splitting of the white-line structures but also in the relative intensities of the peaks. The general description of the ligand-field atomic multiplet theory is briefly summarized here to clarify the different points with the band-structure and multiple-scattering approaches.

2.3.1 Ligand-Field Model

The ligand-field atomic model was first developed by Yamaguchi et al. [46] and generalized by the works of Thole and van der Lann et al. [47, 48]. Within the perturbation theory, the total Hamiltonian consists of intra-atomic interactions and a perturbation term from the nearest neighboring atoms (ligand atoms). In the intra-atomic terms, the electrostatic interaction terms (Coulomb integrals F^k and exchange integrals G^k) are reduced by multiplying a free parameter (which is given as a known factor in the calculations) to simulate the multi-configuration and hybridization effects [45]. The perturbation term is so called “ligand-field” or “crystal-field” in the literature, which describes the effect of a mono-electronic potential acting on the valence orbits of the absorbing atom. In this thesis, the term “ligand-field” is used to denote the net field of the nearest neighboring atoms, and the term “crystal-field” is used to describe the total net field of the surrounding atoms.

The so-called “superposition model” is usually adopted to construct the ligand field. In this model, the ligand field can be built from a superposition of the individual field of the ligand atom because the three-center interactions are about one order of magnitude smaller than two-center interactions due to the strong electrostatic repulsion between ligands [49]. So, the ligand field in arbitrary symmetric system can be calculated without the elusive group theory knowledge [50].

The framework of the ligand-field calculation was given by de Groot and Fuggle [51]. The absorption cross-section is given by

$$\sigma(E) \propto \sum_f |\langle \psi_f | H' | \psi_i \rangle|^2 \delta(E + E_i - E_f), \quad (2.69)$$

where H' is the perturbation Hamiltonian (or interaction operator). For the L_{23} edges, the dipole-allowed transitions are $2p \rightarrow 3d$ and $2p \rightarrow 4s$. Because the possibility of the $2p \rightarrow 3d$ transition is much larger than that of the $2p \rightarrow 4s$ transition, the latter transition can be neglected in the calculations. Eq. (2.69) can be rewritten to

$$\sigma_{3d}(E) \propto |\langle \psi_{3d} | H' | \psi_{2p} \rangle|^2 \rho_{3d}(E), \quad (2.70)$$

where $\rho_{3d}(E)$ is the unoccupied $3d$ density of states which can be calculated using the band structure method described in the previous section. In this chapter, it was taken as a known function.

In $3d$ transition-metal compounds, the two-particle ($3d - 3d$ and $2p - 3d$) interactions are most important for the calculation of the L_{23} edges. These two-particle interactions determine the ground state of the transition-metal ion and split the final state into a large number of configurations. In the one-electron approximation, the $3d - 3d$ and $2p - 3d$ two-electron interactions are not included. For simplicity, one can start the atomic multiplet calculation without solid-state effects, i.e., the atomic multiplets are calculated in an isolate atom. Within this assumption, the initial state and final states can be calculated in a spherical symmetry $O(3)$. Eq. (2.69) becomes

$$\sigma_{3d}(E) \propto \sum_f |\langle \psi_f^{O(3)}(2p^5 3d^{N+1}) | H' | \psi_i^{O(3)}(2p^6 3d^N) \rangle|^2 \rho_{3d}(E), \quad (2.71)$$

where N is the occupation number of $3d$ orbitals.

2.3.2 Hamiltonian Construction

The perturbation Hamiltonian of initial state $2p^6 3d^N$ only consists of the $3d - 3d$ Coulomb interaction H_{dd} , which can be expanded in spherical harmonics. Its radial parts F_{dd}^0 , F_{dd}^2 , and F_{dd}^4 are calculated within the Hartree-Fock approximation and reduced to 80% of origin values to involve the intra-atomic configuration interaction (CI) [45]. The integral F^0 does not affect the multiplet, but only causes a shift in the average energy. The multiplet splitting is determined by the multipole terms of $3d - 3d$ interactions (F_{dd}^2 and F_{dd}^4) which also determine the initial state multiplets. The $3d$ spin-orbit coupling of the initial state is small and can be neglected. The initial state Hamiltonian is represented by

$$H_{\text{init}} = H_0 + H_{dd}, \quad (2.72)$$

where H_0 consists of the kinetic term and the interaction with the nuclei.

The $2p^5 3d^{N+1}$ final state Hamiltonian includes two terms related to the $2p$ core hole. Firstly, the spin-orbit coupling of the $2p$ electrons with the core hole, H_{pp} , which causes the energetic separation of the $2p_{3/2}$ and $2p_{1/2}$ states. The $2p_{3/2}$ and $2p_{1/2}$ states correspond to the L_3 and L_2 edges, respectively. Thus, the L_{23} edges can be calculated simultaneously, in contrast to be calculated one by one in the multiple-scattering and band-structure methods.

Secondly, $2p - 3d$ Coulomb and exchange interactions, H_{pd} , which also originate from the core hole effect. The radial parts of the Coulomb terms (F_{pd}^0 and F_{pd}^2) and the exchange terms (G_{pd}^1 and G_{pd}^3) can be calculated by the Cowan code named ‘‘RCG’’ [45]. The $2p - 3d$ Coulomb interaction term F_{pd}^0 is equal for all final states, which only causes an energy shift but not changes the shape of the fine structures. Including the $3d - 3d$ Coulomb interaction term H_{dd} , the Hamiltonian of the final states is written by

$$H_{\text{final}} = H_0 + H_{dd} + H_{pp} + H_{pd}. \quad (2.73)$$

2.3.3 Crystal-Field Effects

To taken into account the solid-state effects, a crystal-field (CF) term (H_{cf}) needs to be added into the Hamiltonians of both initial state and final state. The crystal field is composed by one or several crystal-field parameters. For example, one parameter (Dq) is needed to describe the cubic (O_h) crystal field, and three parameters (Dq , Ds and Dt) are needed to describe the D_{4h} crystal field. The lower symmetric crystal field the more crystal field parameters [51].

The crystal field can split the initial-state and final-state multiplets. For a small crystal field, the electron energetically prefers to occupy the state with a spin parallel to the others according to Hund’s rule. This is called ‘‘high-spin’’ state in the literature. For a strong crystal field, a different electron configuration can be formed with electron pairs. In this case, the atom becomes ‘‘low-spin’’. A significant modification of the EELS spectra would be found when the transition occurs. For a O_h crystal field effects on d^4 electrons, the schematic illustration of the transition from high-spin state to low-spin state is shown in Fig. 2.2. ΔE indicates the crystal field splitting. When the ligand atoms present around the absorbing atom, the degenerate d states are separated into two e_g ($dx^2 - dy^2$ and dz^2) and three t_{2g} (dxy , dyz and dxz) states. If the crystal field ΔE is weak, the parallel spin is energetically favorable. Four electrons with parallel spins will be found. If the crystal field is strong enough, one electron pair will be formed on the low-energy t_{2g} orbits according to Hund’s rule.

According to group theory, the crystal-field effect is equivalent to the reduction of the spherical symmetric multiplets [52]. The calculations consist of three steps. First, the energy levels in the initial state ($2p^63d^N$) multiplet and the final state ($2p^53d^{N+1}$) multiplet are calculated in $O(3)$ symmetry. Then, the atomic multiplet spectrum is calculated by the means of the dipole transition from the ground state to all final states. Finally, the $O(3)$ multiplets are projected onto the irreducible representations of the ligand-field symmetry group. In the case of O_h crystal field, the spherical symmetry is reduced from $O(3)$ to its subgroup O_h . If a lower-symmetric D_{4h} crystal field is applied, the spherical symmetry is reduced from $O(3)$ to O_h first, then forward to D_{4h} . This procedure is called ‘‘branching’’ in the group theory [52].

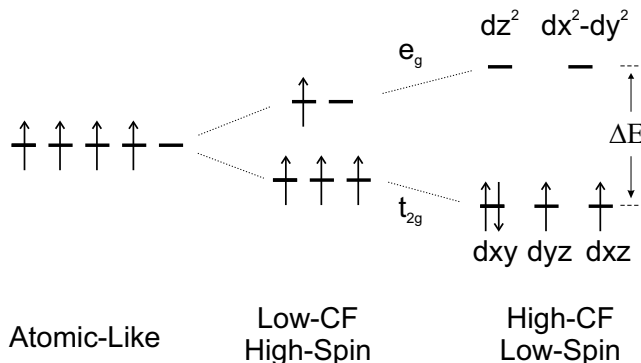


Fig. 2.2: Schematic illustration of the transition from high-spin state to low-spin state.

The group theory method is limited by the elusive branching for a lower-symmetric crystal-field. Mirone and Sacchi et al. proposed a numerical method which did not depend on group theory [50]. In their work, the Hamiltonian consists of intra-atomic interactions and perturbation terms describing the effect of the ligand atoms. The ligand-field effect is described by a $(2l + 1) \times (2l + 1)$ mono-electronic potential matrix which gives the potential elements between each mono-electronic level. The ligand-field matrix is constructed by rotating the identity matrix of the individual ligand atom to the angular momentum quantization axis (z-axis) one by one with a length scale. Therefore, this method can be applied to any geometry regardless of the ligand-field symmetry. For example, the ligand-field matrix for the $3d$ orbits in O_h symmetry is given by [50]

$$C_{O_h} = \begin{pmatrix} 3/2 & 0 & 0 & 0 & 3/2 \\ 0 & 0 & 0 & 0 & 0 \\ 0 & 0 & 3 & 0 & 0 \\ 0 & 0 & 0 & 0 & 0 \\ 3/2 & 0 & 0 & 0 & 3/2 \end{pmatrix}. \quad (2.74)$$

2.4 Comparison of Different Calculation Methods

The three theoretical calculation methods have their advantages and shortages. In order to compare the abilities of the three methods, the Ti L_{23} and O K edges in rutile TiO_2 have been calculated. The lattice parameters ($a=4.594$ Å, $c=2.959$ Å) are taken from Ref. [53]. The unit cell of rutile TiO_2 is sketched in Fig. 2.3. The titanium atom is surrounded by six oxygen atoms in a distorted octahedral coordination. The oxygen octahedron is distorted along the $[1\bar{1}1]$ direction. The length of the two Ti-O bonds in this direction is 1.980 Å. The other four Ti-O bonds are lying in the $(1\bar{1}0)$ plane with the bond length of 1.949 Å. The calculated spectra of the Ti L_{23} and O K edges are shown in Fig. 2.4 and 2.5 together with measured EEL spectra. The spectra have been aligned at the peak position of t_{2g} (the first peak). The energy-loss near-edge structures of the Ti L_{23} and O K edges are acquired from the single crystal rutile TiO_2 in order to show the accuracy of the different theoretical methods. The description of the calculation for each method is given in the following:

(1) The ground state Ti d DOS (d -character density of states) and O p DOS (p -character density of states) are calculated by the Wien2k code [42], which has been widely used and proved to be of a high accuracy for the band structure calculations. The muffin-tin radii of titanium and oxygen atoms have been set to 1.9 and 1.75 in units of the Bohr radius. A $8 \times 8 \times 13$ k-point sampling has been used in the irreducible Brillouin zone. The calculated Ti d DOS and O p DOS are used to compare with the other methods and the experimental EEL spectra. The Ti d DOS spectrum has been broadened by a gaussian distribution with a 0.1 eV full width at half maximum (FWHM). The O p DOS is broadened by 0.4 eV.

(2) The full multiple-scattering spectrum is calculated by the commercial Feff8.20 code [37]. The self-consistent-field iterations are performed within a sphere with a radius of 5.0 Å including 53 atoms. The FMS calculations can be done in a so-called “shell-by-shell” model.

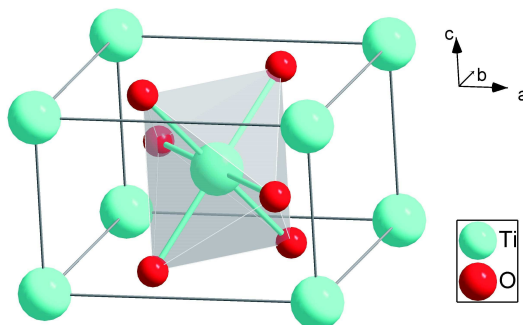


Fig. 2.3: Unit cell of the rutile TiO_2 .

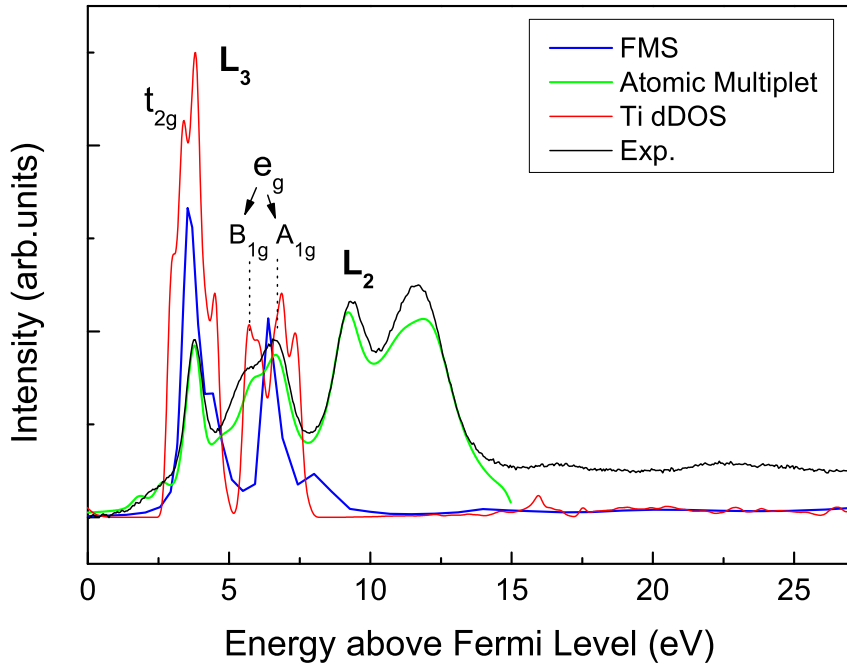


Fig. 2.4: Simulated near-edge structures of the Ti L₂₃ edges in rutile TiO₂ in comparison with the measured EEL spectrum.

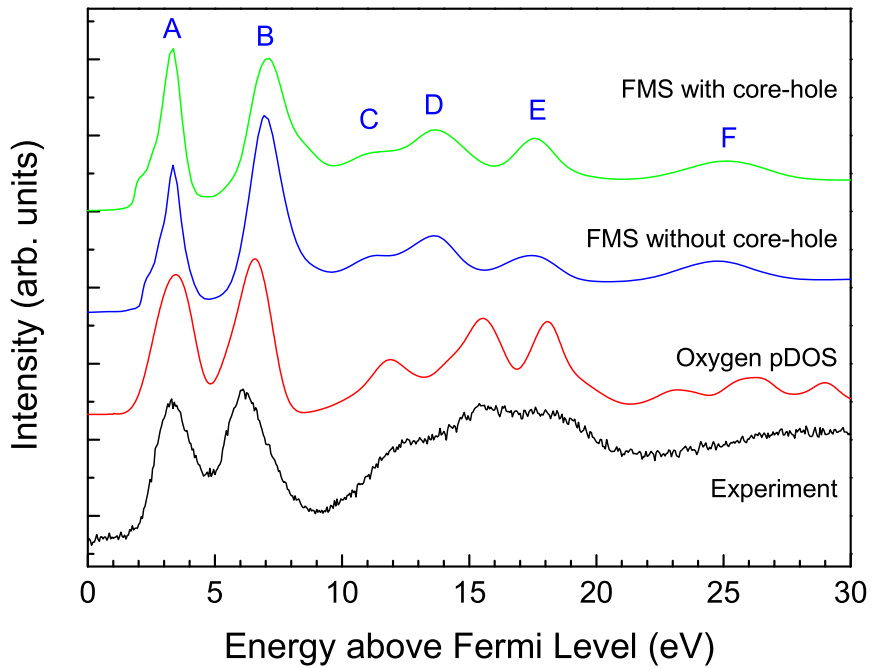


Fig. 2.5: Simulated near-edge structures of the oxygen K edge in rutile TiO₂ in comparison with the measured EEL spectrum.

That is, a series of shells are subsequently taken into account in the FMS cluster. The atoms in each shell have similar distances to the absorbing atom. In comparison with the previous-shell calculation, the variation of the calculated near edge structures is considered to be related to the new shell. Therefore, the relationship between the fine structures and the crystal structure can be given in this way. The atomic structures of neighboring atoms around the Ti atom and the oxygen atom are schematically shown in Fig. 2.6. The Ti-cluster contains 25 atoms which have been divided into four FMS shells. The first shell contains six nearest oxygen atoms octahedrally surrounding the central Ti atom with a distance range 1.949-1.980 Å. The second shell contains only two Ti atoms with a distance 2.959 Å along the z-axis. The third shell contains six oxygen atoms with a distance range 3.487-3.560 Å. The fourth shell contains eight Ti atoms with an identical distance of 3.569 Å. The oxygen-cluster contains 24 atoms which have also been divided into four FMS shells. The first shell contains three Ti atoms with a distance range 1.949-1.980 Å. The second shell contains thirteen oxygen atoms with a distance range 2.536-3.325 Å. The third shell contains four Ti atoms in the range 3.487-3.560 Å. The fourth shell contains three oxygen atoms in the range 3.897-3.960 Å. The FMS calculations of the Ti L_3 and O K edges in the shell-by-shell models described above are shown in Fig. 2.7(a) and (b). In Fig. 2.7(a), the peaks t_{2g} and e_g in the Ti L_3 edge are reproduced in the 7-atom cluster (one absorbing Ti atom and six nearest oxygen atoms). Due to the formation of a “core hole” after a core-level electron was excited into the unoccupied DOS, the final states are different from the ground state DOS. This effect is called the “core-hole effect”. The core-hole effect is considered in the present FMS calculations with a fully relaxed potential in the presence of a core hole [37]. In order to compare with the experimental spectrum, the theoretical spectrum should be appropriately broadened. The spectral broadenings consist of the instrumental broadening and the core-hole lifetime broadening. The latter broadening is caused by the relaxation of the core-hole. A 0.4 eV FWHM broadening is used in the FMS calculations. This value is the same as the energy resolution of the used instrument in this thesis.

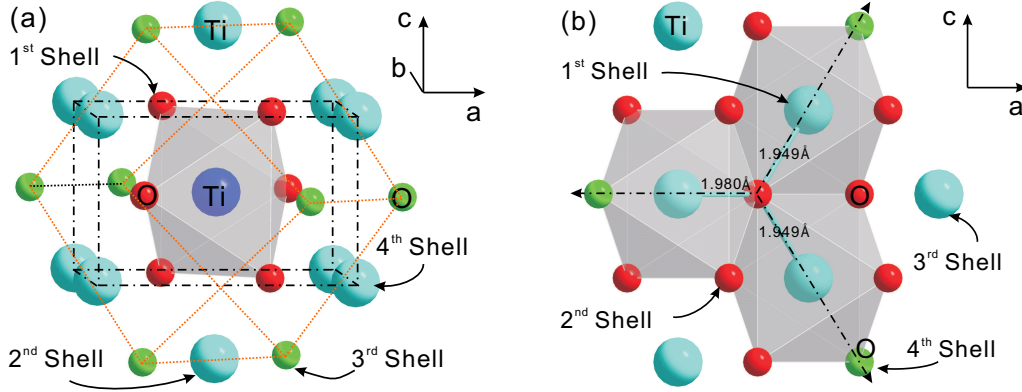


Fig. 2.6: Atomic structures of the neighboring atoms surrounding the Ti atom (a) (containing 25 atoms) and the oxygen atom (b) (containing 24 atoms) in rutile TiO_2 . The dashed lines indicate the Ti-O bonding directions.

(3) The atomic multiplet spectrum is calculated in the D_{4h} ligand field with the ligand-field parameters $10Dq=2.35$ eV, $ds=0.25$ eV and $dt=0.1$ eV by the TT-multiplet code [51, 54]. The Coulomb radial integrals F_{ij}^k and the exchange radial integrals G_{ij}^k are calculated from the Cowan code RCN [45]. Because the appropriate broadening of the calculated multiplets is very important for comparing with the measured spectrum, the description of the spectral broadening is given as follows. At first, the calculated multiplets were segmentally broadened by the different values, 0.2 eV (L_3, t_{2g}), 0.6 eV (L_3, e_g), 0.6 eV (L_2, t_{2g}) and 0.8 eV (L_2, e_g)

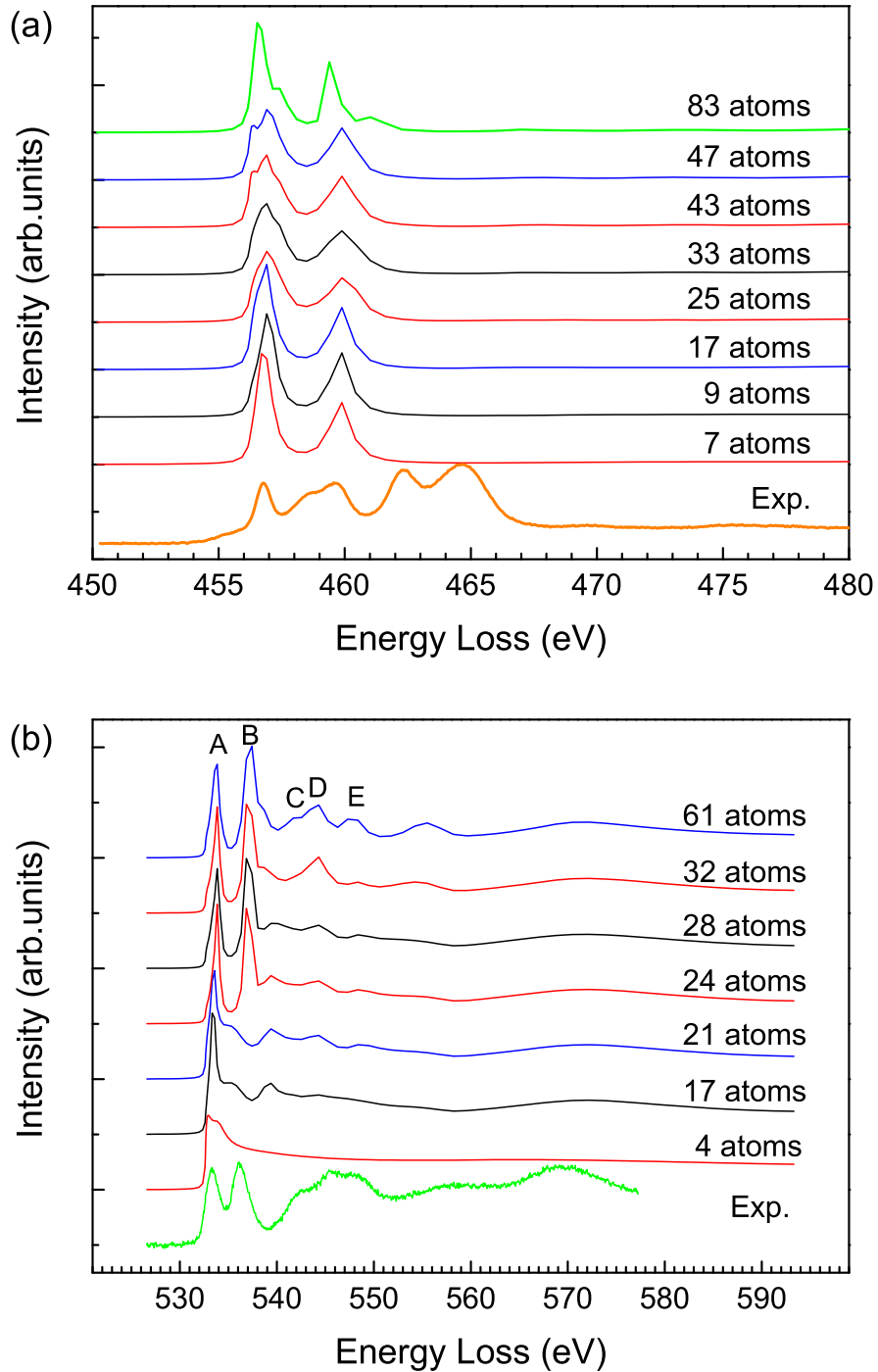


Fig. 2.7: FMS calculations in shell-by-shell model for (a) Ti L_3 edge and (b) O K edge.

FWHMs. This broadening is to simulate the different core-hole lifetime broadening at the different energy. Generally speaking, the spectrum is broader at the higher energy loss according to Heisenberg's uncertainty principle [55]. Next, a 0.4 FWHM broadening is performed to simulate the instrumental broadening. Note that the ligand-field parameters are obtained by fitting the theoretical spectrum to the experimental spectrum. A series of spectra with the different ligand-field parameters have to be calculated. The varying spectra of the Ti L_{23} edges with different intensions of the ligand field ($10Dq$) are given in Fig. 2.8. One can see that the best agreement with the experimental spectrum is obtained at $Dq \simeq 2.3$ eV.

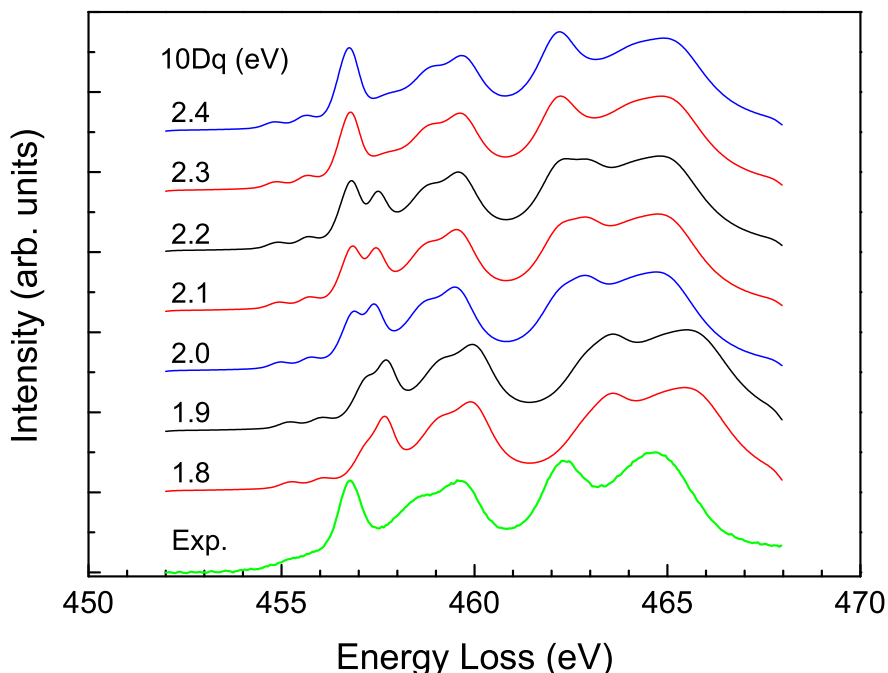


Fig. 2.8: Ti L_{23} edges in the D_{4h} ligand-field coordination calculated by the ligand-field atomic multiplet method. $10Dq$ ranges from 1.8 to 2.4 eV.

In the Ti L_3 edge (cf. Fig. 2.4), the major peaks of the crystal-field splitting, t_{2g} and e_g , are reproduced by all of the three theoretical methods. However, since the multiplet effect has been ignored in the FMS and band-structure methods, the relative intensities of the peaks t_{2g} and e_g are not correct. The peak t_{2g} is overestimated in these two methods. In the band-structure method, the calculated peak positions are well consistent with the EEL spectrum. But the peak positions calculated by the FMS method are of lower accuracy which might be caused by the less accurate muffin-tin potential. In the Ti L_{23} edges calculated by the ligand-field atomic multiplet, the theoretical spectrum is in excellent agreement with the experimental spectrum. The major shortage of the LFAM method is that the ligand-field parameters have to be fitted to the experimental spectrum. In principle, these parameters can be calculated by Ab-Initio methods. However, the splitting (B_{1g} and A_{1g}) of the peak e_g , caused by the distortion of the oxygen octahedron, is also reproduced in all three methods.

For the oxygen K edge in Fig. 2.5, both the main features and their relative intensities are fairly well reproduced by the band structure and FMS methods. Note that the ligand-field atomic multiplet method is not suitable for this case because the photoelectron is not

strongly localized around the oxygen atom. Therefore, the multiplet effect is not important. The theoretical spectra have been broadened by 0.4 eV. As shown in Fig. 2.5, the estimation of the core-hole effect can be given by comparing the FMS calculations with (blue line) and without core hole (green line). Generally, the core-hole effect has the following consequences: (1) shifting the peaks to lower energy, (2) compressing the energy separation between the peaks, (3) varying the intensities of the low-energy features. However, the core-hole effect on the oxygen K edge is very small due to the strong screening by the valence electrons. This is the reason why the ground state oxygen *p*DOS is in excellent agreement with the ELNES spectrum of the oxygen K edge. In comparison with the result of the FMS calculation, the band structure method shows a higher accuracy for the fine structures in the oxygen K edge.

As known, the electron energy-loss spectrum is sensitive to the orientation of crystals as the convergence angle is small [56, 57, 58, 59, 60]. The orientation-projected partial density of states can be calculated by the band-structure method. This advantage makes a polarization analysis possible. Although the accuracy of the FMS method is not very high, all of the main features can be reproduced when the FMS cluster is sufficient large. The most important advantage of the FMS method is that the spectrum can be calculated in the shell-by-shell model. By carefully comparing the variation of the fine structures with different shells, the relationship between the fine structures and the crystal structure can be derived. This technique works better for the high-energy region of the core-loss spectrum where the oxygen-oxygen interactions dominate the fine structures, and the band-structure interpretation is difficult. For example, in Fig. 2.7(b), a significantly changed peak B can be found between the 21-atom and 24-atom spectra. The three atoms are indicated by the green atoms in Fig. 2.6(b). The change indicates that the backscattering from the oxygen atoms along the Ti-O bonding directions is much stronger than from the other neighboring atoms (except the direct chemical bonding in the first shell), which gives a strong contribution for the peak e_g . This finding might be related to the electron hopping mechanism along the chemical bonding direction [61, 62, 63]. In fact, this result has been also found in the FMS calculations of the oxygen K edge for other oxide compounds, such as SrTiO₃, BaTiO₃, and Y₂O₃, which will be shown in chapters 4 and 5.

In order to compare with the experimental results, the theoretical spectra have to be broadened appropriately. The appropriate broadening is more critical for the sharp features in the calculated spectrum. The spectral broadening consists of the core-hole lifetime broadening, thermal-related broadening and the intrinsic broadening of the instruments. In the FMS method, the core-hole lifetime broadening is taken into account by the Green's function automatically. In the other two methods, a Gaussian or Lorentzian broadening is usually chosen for the whole spectrum in the literature. A more complicated segmented broadening method has been applied in the ligand-field atomic multiplet calculations [51]. Actually, although the instrumental broadening and thermal broadening are stationary with the energy loss, the core-hole lifetime broadening is different for the different energy loss according to Heisenberg's uncertainty principle, i.e., the longer core-hole lifetime the sharper absorption peak. Generally, the broadening is increasing with higher energy loss [54].

In summary, the main advantages and shortages of the three Ab-Initio methods are briefly given in Table 2.1. The FMS method is suitable for the fast calculation of the low-symmetric or complex materials. In low-symmetric or complex materials the band-structure calculations are very time consuming due to the large basis set. The band-structure method is suitable for the calculation of the oxygen K edge structures. The oxygen K edge structures calculated by the band-structure method is more accurate than the multiple-scattering method or the atomic multiplet method. The atomic multiplet method is suitable for the L₂₃ edges of the transition metal elements due to the consideration of the multiplet effects.

Table 2.1: Comparison the standard Ab-Initio methods for simulating ELNES.

	Full Multiple-Scattering Method	Band-Structure Method	Ligand-Field Atomic Multiplet Method
Periodical Requirement	Arbitrary symmetric systems	Periodic systems	Arbitrary symmetric systems
Speed	Fast	Time-consuming	Very fast
Accuracy	Higher in high-energy region	Higher in low-energy region	Depends on fitting
Core-Hole Effect	Yes	No	Yes
Multiplet Effect	No	No	Yes
Energy Scale	Absolute scale	Refer to Fermi energy	Absolute scale
Orientation Analysis	No	Yes	No

Chapter 3

Details of EELS Experiments

In this chapter, the details of EELS experiments will be described because the experimental conditions are critical to acquire reliable EELS/STEM spectra at the interface.

3.1 EELS/STEM Instruments

The illustration of the EELS/STEM instruments used in this thesis is schematically shown in Fig. 3.1. The specification of the instruments are listed in the following table.

Table 3.1: Specifications of the used EELS/STEM instrument.

Microscope:	STEM, VG HB 501 UX, cold field emission gun
Spectrometer:	Gatan Enfina 1000
Beam Energy:	5-100 keV
Spatial Resolution:	0.4 nm (imaging), 1 nm (analytic)
Energy Resolution:	0.05-2.0 eV/channel
CCD:	1340×100 pixels, 20×20 μm^2 photodiode
Scintillator:	YAG

The dedicated STEM (VG HB 501 UX, Vacuum Generators), equipped with a cold field emission gun (FEG), consists of three basic units (cf. Fig. 3.1): the electron optical column, the electronics console and the vacuum control rack. The electron gun consists of a single crystal tungsten field emitter followed by an extraction electrode and an accelerating electrode assembly. The variation of the field emission extraction voltage over the range of 1.1 kV to 4.5 kV adjusts the emission current. The two condenser lenses, C1 and C2, have the major function of controlling the demagnification of the source and the beam current at the specimen. The double scan coils permit the electron beam to rock about the point on the vertical axis of the column. The size of the objective aperture is very important to control the beam current, the probe size, and the convergence angle. The objective lens focuses the beam onto the specimen. The specimen is immersed in the field of the objective lens. The post specimen field produces an angular compression of the beam. Since the collection angle and the convergence angle are important in element ratio analysis, exact values of these parameters enhance the reliability of the quantitative analysis.

On the top of Fig. 3.1, a Gatan parallel EELS spectrometer (Enfina 1000), which is used to record the EEL spectra, is installed. Two entrance apertures with different sizes (2 mm and 4 mm) can be used to limit the collection angle and to control the exposure

time. The QX, QY, SX, SY alignment coils are used to align the transmitted electrons. The electrons with different energy are dispersed in the magnetic prism. The quadrupole lenses Q1-Q4 can be used to focus the dispersed electrons onto a fiber-optically coupled yttrium aluminum garnet (YAG) scintillator. The kinetic energy of the fast electrons is absorbed by the scintillator materials and converted to visible or ultraviolet light. When the light strikes the charge-coupled device (CCD) surface, it frees electrons which are accumulated in the capacitors. The electron charge is shifted in the CCD by regular electronic pulses and “counted” by a circuit. This gives an effective grayscale image indicating how much light has fallen on each individual pixel. In other words, the coupled YAG/CCD converts the electron energy into a digital count. The efficiency of the used YAG/CCD detector is that one 100 keV fast electron produces about 60 counts.

The counts are periodically read into a computer by the DigitalMicrograph 3.7.1 software package, which is used to control the automatic EELS acquisition, including qualitative and quantitative analysis. A plug-in tool and a script class, based on the DigitalMicrograph software development kit, script language, and Visual C++, were developed by the author to facilitate the processing of the spectra in this thesis. Their functions include subtracting the background for the raster image of line scans (a series of EEL spectra), spectrum shift, normalization, import and export, etc. Images and spectra can be controlled as matrixes and arrays, which is much faster than the pixel-by-pixel operation.

The STEM was operated at 100 keV as the electron energy-loss spectra were acquired. The operating pressure is $\sim 5.0 \times 10^{-9}$ mbar in the column and $\sim 3.0 \times 10^{-11}$ mbar in the field emission gun chamber. Both dark count readout and channel-to-channel variation in gain response are corrected by the corresponding standard procedures. The background of the spectrum is subtracted by the AE^{-r} power-law extrapolation of the pre-edge of the core-loss edge [64], where the coefficient A determines the intensity of the background, the exponent r (generally in the range 2–6) is responsible for the curvature of the fitting curves, and E denotes the energy loss. The energy resolution of the coupled microscope/spectrometer, determined from the full width at half maximum of the zero-loss peak (ZLP), amounts to about 0.4 eV. The beam current focused on the specimen is ~ 1 nA. An entrance aperture of 2 mm is selected for collecting inelastic electrons. The calibrated collection semiangle amounts to about 12 mrad in the STEM used. This collection angle is large enough to collect most of the inelastic electrons since the characteristic scattering angle is usually very small. For a 50 μm objective aperture, the convergence semiangle is ~ 14 mrad in the HB501 microscope. The estimation of the probe size, and the discussion of the calibration of collection angle, as well as the effects of the experimental conditions will be given in Section 3.3.

3.2 Specimen Preparation

The preparation of specimens with a good quality is the most critical work in EELS experiments. Good quality means that a specimen should have a large thin area, no contamination problems, no surface artifacts introduced and no surface charging effects. Especially, specimens containing an interface are much more difficult to prepare than bulk materials.

3.2.1 General Procedures

Thin film layers can be grown on certain substrates by several techniques, such as pulsed laser deposition (PLD), molecular beam epitaxial (MBE), electron beam evaporation, ion beam sputtering, etc. The first step is to cut the wafer with the original thin film into two parts of the same size using a diamond wire saw and then glue them face-to-face. In this work M-Bond 610 epoxy resin which has a very low viscosity was used. The glued sample is compressed by an uniformly distributed pressure during the curing time (2 h at curing

temperature 120°C). The sample is postcured at 160°C without pressure. A very thin glue layer (less than 1 μm) can be achieved. The glue layer should be as thin as possible. If not, the glue layer can be sputtered away quickly by the ion-milling, and a hole will be formed around the glue line when the specimen is still very thick. Another advantage of the M-Bond 610 epoxy resin is its high thermal stability up to 400°C and its resistivity against degassing in vacuum which minimizes the contamination.

The glued wafer is cut into sticks which are inserted into an alumina holder. The interspace between the sample and the alumina holder is filled by alumina slices and epoxy resin M-Bond AE-15, which has a high viscosity and a high elasticity. The cure is performed at 80°C for 1 h. The assembled cylinder is then cut into slices with a thickness of 0.5 mm. The 0.5 mm thick slice is roughly ground and polished on grinding and polishing paper in a Buehler Minimet polisher until the thickness is less than 100 μm . A Gatan Model 656 dimple grinder is used to dimple and polish from both sides at the center of the slice (the interface region) by a copper wheel with a radius of 15 mm. Hot wax was used to mount the slice onto a glass cylinder. After dimpling, the wax attached on the slice can be well cleaned several times by acetone in a Transsonic DigitalS vibrator. At the end of this step, the thickness at the dimple area is controlled in the range of 15-20 μm .

The final step is thinning the slice at the center of the dimple by ion sputtering until a transparent hole is formed. A Gatan PIPS 691 was used to do the work. Two Ar^+ ion guns bombard the up- and down-side of the specimen simultaneously. The incident angles were set to $\sim 3^\circ$. Such a small incident angle is important to obtain a large thin area around the transparent hole. However, the ion milling speed is very slow with such a small incident angle. A varying ion energy method has been used to quicken the specimen preparation. At the beginning of ion milling process, the ion energy is set to 3.5 keV. Several hours later when the specimen is nearly transparent, the ion energy is reduced to 2.5 keV. Finally, after the transparent hole is formed, the ion energy is further reduced to 1.5 keV until the ion milling is terminated.

3.2.2 High Quality EELS Specimens with Interfacial Structures

Obtaining a Large Thin Area

A high quality specimen should have a large thin area with an uniform thickness. The size of the thin area is controlled by the small incident angles of the ion-milling beams. In this condition the acquired spectra from different region can be compared more easily, and small variations can be found by direct comparison. For a perfect bulk material, all of the spectra should not be different if the experimental conditions do not change during the acquisition. There are several advantages of very thin specimens: (1) The plural scattering effect vanishes. Thus, the deconvolution of the edges is not necessary in this case, since artifacts may be introduced into the results by the deconvolution procedures. (2) A high signal-to-noise ratio can be obtained. This is important especially for small features. According to the author's experiences, a high quality spectrum can be obtained as the thickness of the specimen is in the range of 0.2-0.6 mean free path (MFP). If the specimen is too thin (< 0.2 MFP), the noise of the spectrum will be high. That causes the signal-to-noise ratio small. If the specimen is too thick (> 0.6 MFP), the plural scattering effect can not be ignored. That makes the interpretation of the fine structures difficult.

For a specimen with thin film structures, the interesting region is usually near the interface. In most cases, the thickness of the thin film is only several tens of nanometers. Due to the different ion-milling speed for the thin film and the substrate, the thin film layer is easily sputtered away from the substrate. This makes it often difficult to obtain a larger thin area for interfacial specimens. The solution is to stop the ion-milling process immediately as soon as the small hole is formed at the center.

Removing Surface Artifacts

In some cases, the microstructure of materials is very sensitive to high-energy ions. Surface damage may be found in TEM specimens prepared by the focused ion beam (FIB) method or after ion-milling when the ion energy is too high [65]. An amorphous layer can be formed on the surface. Another possibility of the formation of an amorphous layer on the surface is the re-deposition of the sputtered powder. Surface artifacts become more significant for thinner specimens. The problem can be solved by applying a small incident angle ($\sim 3^\circ$) and additional ion-milling at a lower ion-energy to remove the possible amorphous layer on the surface.

Minimizing Contamination

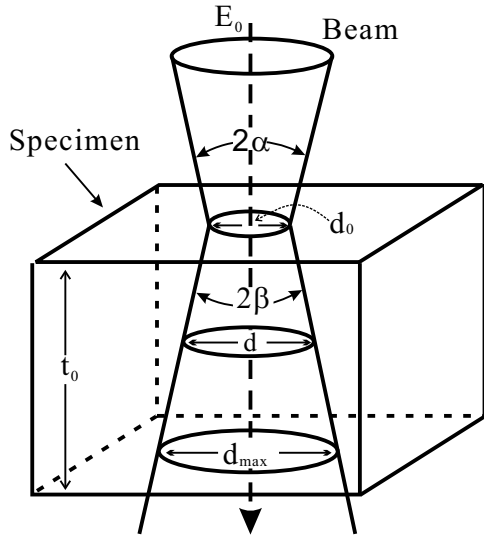
Carbon contamination is the most familiar contamination in EELS experiments due to the strong carbon K edge signal. A several angstrom thick carbon layer deposited on the specimen surface can hide most of the near edge structure of other elements. There are several sources responsible for carbon contamination, such as the glue layer, dust from air, the vacuum pump, and dust deposited on the apertures. There are also other kinds of contaminations, for example, copper contamination which comes mainly from the grinding procedure. There might be also iron or argon contamination from the thin film deposition [66], but the influence of these contaminations on ELNES is usually very small and can be neglected in practice. There are several general advices to minimize the carbon contamination: (1) The glue layer should be as thin as possible; (2) The prepared specimen should be put into the microscope as soon as possible; (3) The vacuum pump is cooled down by the liquid nitrogen.

3.3 Acquiring Spectra from Interfaces

In contrast to bulk materials, the difficulties of the investigation of interfaces are related not only to the preparation of the specimen, but also to the acquisition of the spectra. The experimental conditions, such as the spatial resolution, convergence angle, energy drift, spatial drift, decay of beam current, orientation of specimen, and surface-charging are very important to acquire reliable spectra from the interface. These conditions are not so critical for a bulk spectrum because the signals from anywhere are equivalent if the thickness is uniform. Prior to the investigation of interfaces in unknown materials, the optimum conditions for acquiring EEL spectra from the interface should be known. It is well known that the SiO₂/Si interface is very sharp, which can be proved from the rapidly developing metal-oxide-semiconductor technique. Indeed, a silicon-oxide gate dielectric thickness less than 0.8 nanometer has been achieved in the laboratory [4]. In this section, the influences of the experimental conditions on the spectra from the interfaces are discussed via the investigation of SiO₂/Si interface.

3.3.1 Spatial Resolution

A significant variation of EEL spectra at an interface usually occurs in a nanoscale or sub-nanoscale region. If the spatial resolution is too low, the probe is hard to exactly locate on the interface region, and most of the signals will come from the substrate or thin film far from the interface. The spatial resolution of STEM is related to the probe diameter d_0 , convergence semiangle α (incident beam), divergence semiangle β (transmitted beam), incident beam energy E_0 , and the thickness of the specimen t_0 . Smaller d_0 , α , β , t_0 , and higher E_0 correspond to a higher spatial resolution. Because the divergence semiangle is related to the beam energy and the convergence angle, E_0 and α can be included in the divergence semiangle $\beta(E_0, \alpha)$. The spatial resolution d can be defined by



$$\begin{aligned}
 d &= \frac{1}{2}[d_0 + d_{\max}(t_0, \beta)] \\
 &= d_0 + t_0 \tan(\beta) \\
 &\simeq d_0 + t_0 \beta(E_0, \alpha),
 \end{aligned}
 \tag{3.1}$$

as shown in Fig. 3.2, where d_{\max} is the maximum diameter of the broadened beam on the outgoing surface. The spatial resolution can be estimated by scanning over a sharp interface or edge, as shown schematically in Fig. 3.3.1, which is redrawn from Ref. [67]. The relationship between profile width L_0 and spatial resolution d is given by the following equation,

$$d = \sqrt{2}L_0. \tag{3.2}$$

The spatial resolution of the EELS/STEM was measured by the intensity profile of the Si L_{23} edges from silicon across the sharp SiO_2/Si interface with

a scanning step of 0.5 nm. In order to achieve a small convergence angle, a small objective aperture with a radius of 25 μm was selected. A 2 mm entrance aperture was selected to

Fig. 3.2: Definition of the spatial resolution.

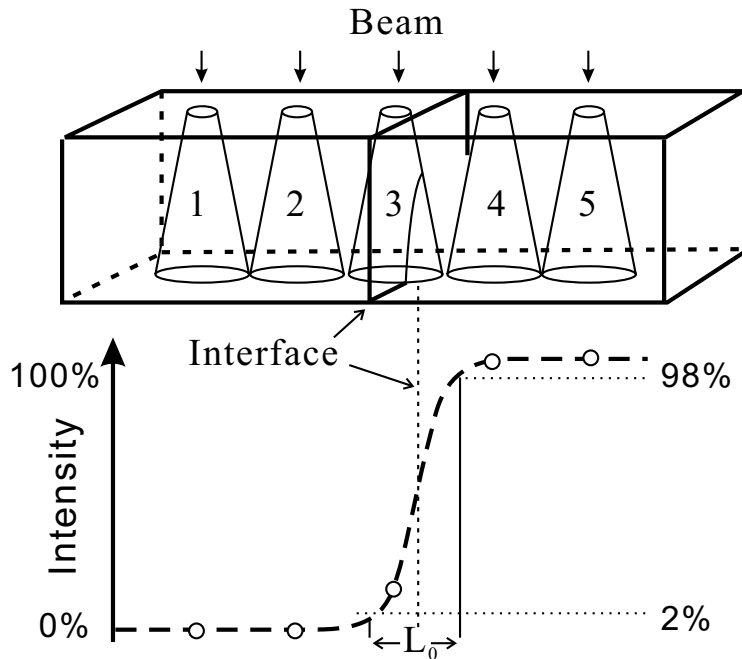


Fig. 3.3: Estimation of spatial resolution (redrawn from [67]). The top is the line scan across the sharp interface, and the bottom is the normalized intensity profile of the spectra (lower intensity is referred to zero percent and the upper intensity is referred to 100 percent). The distance L_0 related to the spatial resolution is measured between the intensities of 98% and 2%.

limit the collection angle. After the acquisition, the background was subtracted by the standard power-law method for all of the spectra in the raster image [64]. The resulting raster image is shown in Fig. 3.4. The first peak (marked by the white rectangle in Fig. 3.4) is used to estimate the spatial resolution. Due to the chemical shift of more than 5.0 eV in the Si L_{23} edges of SiO_2 , silicon and SiO_2 can be well distinguished in this energy range. The intensity profile is obtained by summing up the counts in the energy range, and the result is given in Fig. 3.5. The profile width L_0 is measured to be about 0.7 nm. Thus, about 1.0 nm spatial resolution is estimated for the EELS/STEM according to Eq. (3.2).

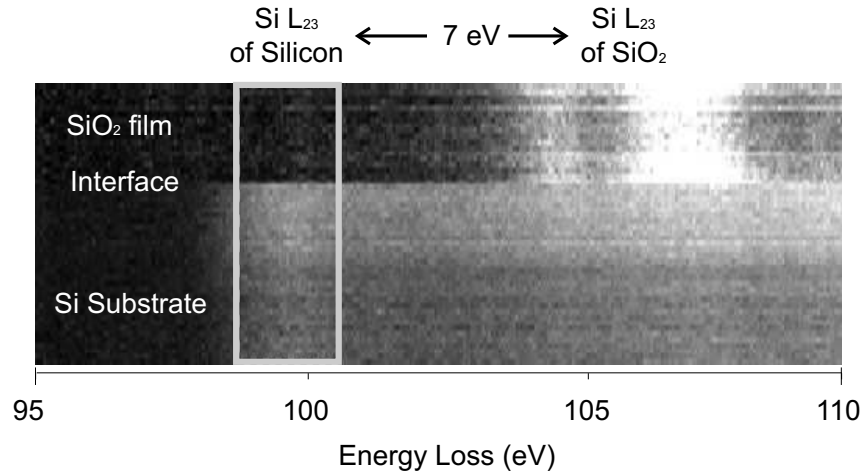


Fig. 3.4: Raster image of a line scan across the SiO_2/Si interface from the Si L_{23} edges. The background has been subtracted, and the scanning step is 0.5 nm. The white rectangle indicates the energy range used for estimating the spatial resolution.

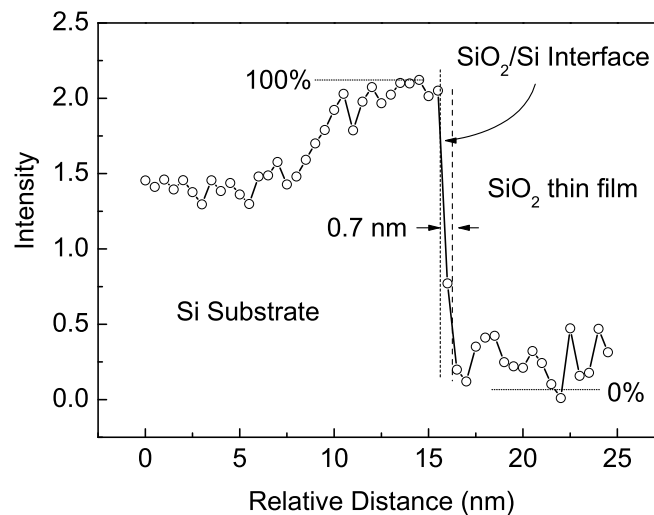


Fig. 3.5: Measurement of the spatial resolution of the EELS/STEM. The intensity profile is obtained from summing the intensity in the energy range marked by the white rectangle in Fig. 3.4.

In Fig. 3.5, the intensity increase in the silicon far from the interface is caused by the nonuniform thickness. Due to the faster ion-milling speed, the silicon region near the SiO_2/Si interface is a little thinner than that of the other silicon regions. The smaller thickness leads to a lower plasmon background, i.e., a higher signal intensity.

3.3.2 Convergence Angle

The effect of the convergence angle can be roughly estimated in the following way. Assuming the beam was focused on the exit surface, the convergence semiangle α can be obtained by

$$\tan \alpha = \frac{R_{\text{OA}}}{h}, \quad (3.3)$$

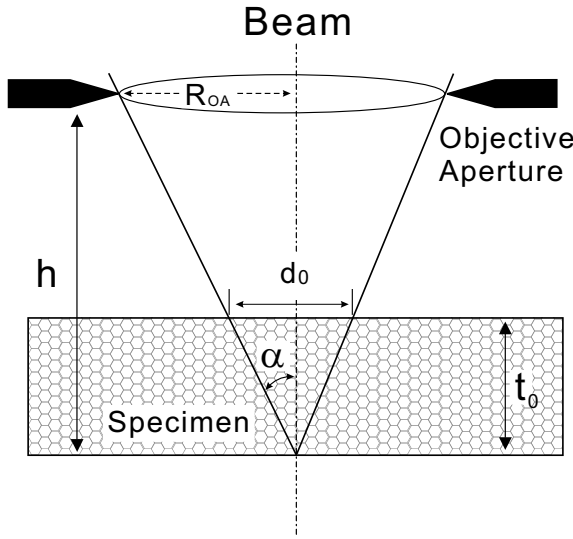


Fig. 3.6: Schematic illustration for estimating the effect of the radius of objective aperture.

where h is the distance from the objective aperture to the specimen, and R_{OA} the radius of objective aperture. In the HB501 STEM, the estimated convergence semiangle for the $100 \mu\text{m}$, $50 \mu\text{m}$, and $25 \mu\text{m}$ objective apertures is 28 mrad, 14 mrad and 7 mrad, respectively. The schematic illustration is drawn in Fig. 3.6. Therefore, for a typical specimen thickness $t_0=50 \text{ nm}$, the estimated probe size

$$d_0 = 2t_0 \tan \alpha \quad (3.4)$$

is 2.8 nm, 1.4 nm and 0.7 nm, respectively. According to Eq. (3.1), the spatial resolution is broadened to about 6.0 nm for a $100 \mu\text{m}$ objective aperture. It is a really bad resolution for acquiring EEL spectra from interface regions. For a better spatial resolution, the objective

aperture should be selected as small as possible. However, sometimes a larger objective aperture has to be selected due to weak signals.

The convergence angle is very critical for the investigation of interface structures. In STEM, the convergence angle is determined by the radius of the objective aperture. The effect of the radius of objective aperture (ROA) can be seen in Fig. 3.7. In Fig. 3.7(a), the spectra of the Si L_{23} edges were measured at the center of a 20 nm thick SiO_2 thin film with $100 \mu\text{m}$ and $25 \mu\text{m}$ ROAs, respectively. The $25 \mu\text{m}$ -ROA spectrum has been scaled to compare with the $100 \mu\text{m}$ -ROA spectrum. One can see that part of signals come from the silicon substrate as indicated by the small shoulder at 99 eV in the $100 \mu\text{m}$ -ROA spectrum, even though the probe was located about 10 nm away from the substrate. In fact, no significant silicon shoulder was found at 99 eV just 1 nm away from the interface when the $25 \mu\text{m}$ ROA was selected. Another illustration is given by a 10 nm thick BaTiO_3 layer which was deposited on $\text{SrTiO}_3(001)$ substrate using pulsed laser deposition. The oxygen K edge was acquired at the center of the BaTiO_3 layer with a $50 \mu\text{m}$ and a $100 \mu\text{m}$ ROA, respectively, as shown in Fig. 3.7(b). In this case, the application of the $25 \mu\text{m}$ ROA was not possible due to the weakness of the beam current. One can see, the third peak (indicated by the double vertical dashed lines) is well split in the $50 \mu\text{m}$ -ROA spectrum, but it can not be separated in the $100 \mu\text{m}$ -ROA spectrum.

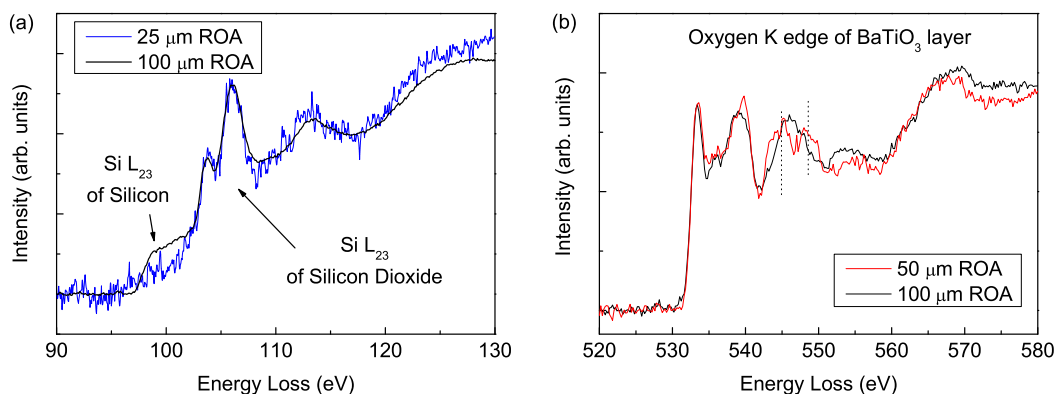


Fig. 3.7: The effect of the radius of objective aperture. (a) The Si L₂₃ edges acquired at the center of a 20 nm thick SiO₂ thin film which is deposited on a silicon substrate. (b) The oxygen K edge acquired at the center of a 10 nm thick BaTiO₃ layer which is deposited on a SrTiO₃(001) substrate. The double vertical dashed lines indicate the splitting of the third peak.

3.3.3 Collection Angle

In this work, a smaller entrance aperture of 2 mm is always selected for collecting the inelastic electrons. The uncalibrated collection semiangle, which is determined by the radius of the spectrometer entrance aperture and the distance from the specimen to the collection aperture, is ~ 6.5 mrad. However, the collection semiangle should be calibrated prior to the analysis of the element ratio because the atomic ratio is a function of the collection angle [64]. Because the specimen is always immersed in the field of the objective lens in the dedicated STEM, the post specimen field produces an angular compression of the transmitted electron beam. Consequently, the actual collection semiangle is somewhat larger than the uncalibrated value. The collection angle can be calibrated by projecting the spectrometer entrance aperture into the plane of the diffraction pattern of a known crystalline specimen to obtain the so-called “effective diameter” of the spectrometer entrance aperture [67]. The calibrated collection semiangle amounts to about 12 mrad in the HB501 STEM. The collection angle is large enough to collect most of the inelastically scattered electrons since the characteristic scattering angle is usually very small.

In order to exactly locate the probe on the position of interest, the dark-field image can be used to monitor the spatial drift while acquiring the EEL spectra. In this case, the actual collection angle is limited by the hole of the dark-field angular detector. The radius of the dark-field detector can be evaluated in diffraction mode by comparison with the entrance aperture of the spectrometer. In the HB501 microscope, the radius of the dark-field detector amounts to about half of the radius of the 2.0 mm entrance aperture, 1.0 mm. Therefore, in the case with the dark-field detector inside the column, the actual collection semiangle is about 6.0 mrad. The smaller collection angle can reduce the intensity of the spectra but enhance the signal-to-noise ratio. The raster images on the CCD detector with and without the dark-field detector are shown in the left of Fig. 3.8. The two raster images were obtained by firstly focusing the spectrometer and then removing the dark-field detector. The corresponding zero-loss peaks are given in the right of Fig. 3.8. Note that the measurement with or without the dark-field detector in the optical column might have some energy shifts and an inhomogeneous zero-loss peak, which results from different focusing conditions of the spectrometer. The energy shift and the inhomogeneous shape can introduce some artifacts into the acquired spectra. The inhomogeneous shape is due to the misaligned dark-field

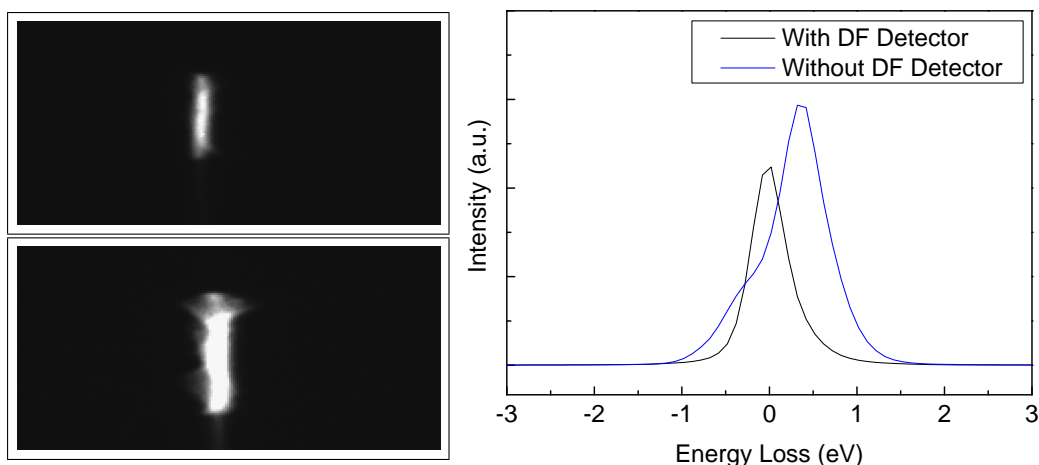


Fig. 3.8: Effect of the dark-field detector. The left is the raster images illuminated on the CCD detector with (top) and without (bottom) the dark-field detector in the optical column. The spectrometer is focused when the dark-field detector is pulled in, but without refocusing after it was pulled out. The right side show corresponding zero-loss peaks at a hole of specimen.

detector and the entrance aperture of the spectrometer. A shoulder can be seen in the left side of the peak. Such artifacts result in some unexplainable peaks or shoulders in the acquired core-loss edge. Due to this reason, the spectrometer should be refocused after the status of the dark-field detector is changed.

3.3.4 Beam Stability

Under ideal conditions, the beam current should be unvaried along the acquisition time. However, in actual experiments the long-term stability of the cold field emission gun (CFEG) is usually poor. A typical behavior of a CFEG is a rapid decline in emission just after flashing. Due to the sharpness of the CFEG tip, the field strength near the tip is very strong. Just the very strong field strength extracts the electrons from the tungsten tip. The molecules near the tip are polarized and absorbed onto the surface of the CFEG tip. The absorbed molecules reduce the field strength and then hamper the emission of electrons. Therefore, a flashing need to be periodically performed to evaporate the deposited molecules from the tip. The decay curve of beam intensity is given in Fig. 3.9(a). EEL spectra were acquired periodically at the zero-loss peak. Then, the total counts of the individual spectrum is used as a measure of the beam intensity. The beam intensity I is exponentially decreasing with the elapsed time and can be fitted by

$$I(T) = I_0 + b_0 * e^{-T/\lambda'}, \quad (3.5)$$

where I_0 is the beam intensity at infinite elapsed time, b_0 and λ' are coefficients, and T is the elapsed time after flashing. The burst peak at 20 minutes after the flashing might be caused by the deposition of dust onto the tip.

Another parameter of beam stability is the variation of full width at half maximum. The measured zero-loss peak has been fitted by a gaussian function. The variation of the FWHM along the elapsed time is shown in Fig. 3.9(b). The FWHM is slightly broadened linearly with the acquisition time. Some occasional noises with a large FWHM can be found

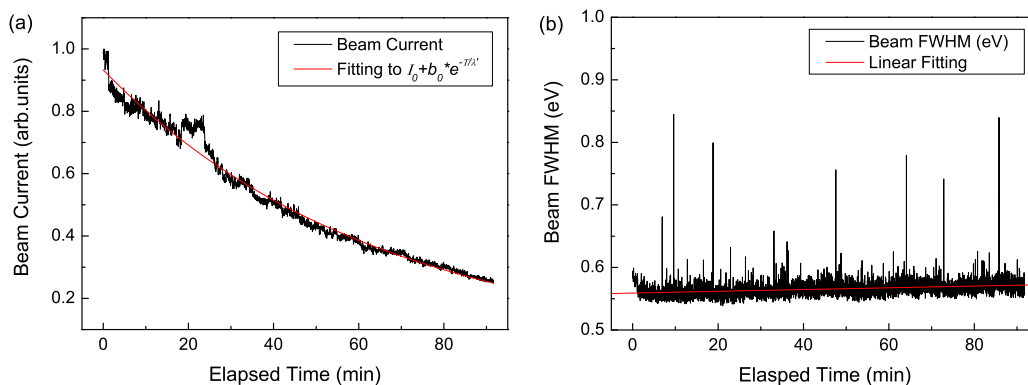


Fig. 3.9: (a) The declining curve of beam intensity along the elapsed time after flashing the tip. (b) The FWHM of the beam along the elapsed time.

in the figure. The noises should be caused when some molecules are absorbed on the FEG tip. Otherwise, the beam energy is not ideally fixed. The energy drift can be measured by periodically recording the energy position of the zero-loss peak. The measured result is shown in Fig. 3.10. One can see that the beam energy is varying in the range of ± 0.4 eV. The horizontal strips are caused by the selected energy dispersion of 0.1 eV/channel.

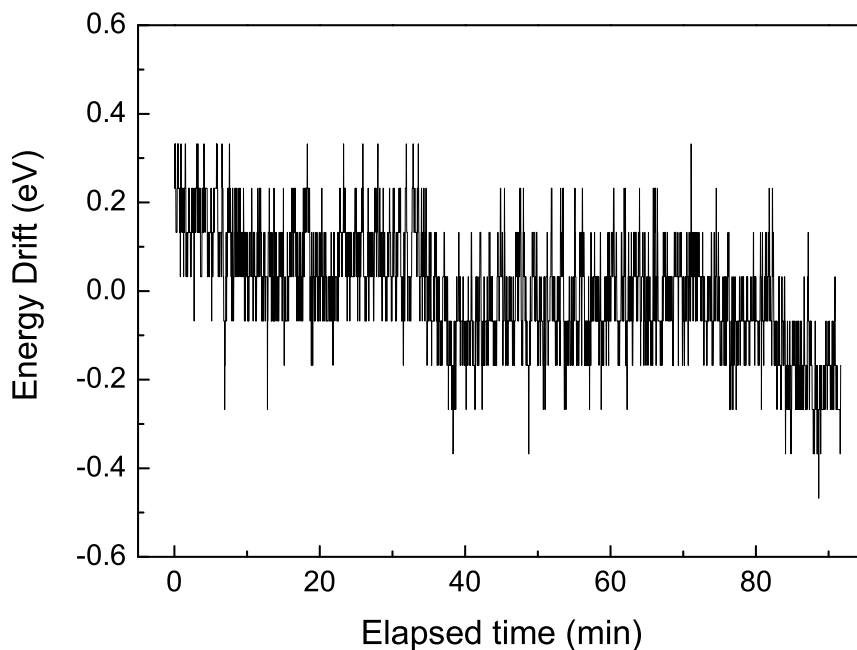


Fig. 3.10: Energy drift of the electron beam along the elapsed time.

3.3.5 Spatial Drift

When the electron beam illuminates the specimen, a small part of fast electrons and secondary electrons are trapped by the surface potential of the specimen around the probe position. For conducting materials, the charges can flow away immediately via the specimen holder and hence the surface-charging effect is small. But for insulator and semiconductor specimens, the charges aggregate and remain on the surface of the specimen. The Coulomb interaction between the electron beam and the charged surface result in a flip or spatial drift. The spatial drift does not affect the signal of bulk materials. For bright/dark field imaging, the spatial drift is usually not significant since the exposure time is very short in the magnitude order of 10 μ s per pixel. However, the spatial drift might be catastrophic upon acquiring EEL spectra. The spatial drift or flip of the specimen is the reason that a larger contribution of the EEL signals is recorded from the substrate or bulk regions far away from the the interface. Therefore, for insulating and semiconductor specimens, additional preparation procedures are required to avoid the surface-charging problem. In this thesis, an amorphous carbon layer with a thickness of several nanometers is deposited in a Cressington 208 Carbon Coater on the double surfaces of the cross-sectional specimen. A thin wire was used to shield the interface line from carbon coating in order to avoid carbon contamination. The shielding area should be as small as possible. Thus, the aggregated charges are able to flow away through the conducting carbon layer. Carbon coating can significantly reduce the spatial drift. One additional method is to acquire a line or square scan across the interface region. The line scan method is widely used in this thesis for reducing the acquisition time. The acquisition time per point was set as short as possible. Moreover, a small ROA can be helpful to decrease the spatial drift of the specimen. The lower current causes a lower accumulation of electrons. The direction of the spatial drift is roughly parallel or antiparallel to the line scan direction and might be also determined by the angle between the specimen surface and the electron beam.

3.3.6 Ghost Features

In EELS investigations, the thickness of the specimen is usually estimated in the low-loss region. When acquiring the zero-loss peak, the beam current should be reduced carefully. Otherwise, the over-saturated beam intensity will form ghost features in the acquired spectra. When the ghost features are overlapping with core-edge structures, they are very difficult to be distinguished and easily treated as a new feature, especially for the unknown materials. Fig. 3.11 shows the spectra of the Ti L_{23} edges taken from a $BaTiO_3$ thin film. In the upper spectrum the inverse ghost peak, at the 210th channel on the CCD detector, was overlapped with the satellite structures and led to two separated peaks, P1 and P2. The inverse peak was caused by an over-saturated beam during acquisition of the zero-loss peak. The lower spectrum was acquired with a shift of 205 channels to the high-energy side. The inverse ghost feature can be found in the pre-edge region of the lower spectrum. One way to remove the ghost peak is using a homogenous (or broadened) beam to illuminate the whole CCD area for some time, while a large number of readouts are performed.

3.3.7 Orientation of the Interface

The thickness of the interface (where the near-edge structures are different from those of bulk regions) is typically in the order of magnitude of several Angstroms and hence smaller than the spatial resolution of EELS/STEM. Therefore, the interface spectrum usually contains the contributions from the interface region and the bulk regions. The tilt of the interface will change its sensitive volume. Here, the term “sensitive volume” means the interface region interacting with the electron beam. When the electron beam parallels the interface, the sensitive volume has a maximum value. In this work, a simple model is proposed to

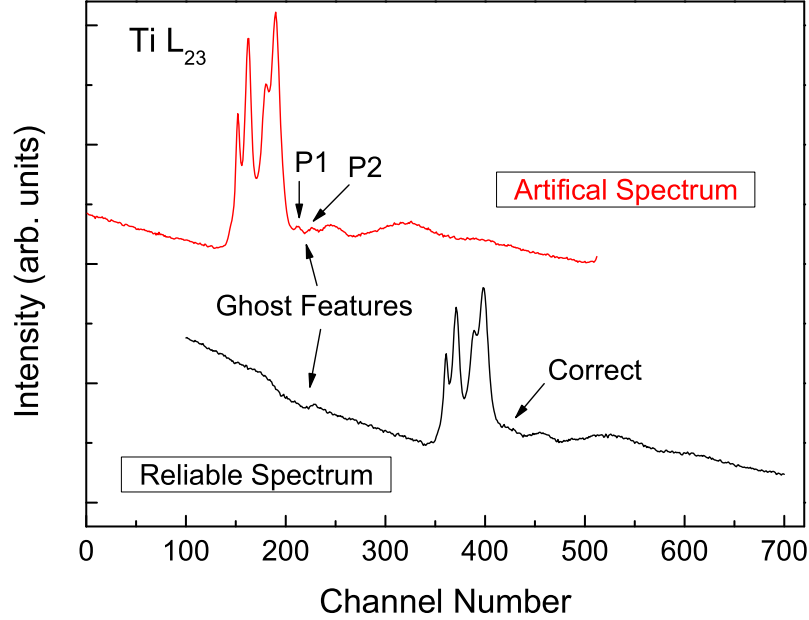


Fig. 3.11: Illustration on the effect of ghost features on the core-loss edge. In the upper spectrum the satellite structure of the Ti L_{23} edges are overlapped with ghost features caused by over-saturated intensity. In the lower spectrum the energy window is shifted to the higher-energy side by 205 channels.

estimate the orientation effect. The schematic illustration is shown in Fig. 3.12. The ratio of the sensitive volume to the total inelastic interaction volume is used to characterize the measurability of interface signals. With the assumption that the spatial resolution d is larger than the thickness of the interface t' and a cylindrical shape of beam in the specimen, the relationship between the sensitive volume ratio S and the tilt angle ϑ is given by

$$\begin{aligned}
 S &= V(\vartheta)/V_0, \\
 V(\vartheta) &= \frac{t'\pi(\frac{d}{2})^2}{\sin \vartheta}, \quad (\vartheta \neq 0) \\
 V_0 &= t_0\pi(\frac{d}{2})^2, \\
 S_{\max} &= V_{\max}/V_0, \\
 V_{\max} &= t_0(t'\sqrt{d^2/4 - (t'/2)^2} + 2R^2 \arcsin(t'/d)),
 \end{aligned} \tag{3.6}$$

where $V(\vartheta)$ is the sensitive volume at the tilt angle ϑ , V_0 the total volume interacting with the electron beam, and t_0 the thickness of the specimen. When the electron beam parallels to the interface plane $\vartheta=0^\circ$, the sensitive volume has a maximum value V_{\max} , while the maximum of the sensitive volume ratio is indicated by S_{\max} . In the cases of $t'=0.5$ nm and $t'=0.2$ nm, the sensitive volume ratio with the tilt angle are given in Fig. 3.13. The spatial resolution and the thickness of the specimen are assumed to be 1.0 nm and 100 nm, respectively. Typically, if the sensitive volume ratio is smaller than 10%, the interface signals are hard to be distinguished from the interface spectrum because most of the signals originate from bulk regions. One can see that the sensitive volume ratio for the 0.5 nm thick interface decreases to 10% as $\vartheta=2.8^\circ$. For a 0.2 nm thick interface, the tilt angle is about 1.0° as the

sensitive volume ratio decreases to 10%. Note that the maximum of the sensitive volume ratio is less than 100% because the thickness of the interface is smaller than the spatial resolution. This means that the sharper interface is more sensitive to the orientation effect. One way to minimize the orientation effect is utilizing the diffraction pattern of the substrate to check the orientation of the interface. However, the crystal appears more transparent when the electron beam parallels to low index directions. The intensity of core-loss signals becomes low. This is called “channelling effects” [64, 68]. The avoidance of channelling effects has to be considered additionally by a tilt of a small angle from low index directions.

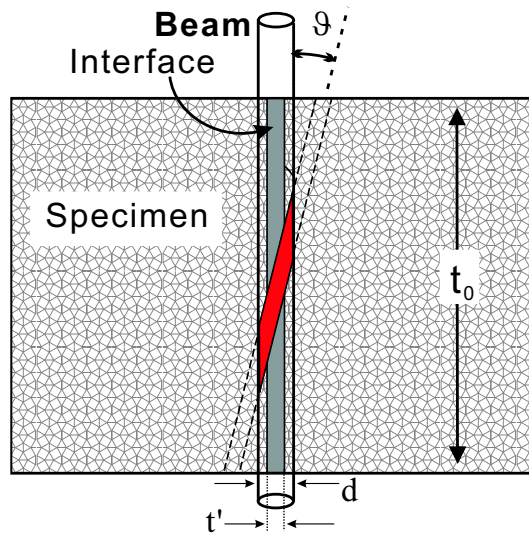


Fig. 3.12: Schematic illustration of the sensitive volume against the tilt angle ϑ between the electron beam and the interface plane. The red-color region indicates the sensitive volume as the interface tilted by the angle ϑ .

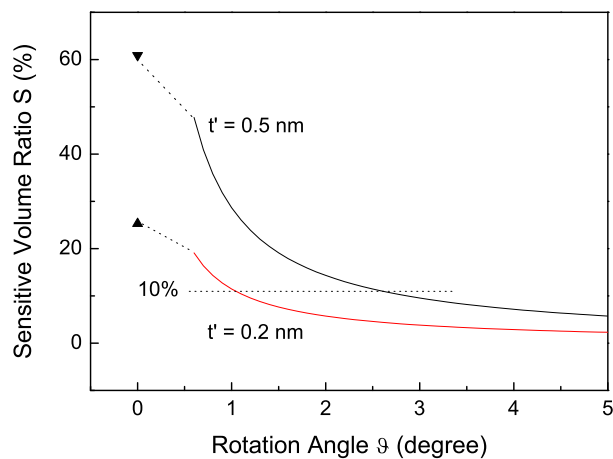


Fig. 3.13: The sensitive volume ratio against the tilt angle ϑ for the 0.5 nm thick and 0.2 nm thick interfaces under the conditions of $d=1.0$ nm and $t_0=100$ nm. The maximum of the sensitive volume ratio is given as a solid triangle.

Chapter 4

HR-EELS Investigation of BaTiO₃/SrTiO₃ Multilayers

The dielectric properties of BaTiO₃ thin films and multilayers are different from bulk materials because of nanoscale dimensions, interfaces, and stress-strain conditions. In this study, BaTiO₃/SrTiO₃ multilayers deposited on SrTiO₃ substrates by pulsed laser deposition have been investigated by high energy resolution electron energy-loss spectroscopy. The fine structures in the spectra are discussed in terms of crystal-field splitting and misfit strain. The near-edge structure of the oxygen K edge in BaTiO₃ thin layers and in bulk BaTiO₃ are simulated by Ab-Initio self-consistent full multiple-scattering calculations.

4.1 Introduction

Ferroelectric thin films are used for the development of next generation microwave controllers, frequency-agile filters, voltage-controlled oscillators, tunable microwave filters, non-volatile random access memories, etc. [69]. The dielectric permittivity can be controlled by applying a sufficiently high electric field. This field can be easily achieved in thin film structures using low control voltages below 50 V, which is necessary for high-density integrated electric devices. Recent investigations have been focused on barium strontium titanate (Ba,Sr)TiO₃ (BST) because of its high permittivity and specific capacitance. One of the most promising applications of BST is the use for very-high-density dynamic random-access memories [70]. High integration requires very small sizes of the electric devices, but the dielectric properties of many existing materials are different at nanoscale dimensions.

In order to grow high quality thin films on a certain substrate, many new techniques have been developed. Among them, pulsed laser deposition (PLD) is widely and successfully used. High-quality ceramic thin films can be obtained by PLD with carefully optimized oxygen pressure, substrate temperature, laser spot size, as well as other parameters like pulse repetition rate.

BaTiO₃/SrTiO₃ (BTO/STO) multilayers are promising in view of unique properties different from thin films and from bulk materials [71]. The dielectric properties of BTO/STO multilayers are predominated by the crystallization of the BTO layers and the interfaces between the BTO and STO layers. In this study, fine structures of the titanium L₂₃ edges and the oxygen K edge are investigated by EELS/STEM in multilayers consisting of BTO/STO layers deposited on SrTiO₃ (001) substrates by PLD.

4.2 Experiment

Two series of multilayer films were deposited on SrTiO_3 (001) substrates in the sequences STO (50 nm)/ BTO (10 nm) and STO (100 nm)/BTO (10 nm) by PLD, respectively, as shown in Fig. 4.1(a) and Fig. 4.1(b). Details of the growth and the TEM (transmission electron microscopy) preparation of the specimens studied in this work were similar to those described in Ref. [1]. For optimizing the probe size with a sufficient beam current, a $50\ \mu\text{m}$ objective aperture is used to restrict the convergence semiangle ($\sim 14\ \text{mrad}$). The details of the general experimental conditions of acquiring EEL spectra can be found in Chapter 3.

4.3 Results and Discussion

The cross-sectional TEM dark-field and STEM bright-field images of the multilayers are shown in Fig. 4.1(a) and (b), respectively. Fig. 4.1(c) gives the selected area diffraction pattern (SAD) taken from the region including both substrate and BaTiO_3 layer with the incident electron beam parallel to the [010] direction. The orientation relationship between BTO layers and the STO substrate can be obtained from the diffraction pattern: (001)

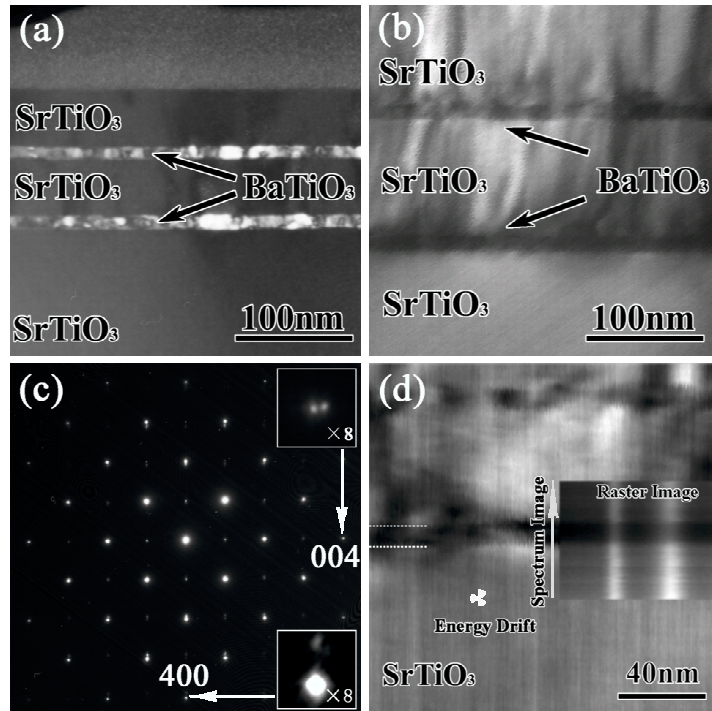


Fig. 4.1: (a) Cross-sectional TEM dark-field image of the multilayers consisting of STO (50 nm)/BTO (10 nm). (b) Cross-sectional STEM bright-field image of the multilayers consisting of STO (100 nm)/BTO(10 nm). (c) Selected area diffraction pattern from the interface region between the BaTiO_3 film and the SrTiO_3 substrate. The reflections from (400) and (004) planes are magnified eight times in the insets. (d) EEL spectra line-scan acquisition across a BTO layer. The energy drift was continuously monitored at the marked position. The white arrow indicates the scanning direction. The upper and lower interfaces are indicated by dashed white lines. The raster image, consisting of a series of spectra, is shown in the inset.

BTO || (001) STO, and [100] BTO || [100] STO. The [400] and [004] reflections (magnified in the insets) from BaTiO₃ and SrTiO₃ are well separated. The sharp reflections confirm that the BaTiO₃ layer is a high-quality single crystal layer. Because the lattice parameter ($a=3.905$ Å, Ref. [72]) of the SrTiO₃ substrate is stable and known very well, the reflections from SrTiO₃ can be used as a standard ruler to determine the lattice parameters of the BaTiO₃ layer without calibration of the camera length. The calculated lattice parameters of BaTiO₃ layers are summarized in Table 4.1. The lattice parameter a is close to that of a 12 nm thick BaTiO₃ single layer deposited on a SrTiO₃ substrate reported by Yoneda [71]. But the lattice parameter c in Ref. [71] might be overestimated since the volume of the unit cell should be a little smaller than that of bulk BaTiO₃ due to the presence of misfit strain (note that the lattice parameter a of the STO substrate is 2.3% smaller than that of bulk BTO). From Table 4.1, one can see that the lattice parameter is shortened in the growth plane and elongated along the growth direction (c axis) by the strain at the interfaces. In comparison with the BaTiO₃ thin film, the smaller lattice parameter in the growth plane indicates that the misfit strain is stronger in the BaTiO₃ layer than in the thin film due to the deposited SrTiO₃ film.

Table 4.1: Lattice parameters (a , b and c) of a 10 nm thick BaTiO₃ layer. For comparison, the data of a 12 nm thick BaTiO₃ thin film [71] and bulk BaTiO₃ (Ref. [73]) are given. V is the volume of the unit cell.

	BTO layer (10 nm)	BTO film (12 nm)	Bulk BTO
c (Å)	4.055	4.16	4.038
a, b (Å)	3.930	3.95	3.994
$V^{1/3}$ (Å)	3.970	4.02	4.008
c/a	1.032	1.053	1.011

4.3.1 Ti L₂₃ Edges

The ferroelectric properties of BaTiO₃ layers are related to the distortion of oxygen octahedra [74]. Although the lattice parameters can be obtained from the SAD pattern, the atomic positions within the unit cell cannot be extracted in a similar way. The ligand-field multiplet model has been successfully applied to identify the symmetry of oxygen octahedra in transition metal compounds [51]. It is derived that multiplet effects dominate the profile of the Ti L₂₃ near-edge structure in titanate perovskites. The density of unoccupied states of the Ti atoms are sensitive to short-range coordination. The four well split peaks in the Ti L₂₃ edges are attributed to excitations of $2P_{3/2}$ and $2P_{1/2}$ subshells to unoccupied t_{2g} and e_g states [75]. Peak positions, FWHM, asymmetry of the peak shape, satellite structures, and branch ratios [76] contain information about the atomic arrangement. As well known, bulk BaTiO₃ is found in a cubic perovskite phase above the Curie point ($T_c=120$ °C) and in a tetragonal phase at room temperature (cf. Fig. 4.2). The Ti atom lies in the center of the regular octahedron of oxygen atoms in the cubic perovskite structure, while the octahedron of oxygen atoms is distorted along the c axis in the tetragonal perovskite structure.

30 spectra were acquired along the direction indicated by the white arrow in Fig. 4.1(d). The acquisition time per spectrum was set to 10 s. A small spatial drift of the specimen due to the local charging effect has been corrected by the help of the raster image (inset in Fig. 4.1d). The BaTiO₃ layer of definite thickness can be used as a ruler mark. Thus, the position of the acquired spectrum can be corrected assuming a continuous drift of the specimen along the line scan direction. The average scanning step corrected by this method

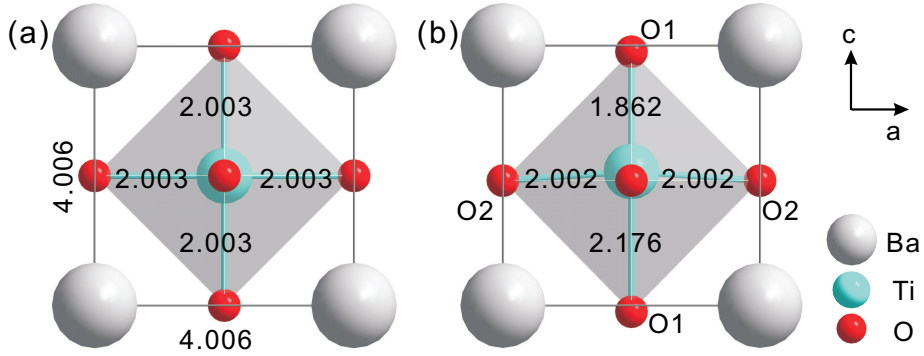


Fig. 4.2: (a) Cubic perovskite structure of bulk BaTiO_3 above the Curie point 120°C . The crystal data take from Ref. [77]. (b) Tetragonal perovskite structure of bulk BaTiO_3 at room temperature. The crystal data take from Ref. [73]. The labeled lattice parameters and Ti-O bond lengths are given in units of \AA .

amounts to about 1 nm, which is close to the estimated probe size. In order to correct the intrinsic energy drift of the electron beam, the zero-loss peak was monitored at the position marked in Fig. 4.1(d). However, this method can only limit the energy drift below $\pm 0.3 \text{ eV}$ because of the slight asymmetry of the zero-loss peak. Therefore, all EEL spectra contained in the raster image were normalized and energetically aligned to the t_{2g} peak in the L_3 edge, which was fitted by a Lorentzian function. By this method, changes in the crystal-field splitting smaller than 0.1 eV could be identified unambiguously.

For quantitative analysis, the Ti L_{23} edges are separated into four peaks by multi-peak

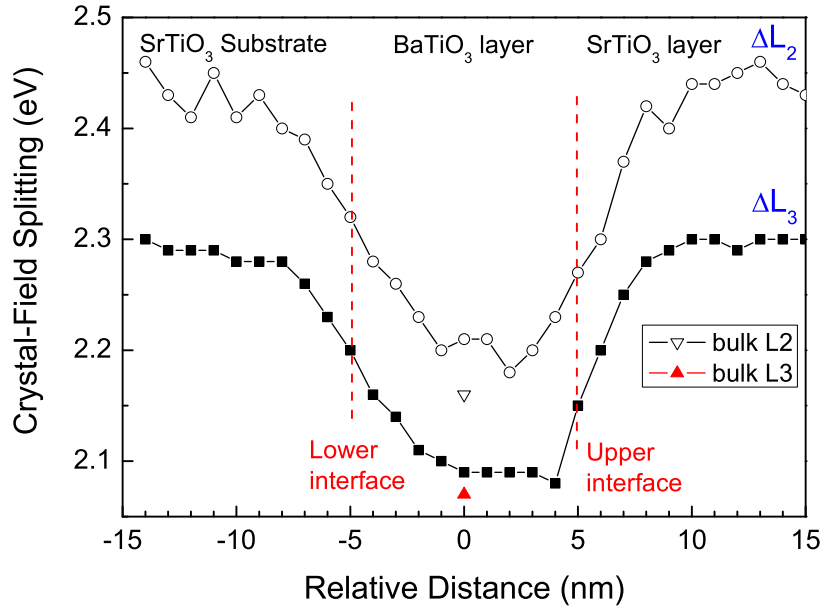


Fig. 4.3: Crystal-field splitting in the L_3 and L_2 edges across the BaTiO_3 layer. The vertical dotted lines indicate the interfaces positions. Additionally, the measured values for bulk BaTiO_3 are given as open and solid triangles.

Lorentzian fitting. Other fitting models, such as δ functions [75], could also be used. The coefficient of determination (R^2) of the Lorentzian fitting is better than 0.99 in this work, which means that the Lorentzian function is a reasonable model for the separation of Ti L_{23} peaks. For bulk BaTiO_3 (see Fig. 4.3), the crystal-field splitting of the Ti L_{23} edges amounts to only about 2.15 eV. Therefore, a high energy resolution is necessary to detect variations in the crystal-field splitting. The variation in the crystal-field splitting across the BaTiO_3 layer is shown in Fig. 4.3, where the abscissa gives the relative distance from the center of the BaTiO_3 layer. Note that the crystal-field splitting of the L_3 edge is obtained more accurately than that of the L_2 edge due to sharper peaks, more accurate pre-edge background fitting, and negligible plural scattering artifacts. The crystal-field splitting of the Ti L_2 edge is slightly larger (by ~ 0.12 eV) than that of the Ti L_3 edge in all layers. According to the results of crystal-field multiplet calculations of the Ti L_{23} edges for octahedral coordination of Ti with oxygen atoms [78], this small discrepancy is due to the different effect of the crystal field on the L_3 and L_2 edges. In Fig. 4.3, one can see that the slope of the lower interface is different from that of the upper interface. This slope is related to the relaxation of misfit strain at the $\text{BaTiO}_3/\text{SrTiO}_3$. The length of the relaxation is about 6 nm, which is in agreement with the TEM results of Visinoinu et al. [1]. Additionally, the crystal-field splitting of the BaTiO_3 layer is a little larger with respect to that of bulk BaTiO_3 . This difference can be interpreted by the misfit strain, which compresses the octahedra to reduce the Ti-O bond length. As known, the shorter Ti-O bond length leads to the stronger crystal field, which finally results in the larger crystal-field splitting.

Fig. 4.4 shows the L_{23} edges of Ti^{4+} in differently distorted octahedral coordinations. The octahedra share two edges with other octahedra in rutile, three edges in brookite, and four edges in anatase. They share six corners in the perovskite structure. The crystal

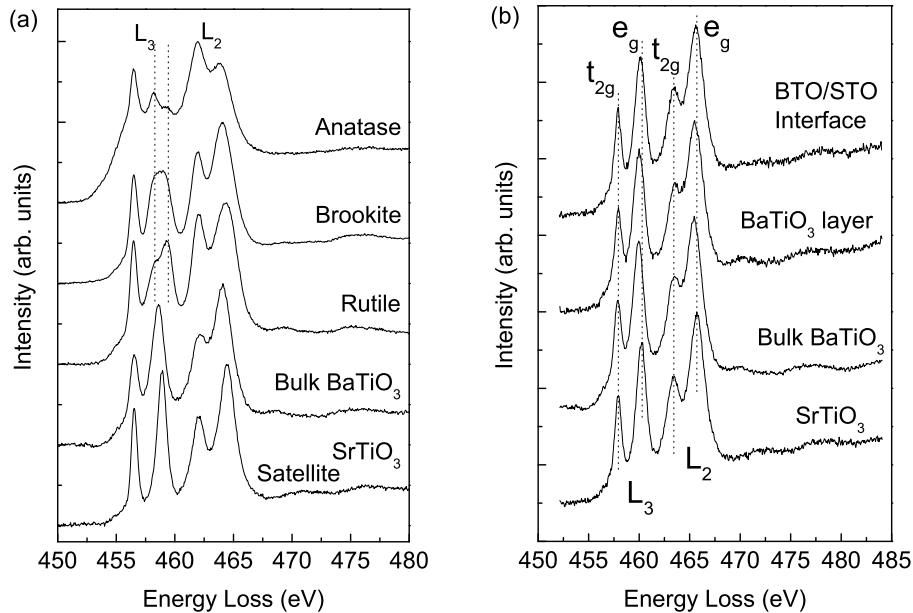


Fig. 4.4: (a) Experimental spectra of bulk BTO and STO compared to TiO_2 anatase, brookite, and rutile. The splitting of the e_g peak in the L_3 edge is indicated by vertical dotted lines. Satellite structures appear above the white lines. (b) Comparison of the fine structure of the titanium L_{23} edges measured in STO, BTO, and at the BTO/STO interface.

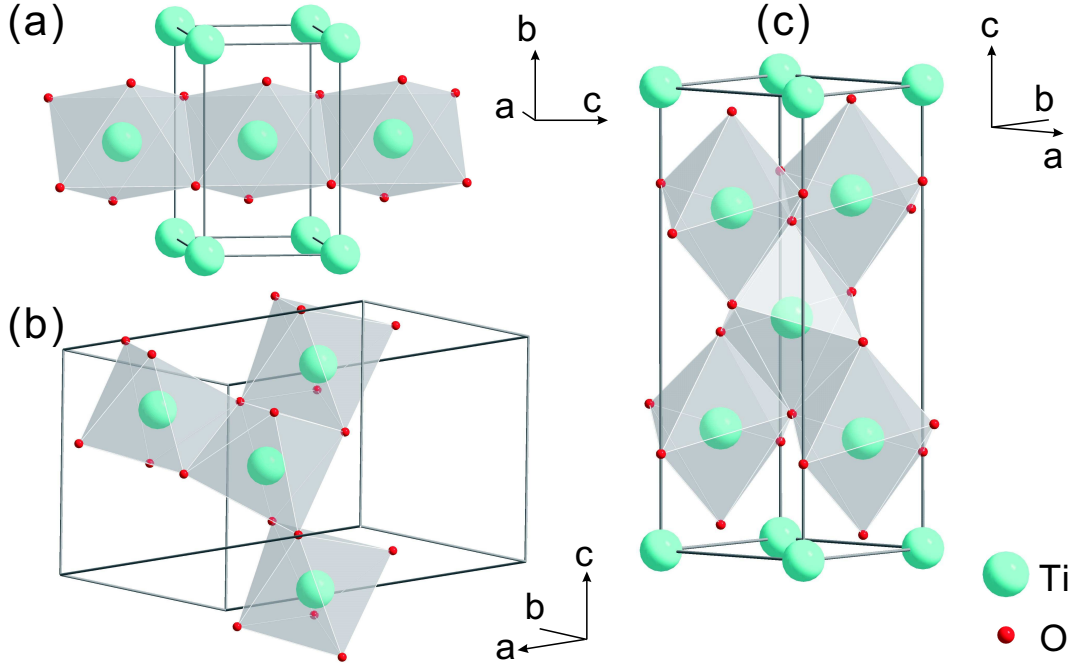


Fig. 4.5: Crystal structures of (a) rutile, (b) anatase, and (c) brookite.

structures of rutile, brookite, and anatase are sketched in Fig. 4.5. In the distorted cubic crystal field, the second main peak (e_g in the L_3 edge) is split into two peaks. Using atomic multiplet theory including the crystal field, de Groot calculated the Ti^{4+} L_{23} edge in O_h and D_{4h} symmetries, respectively [51]. No such splitting was found in O_h symmetry. The reproduced splitting of the L_3 e_g peak in D_{4h} symmetry was in good agreement with the experimental spectra of rutile TiO_2 , even though the octahedron in rutile is actually of D_{2h} symmetry. Therefore, this splitting is believed to be related to the distortion of the octahedral coordinations. With respect to molecular orbitals, the low-energy orbitals point to the ligands with the longer bond length, while the high-energy orbitals point to the ligands with the shorter bond length. In bulk BTO, the octahedron is in a D_4 symmetry, which can be regarded as a distortion of the D_{4h} symmetry. But a splitting has never been observed in the $\text{Ti } L_3$ e_g edge, neither in the experimental spectra of BTO layers nor in spectra of bulk BTO. This unidentified splitting in BTO might be due to the following reasons: (1) The splitting in perovskite titanate ceramics is too small to be separated in the spectrometer, or core-hole lifetime broadening and instrumental broadening smear out the small splitting. (2) The effect of crystal-field splitting in the edge-sharing structures is stronger than that in the corner-sharing structures. The low-energy peak relates to the shared edges, while the high-energy e_g peak relates to the ligand atoms. The relative intensity of the low-energy peak increases with the number of shared edges from rutile to anatase. Due to these reasons, the splitting of the e_g peak in other similar perovskite titanate ceramics, such as PbTiO_3 or ZrTiO_3 , may be also difficult to be observed. Fig. 4.4(b) shows the spectra taken at the BTO/STO interface and in the 10 nm thick BaTiO_3 layer. Spectra taken from SrTiO_3 (substrate) and bulk BaTiO_3 are also given for comparison. All of the spectra are also aligned to the first peak. The centers of the peaks are indicated by vertical dotted lines. There is no discriminable difference between the spectra from the BTO layer and bulk BTO. The spectrum at the interface can be regarded as the superposition of BTO layer and STO substrate spectra. Special fitting techniques, such as the multiple linear least-squares

(MLLS) fitting, may be appropriate for this case [79].

The Ti L_{23} edges can be reproduced by the Ab-Initio full multiple-scattering commercial code Feff8.20 (Ref. [80]). In SrTiO_3 , there are two satellite peaks above the Ti L_{23} edges with an energy separation of about 5.5 eV, which corresponds to the energy separation of the L_{23} edges. The Ti L_{23} edges were calculated shell by shell using the FMS method. The definition of the shell model is schematically illustrated in Fig. 4.6. The first shell contains six nearest-neighbor oxygen atoms with a distance of 1.952 Å to the central Ti atom. The second shell consists of eight Sr atoms with a distance of 3.382 Å. The third shell contains six Ti atoms with a distance of 3.905 Å. The result of calculations up to the sixth shell is shown in Fig. 4.7(a). The satellite structures can be well reproduced when the third shell (labeled 21 atoms) was considered in the cluster. In the simulation, the satellites of L_{23} edges were calculated, then weighted by a branching intensity ratio (I_{L_3}/I_{L_2}) of 0.8 (Ref. [81]) and then summed up. The result is in a good agreement with the experimental spectrum without any manual energy shift (cf. Fig. 4.7b). With regard of multiple-scattering, the satellites originate from backscattering at neighbor atoms; and the charge transfer process dominates the satellite structures. The satellites are shifted to lower energies by about 1.5 eV in BaTiO_3 with respect to bulk SrTiO_3 (cf. Fig. 4.4b). This means that the longer inter-atomic distance leads to a smaller charge transfer. The energy shift of the satellite peaks is more significant than that of the white-line peaks. In the near edge onset region (0-10 eV above the Fermi energy), the four main peaks can also be reproduced (not shown in the left part of the spectra in Fig. 4.7), but the relative intensity of the peaks is not in agreement with the experimental spectrum due to the neglect of multiplet effects (i.e., intra-atomic interactions redistribute the intensities of the peaks) which are more important than the charge transfer process for 3d transition metal atoms [54]. In other words, the excited electrons with a low kinetic energy are easily localized in unoccupied 3d states above the Fermi level. For the simulation of the L_{23} edges of transition-metal atoms, the agreement with experiment can be improved not only for the main peaks but also for the satellites by the charge-transfer and multiplet (CT-M) model [82] or multichannel multiple-scattering theory [83].

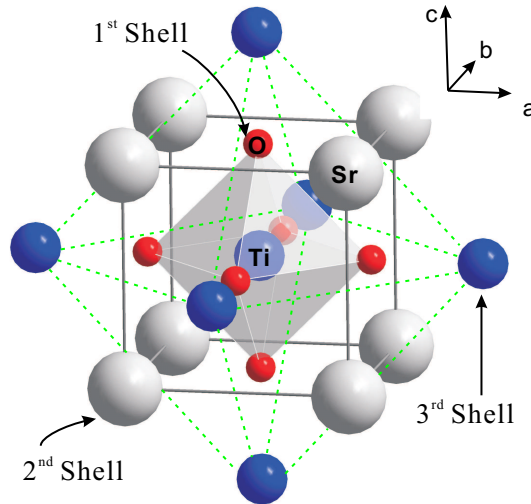


Fig. 4.6: Atomic coordinations up to three-shell around the Ti site in the FMS calculations of SrTiO_3 .

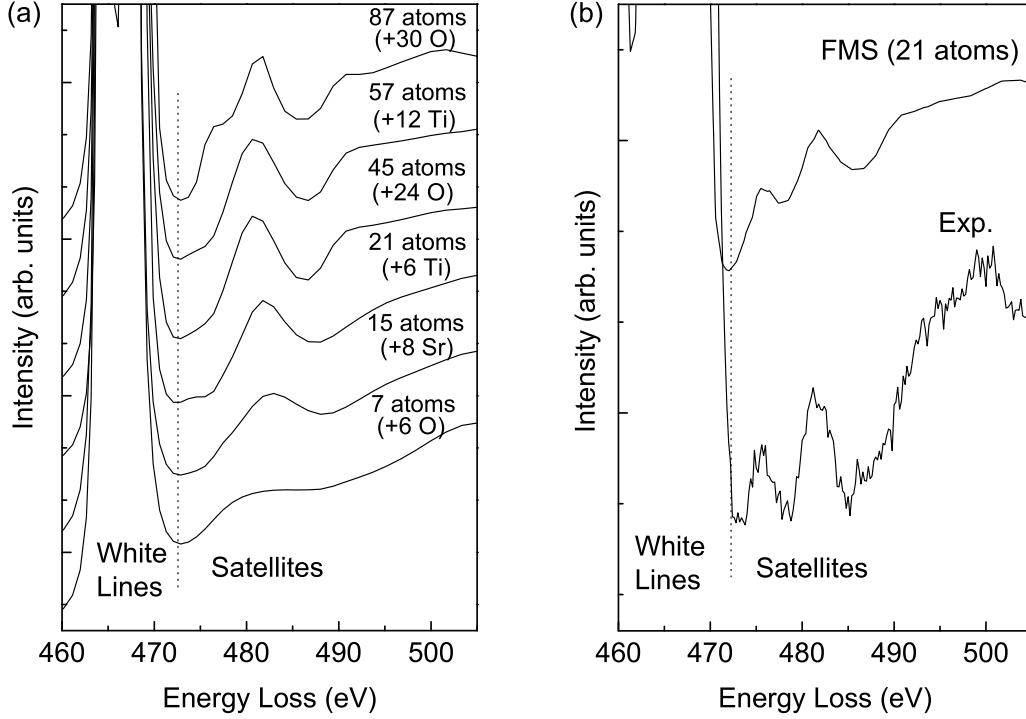


Fig. 4.7: (a) Satellite structures of the Ti L_2 edge of SrTiO_3 calculated in the shell-by-shell model of the FMS method. The spectra are labeled by the total number of the atoms in the clusters. The number of atoms in the new shell with respect to the previous cluster is indicated in parenthesis. (b) The experimental satellite structures of the Ti L_{23} spectrum compared with the FMS calculations of SrTiO_3 .

4.3.2 O K Edge

The fine structure of the O K edge was acquired with an energy dispersion of 0.2 eV/channel. The acquisition time per spectrum was set to 10 s for sufficient intensity. The fine structures of the O K edge are compared in Fig. 4.8(a). The spectra are aligned with respect to peak A1. The peaks A1 and A2 are related to the $3d$ orbitals of the Ti atoms. The separation between A1 and A2 amounts to about 2.4 eV, what reasonably coincides with the crystal-field splitting in the Ti L_{23} edges. The identical separation is one of the evidences of the hybridization of the oxygen $2p$ orbitals with the Ti $3d$ orbitals. This interpretation corresponds to the explanation of de Groot in terms of ligand-field splitting [84].

In order to identify the origin of the features B1, B2, C1 and C2, the O K edge of bulk BaTiO_3 was simulated by FMS calculations shell by shell using the parameters given in Table 4.1. Overlapped self-consistent muffin-tin potentials were used to reduce the effects of potential discontinuities at the muffin-tins. As shown in Fig. 4.2(b), there are two unequal positions for oxygen atoms in the tetragonal perovskite structure, labeled O1 and O2. One O1 and two O2 oxygen atoms are included in one unit cell. The spectra from the two unequal oxygen atoms were calculated, respectively. Then the spectra were multiplied by the corresponding number of atoms in the unit cell and summed up. The results of the calculation of BaTiO_3 layers and bulk BaTiO_3 , including 107 atoms in the individual cluster, are in a good agreement with the main features of the experimental spectra, as shown in Fig. 4.8(b).

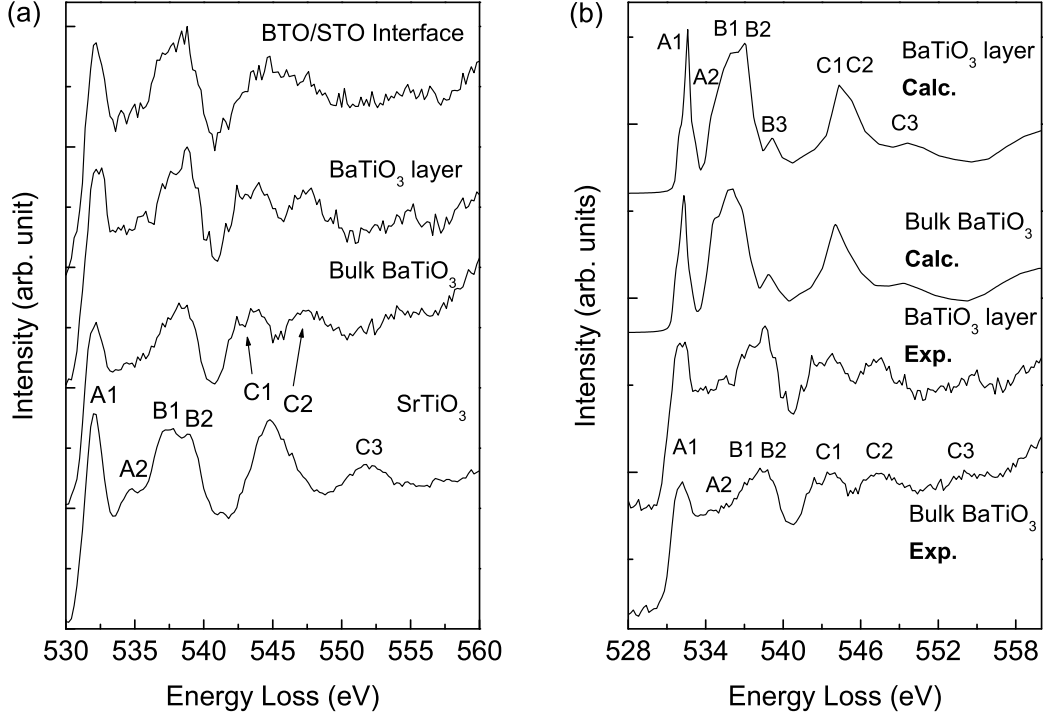


Fig. 4.8: (a) Comparison of the fine structure of the oxygen K edge. The reference spectra measured in bulk BTO and STO were averaged from 5 spectra taken from different positions. (b) Experimental and simulated oxygen K edges of bulk BaTiO_3 and BaTiO_3 thin film. The lattice parameters for simulations are given in Table 4.1.

The difference in the spectra calculated for a BTO layer and bulk BTO is very small, which agrees with the experimental results. This means that the strain-induced distortion of the BTO structure is not the main reason for the difference in the dielectric properties of a BTO layer and bulk BTO. Interface effects have to be taken into account. The details of the FMS calculations will be discussed in Section 4.4. The origins of peaks A1-C3 are discussed in the following. Peak A1 is related to the hybridization of the O $2p$ and Ti $3d$ orbitals. Peak A2 is also related to the hybridization, but its intensity is very low, which is consistent with the experimental spectrum. Peaks B1, B2 and B3 originate from the backscattering of the electron wave at the nearest Ba shell. The peak C1 arises from the backscattering at the nearest oxygen shell. The experimental energy splitting between C1 and C2 amount to about 3.8 eV. However, this splitting cannot be well reproduced in the FMS simulations. This disagreement might be caused by the fact that the polarization potential along the c axis is neglected in the FMS calculations of BaTiO_3 . The polarization potential is generated by the displacement of Ti atoms in the octahedra along the same direction, which breaks the symmetry of the nearest oxygen atoms around the excited oxygen atom [85]. Peak C3 is mainly related to scattering at the third oxygen shell. In multiple-scattering calculations, the fine structure in the spectra predominantly arises from strong backscattering at neighbor oxygen atoms. Contributions from distant cations are usually small.

4.3.3 [Ti]/[O] Ratio

The [Ti]/[O] element ratio was calculated by a standard procedure which implemented in the DigitalMicrograph software packages. In this procedure the total counts of the core edge signals of two elements are integrated in an energy window ($\sim 50\text{eV}$) above the threshold energy, which are assumed to be I_a and I_b . The corresponding cross sections, σ_a and σ_b , are calculated by a Hartree-Slater model. Then, the element ratio is given by $I_a\sigma_b/I_b\sigma_a$. The details of the calculations can be found in Ref. [64]. A 10 eV energy window in the pre-edge was used to fit the background for both core-loss edges. The integrated intensities of the Ti L_{23} edges and the O K edge were calculated up to 45 eV and 60 eV above the corresponding threshold energies, respectively. Fig. 4.9 shows the element ratios across the BaTiO_3 layer. A slight slope caused by the nonuniform thickness has been corrected by subtracting a fitted line. A significant increase (around 6%) of the [Ti]/[O] ratio is found reproducible at several different positions at the upper interface of the BaTiO_3 layer, while no detectable increase is found at the lower interface. The increased [Ti]/[O] ratio implies that oxygen vacancies are aggregated at the upper interface. Similar results have been reported for grain boundaries [20, 86] and dislocation cores [23]. The [Ti]/[O] element ratio in the region far from the interface fluctuates in the range of 0.33 ± 0.03 , which is mainly caused by the removal of the background.

Since the surface of the STO substrate was prepared to terminate at the TiO_2 plane [1],

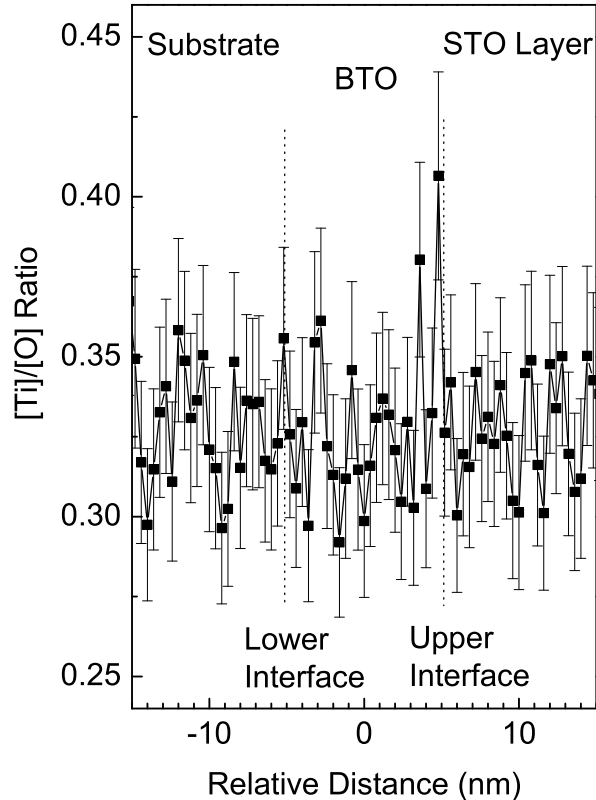


Fig. 4.9: [Ti]/[O] ratio across the BaTiO_3 layer. The vertical dotted lines indicate the upper and lower interfaces. The abscissa denotes the relative distance from middle of the BTO layer.

the molecules were deposited at the beginning of the growth process on the STO surface in the stacking sequence $\text{BaO-TiO}_2\text{-BaO-TiO}_2 \dots$ due to energetic reasons. In the first few layers (< 5 nm), the misfit strain from the interface makes the energetic preference strong, which causes that this region is free of defects. When the BTO layer becomes thicker, the misfit strain is relaxed. However, the misfit-strain-induced polarization along the growth direction retains in the whole BTO layer. In perovskite oxides, oxygen vacancies can order at the grain boundaries [87]. Oxygen vacancy ordering mechanism may occur in the BaTiO_3 thin layer under the influence of misfit strain because the stacking sequence is not rigorous [88]. This may be one of the possible explanations for the formation of space charge layers [71] at the rough upper interface of BaTiO_3 layers [1]. The presence of a space charge at the upper interface dominates the difference of dielectric properties between multilayers and bulk BaTiO_3 .

4.4 Explanation of Fine Structures of the O K Edge

In the previous section, FMS calculations have been performed to interpret the fine structures of the oxygen K edge in BaTiO_3 . However, the accuracy of the FMS calculations is not very high. Therefore, some details of the fine structures have been smeared out, especially for the peaks C1-C3 in BaTiO_3 . More accurate theoretical calculations are needed to explain the splitting feature. In this section, the combination of FMS and band-structure methods will be used to interpret the features of the oxygen K edge in BaTiO_3 . As a starting point, the calculations are performed for SrTiO_3 firstly, and then extended to BaTiO_3 .

4.4.1 Bulk SrTiO_3

For the oxygen K edge, only $1s \rightarrow 2p$ transition is allowed according to the dipole selection rule. Multielectron effects, transition matrix elements and the core-hole potential have a negligible influence on the fine structures of the oxygen K edge [55]. Therefore, the partial density of states can be reasonably compared with the experimental oxygen K edge directly. In this work, a widely used FLAPW code, Wien2K, is used to do the work due to its high accuracy on electronic structure calculations. As a starting point, the oxygen p DOS of SrTiO_3 is firstly calculated, because SrTiO_3 has a perfect perovskite structure. BaTiO_3 has a similar perovskite structure except a small distortion along the Z-axis (cf. Fig. 4.2(b)). The unit cell parameters of SrTiO_3 are taken from Ref. [72] and listed in Table 4.2 including the muffin-tin radius of each different atom used in the present calculations. The atomic structure of unit cell is schematically shown in Fig. 4.10. The three oxygen sites have the equivalent coordinations. Indeed, for reducing the computing afford in the actual calculation, the $(1/2, 0, 1/2)$ and $(0, 1/2, 1/2)$ oxygen sites have been rotated onto $(1/2, 1/2, 0)$ by a so-called “local rotation matrix”. The $(1/2, 0, 1/2)$ site changes to $(1/2, 1/2, 0)$ by a 90° rotation about Y axis, and the $(0, 1/2, 1/2)$ site by a 90° rotation about X axis. The muffin-tin radii for Sr, Ti and O are listed in Table 4.2 in units of the Bohr radius. The self-consistent calculation is performed by using a $10 \times 10 \times 10$ k-point

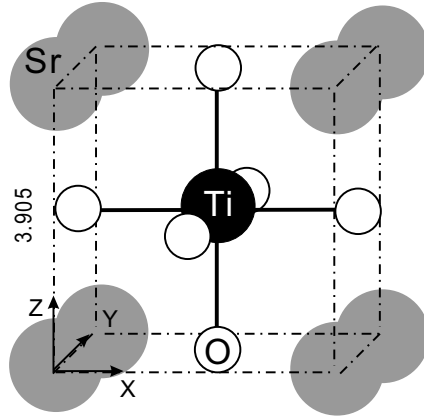


Fig. 4.10: Perovskite structure of SrTiO_3 . The lattice parameter is given in units of \AA .

sampling in the irreducible Brillouin zone (IBZ). The present calculation with 1000 k-points is close to the calculation with a $20 \times 20 \times 20$ k-point sampling in the literature [89].

Table 4.2: Unit cell parameters of bulk SrTiO_3 with a perovskite structure (Space Group $\text{Pm}\bar{3}\text{m}$), taken from Ref. [72]. The lattice parameter is $a=3.905$ Å. The muffin-tin radii R_{MT} used in the FLAPW calculations are given for all different atoms in units of the Bohr radius.

	x	y	z	R_{MT}
Sr	0.0	0.0	0.0	2.3
Ti	0.5	0.5	0.5	1.9
O	0.5	0.5	0.0	1.6

The oxygen p DOS at $(1/2, 1/2, 0)$ site compared with the ELNES of the oxygen K edge is shown in Fig. 4.11. Note that the same Cartesian coordinate is used for the orientation-projected DOS as that of the unit cell. The orientation-decomposed components are also shown in this figure. The same series of labels as in Fig. 4.8 are adopted for the features in the spectrum. One can see that the peaks A1-A2, B1-B3, and C1-C3 are well reproduced in the calculated oxygen p DOS. The spectra have been aligned to the position of the first peak. The present calculation by FLAPW method are well consistent with the results of Ref. [55] by localized spherical wave (LSW) method. The oxygen p DOS has been broadened by 0.1 eV FWHM with a Gaussian distribution. Herein, a smaller broadening is used in order to show the details of the structures. The calculated band gap in this work is about 2.0 eV which is reasonable in comparison with the experimental value of 3.2 eV. The underestimation of the band gap is a well-known feature of LDA method due to the inadequacy to describe the electron excitation directly by the ground state density of states with an one-electron approximation [41].

The orientation-decomposed p DOS provides the possibility of analyzing the origin of the individual feature in the spectrum. The oxygen p DOS can be decomposed into three components along X, Y and Z axes. The label ‘‘PZ’’ means the projection of the p DOS on Z-axis. The label ‘‘PX+PY’’ indicates the PX or PY projection of the p DOS. The features in the oxygen p DOS are related to the Sr-O, Ti-O and O-O interactions. Thus, the site-projected DOS of SrTiO_3 are drawn in Fig. 4.12 in order to analysis the relationships. The total DOS of the Sr and Ti sites are decomposed into the corresponding partial DOS, and the d DOS of Sr and Ti are additionally decomposed into D-eg and D-t_{2g} components. The orientation-decomposed p DOS of oxygen at $(1/2, 1/2, 0)$ is drawn again for completeness.

In Fig. 4.11, peak A1 at 3.8 eV is almost entirely from the PX+PY component. At the same time, this peak relates to the D-t_{2g} component in the Ti d DOS (cf. Fig. 4.12b). That means that peak A1 originates from the pd hybridization between titanium and oxygen with a π -bonding character. Similarly, peak A2 is only found in the PZ component and relates to the e_g component in the Ti d DOS. Therefore, peak A2 arises from the Ti-O pd hybridization with a σ -bonding character. The e_g component of the Ti d DOS is spread out from 4.0 to 9.0 eV, which can be seen in Fig. 4.12(b). The double peaks at 5.2 and 6.8 eV can also be found in the PZ component of the oxygen p DOS. In the calculated Ti d DOS, the intensity of peak e_g is much weaker than that of peak t_{2g}, which is not correct in comparison with the ELNES of the Ti L₂₃ edges in bulk SrTiO_3 in Fig. 4.4(a). This disagreement is caused by the neglect of multiplet effects (or the interactions between core-hole and the crystal-field) for the titanium cations in the ground state calculations. Multiplet effects predominate the Ti L₂₃ white lines. However, there is no significant multiplet effects on the oxygen K edge. The intensity of peak A2 is much weaker than that of peak A1, which is consistent with the relative intensity of peak e_g and t_{2g} in the Ti d DOS. This result is in agreement with the

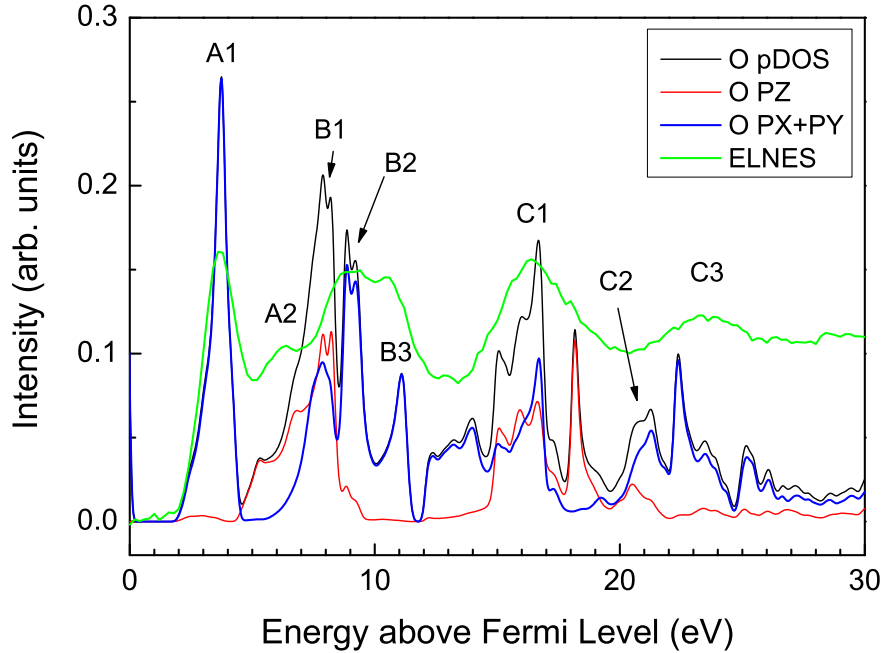


Fig. 4.11: Ground state oxygen p -projected density of states compared with the ELNES of the oxygen K edge for SrTiO_3 . The oxygen p DOS is decomposed into three components along X,Y,Z-axis.

experimental findings.

Now, let's look at the peak B1 in Fig. 4.11. Firstly, peak B1 is spread out in the range of 5.0-8.5 eV. It is overlapped with the peak A2. Peak B1 arises from both PZ and PX+PY components of oxygen p DOS. The PX+PY contribution is related to the Sr D-eg component, which can be seen from Fig. 4.12(a) and (c). The peak at about 8.0 eV in the PX+PY component can also be found in the Sr D-eg component at the same energy position. The B1 contribution from the PZ component of oxygen p DOS is mainly related to the Sr D-t_{2g} component. Similar to the Ti-O bonding, the interactions between oxygen PZ and Sr D-t_{2g} projected orbits have a π -bonding character, as well as the interactions between oxygen PX+PY and Sr D-eg orbits have a σ -bonding character. In the oxygen p DOS, peak B2 is almost entirely related to the PX+PY component. Mainly the Sr d DOS and partially the Ti D-t_{2g} component contribute to this peak. Peak B3 is entirely from Sr DOS, which can be seen from Fig. 4.12(d). According to the decomposed Sr DOS in 4.12(a), peak B3 is contributed from Sr s DOS (s -character density of states) and d DOS components. Thus, peak B3 in oxygen p DOS has s and d characters indeed, which is forbidden by the dipole-transition rule. This is the reason why peak B3 almost disappears in the experimental spectrum. In comparison with the ELNES in Fig. 4.11, peak B1 is shifted to a lower energy by about 1.0 eV as well as 1.5 eV for peak B2. This difference is caused by the neglect of the core-hole effect in the DOS calculations. The core-hole potential tends to hamper the electron transition from a core level to the unoccupied density of states. That causes a little higher energy loss in the EELS experiments.

Peak C2 and C3 can not be well separated in SrTiO_3 due to intrinsic and instrumental broadenings. It might be difficult to assign the peaks in the range of 12-25 eV to C1, C2 and C3. Fortunately, a clear assignment can be given in the calculations for BaTiO_3 , which will be discussed later. Due to similar atomic structures of BaTiO_3 and SrTiO_3 , the assignment

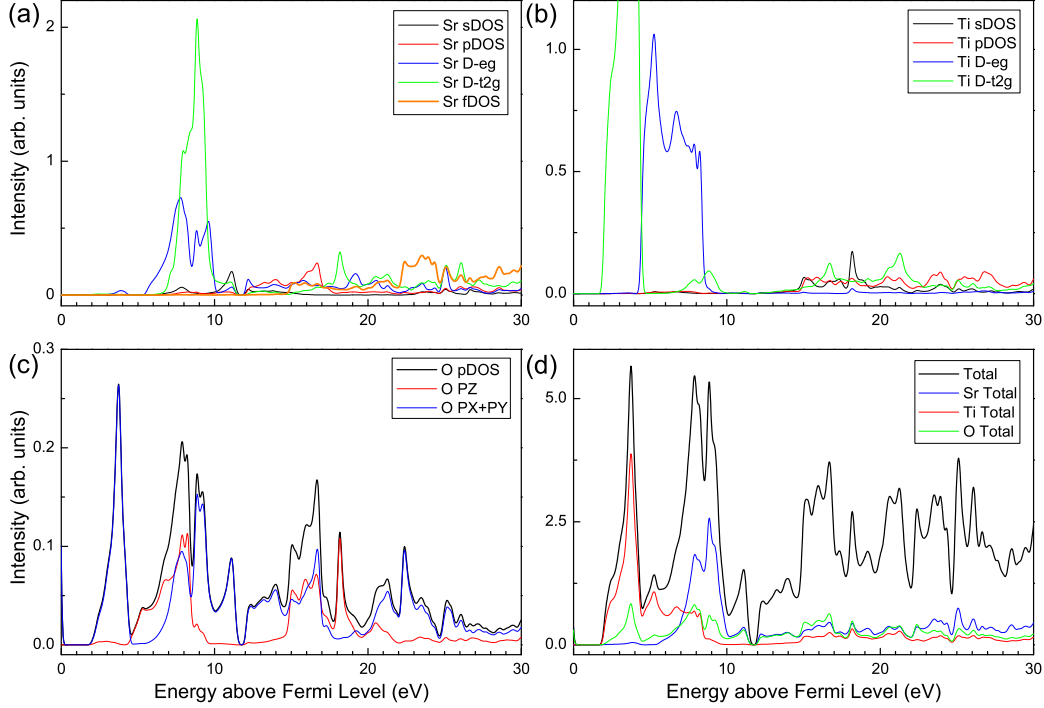


Fig. 4.12: The site-projected density of states of SrTiO_3 (a) Sr, (b) Ti and (c) O, coupled with the corresponding l -projected or orientation-projected decompositions. The total DOS of SrTiO_3 are shown in (d).

for peaks C1–C3 can be given as labeled in Fig. 4.11. Peak C1 is located at about 16.7 eV which is very close to the experimental value of 16.3 eV. Peak C2 is located about 21 eV in the calculated p DOS. This peak is overlapped by the peak C3 at about 22.5 eV. The energy separation between C1 and C2 amounts to about 4.3 eV. Due to the larger broadening at higher energies, the separation between C2 and C3 is completely smeared out in the electron energy-loss spectrum. Peak C1 comes partly from PX+PY and PZ components, while, peak C2 is mainly related to the PX+PY component with a small contribution from the PZ component. According to the partial DOS of Sr and Ti atoms, peak C1 might be related to Sr p DOS, Sr D-t2g, Ti s DOS and Ti D-t2g components, while peak C2 is related to Sr d DOS, Ti p DOS, and Ti d DOS components according to the identical peak positions. Peak C3 is spread out in the range from 22 to 27 eV. The peak position is at about 22.5 eV in comparison with the experimental value of 23.5 eV. The explanation of the energy shift of 1.0 eV is the same as those of peaks B1 and B2 mentioned above in terms of core-hole effect. Peak C3 is entirely from the PX+PY component, which may be also related to Sr d DOS, Ti p DOS, and Ti D-t2g components. Even though peaks C1–C3 have been interpreted by Sr–O and Ti–O interactions, the relative intensities of peaks C1–C3 are not correct if the interpretation is only given by the Sr–O and Ti–O interactions. The fine structures above 12 eV should be dominated by O–O interactions.

The discussion above shows a reasonable way to interpret the fine structures by cation-anion interactions. But oxygen-oxygen interactions cannot be directly incorporated. O–O interactions are usually important in oxide compounds. They dominate the fine structures in the high-energy region in the electron energy-loss spectrum. It is not surprising because the repulsion between the ejected electron and the negatively charged oxygen neighbors has

the trend to increase the energy loss of the oxygen K edge. In fact, the fine structures of the oxygen K edge should be interpreted by the combination of Ti-O, Sr-O and O-O interactions. As known, the multiple-scattering method can get an excellent consistency with the experiments in the extended energy-loss fine structure (EXELFS) region. The combination of multiplet-scattering and band-structure methods should give a better understanding of the features in the oxygen ELNES spectrum.

The FMS method has the ability to consider the backscattering of the individual shell. The present FMS calculations take into account six shells around the oxygen site. The shell structure is shown in Fig. 4.13. The first shell only includes two titanium atoms along the Z-axis with the distance of 1.592 Å to the excited oxygen atom. The second shell (the 1st oxygen shell) includes eight nearest-neighbor oxygen atoms with a distance of 2.761 Å. The eight oxygen atoms occupy the eight corners of a rhombohedron with the lateral lengths of 2.761 Å in the X- and Y-axis and 3.905 Å in the Z-axis. The third one contains four strontium atoms lying in the XY plane. The distance to the central atom amounts to 2.761 Å. The fourth shell (the 2nd oxygen shell) contains six oxygen atoms in octahedral symmetry around the central atom. The shell-distance is 3.905 Å. The fifth shell is comprised of eight titanium atoms, which occupy the eight corners of a rhombohedron with the lateral lengths of 3.905 Å in the Z-axis and 5.523 Å in the X- and Y-axis. The distance to the central atom of this shell is 4.366 Å. The last shell has a distance of 4.783 Å to the central atom. Sixteen oxygen atoms are included in this shell and occupying the sixteen corners of a decahedron.

In the FMS calculations, the scattering potential is self-consistently calculated in a cluster with a radius of 5.0 Å, which contains 53 atoms. The FMS calculations of the oxygen K edge in SrTiO_3 following this shell model are shown in Fig. 4.14. The labels for the individual spectrum at the right side indicate the total number of atoms in the FMS cluster. When the six shells with 45 atoms are included in the cluster, all major peaks are reproduced in comparison with the 165-atom cluster. In the FMS calculations, the core-hole effect is taken into account. Peaks A1 and A2 can be reproduced in the 3-atom cluster. Peak A1 is sharp, but peak A2 spreads over a wide range of 535-540 eV. When the eight nearest-neighbor

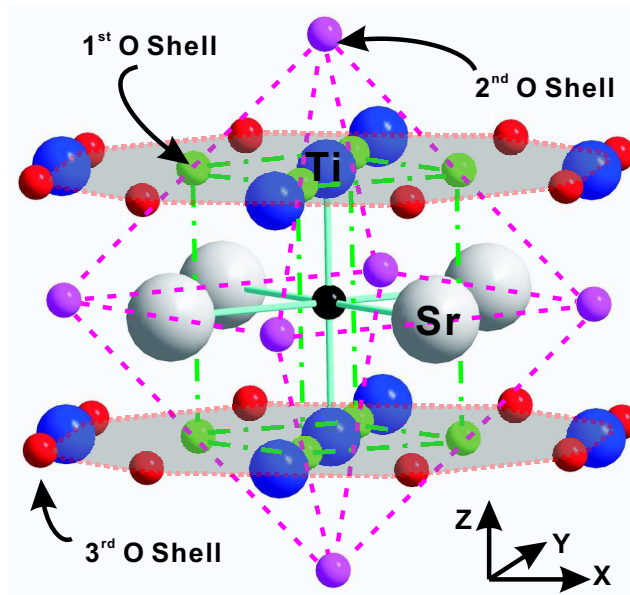


Fig. 4.13: Atomic coordination with up to six shells (three oxygen shells and three Sr-Ti shells) around the oxygen site at $(1/2, 1/2, 0)$. The lateral lengths of the oxygen hexahedron are given in units of Å.

oxygen atoms are appended, peak C1 is well reproduced. As the four nearest-neighbor barium atoms are considered, Peaks B1, B2 and B3 are reproduced, but peaks B1 and B2 are strongly overlapped the broadened peak A2. The second nearest-neighbor oxygen shell has a small contribution between peaks C1 and C3. This contribution is assigned to the peak C2, which is strongly overlapped the peak C3 according to the calculated oxygen p DOS in Fig. 4.11. The second nearest-neighbor titanium atoms have a very small influence on the fine structures above 12 eV. This is caused by their small scattering cross sections for the electron wave. Peak C3 is mainly related to the third nearest-neighbor oxygen shell, which can be seen from the 45-atom spectrum.

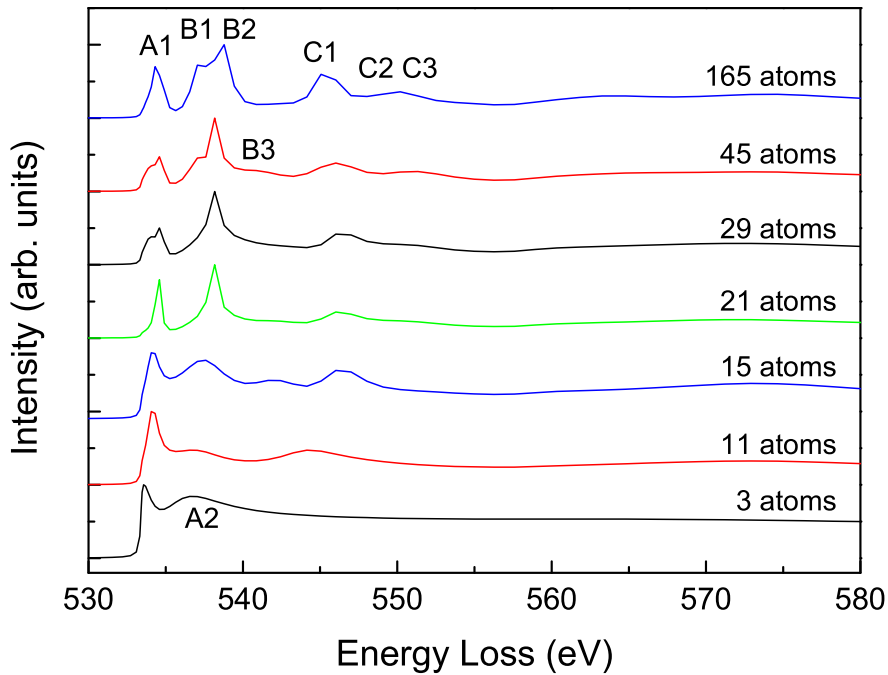


Fig. 4.14: FMS calculations of the oxygen K edge for SrTiO_3 in shell-by-shell model.

In conclusion, peaks A1-A2 are dominated by Ti-O bonding, peaks B1-B3 by Sr-O bonding. Peaks C1 is mainly related to the nearest-neighbor oxygen shell, as well as peaks C2 and C3 are mainly related to the second and the third nearest-neighbor oxygen shells, respectively. Although peaks C1-C3 have identical peak positions to the corresponding peaks in Sr DOS and Ti DOS, the amplitudes are mainly dominated by the surrounding oxygen atoms. Herein, the term of a “shell field” is introduced, which represents the local field of the corresponding shell felt by the excited electron from the core level. This definition is similar to the conventional definition of “ligand field” or “crystal field”. For a neighbor cation shell, the shell field has a trend to facilitate the electron excitation due to the attraction on the ejected electron. That makes the corresponding excitation slightly easier. Vice versa, the neighbor anion shell has a trend to hamper the corresponding excitation by repulsion, which makes the corresponding excitation energy slightly higher. For the Ti^{4+} shell, its shell field is slightly stronger than that of the Sr^{2+} shell. Therefore, the Ti-related features are located in the lower-energy region and the Sr-related features in the higher-energy region. Due to the repulsion of the negatively charged oxygen shell on the ejected electron, the O-O interaction related features C1-C3 present in the higher-energy region of the spectrum. The

energetic sequence of peaks C1-C3 may be explained by the electron hopping mechanism. The ejected electron can be more easily transferred to the nearest-neighbor oxygen atoms than the other oxygen atoms. From the point of view of the multiple-scattering, higher energy of the photoelectron wave is needed to reach higher oxygen shells.

4.4.2 Bulk BaTiO_3

The interpretation of the fine structures of the oxygen K edge in BaTiO_3 is similar to that of SrTiO_3 due to the similar atomic structure. Firstly, the unit cell parameters of bulk BaTiO_3 , which are listed in Table 4.3, are taken from Ref. [73]. The atomic structure of the unit cell can be seen in Fig. 4.2(b). There are two inequivalent oxygen positions in the unit cell, which are labeled O1 and O2, respectively. O1 takes the position (1/2,1/2,-0.024) and O2 takes the positions (0,1/2,0.48) and (1/2,0,0.48). The atomic coordinations of O1 and O2 sites are schematically shown in Fig. 4.15. The major difference between the local environments of the O1 and O2 sites is the rotation of the nearest-neighbor oxygen atoms which surround the O1 site in a tetrahedral symmetry and the O2 site in a distorted tetrahedral symmetry.

In the DOS calculations, the muffin-tin radii of Ba, Ti and O are set to 2.4, 1.9 and 1.6 in units of the Bohr radius, respectively. A $10 \times 10 \times 9$ k-point sampling is used in the irreducible Brillouin zone. The total of 900 k-points are sufficient in the present calculations by comparing with the results of the 8000 k-points calculations in the literature [89]. The site-projected DOS are shown in Fig. 4.16. The O1 p DOS is decomposed into PZ and PX+PY components. For the O1 site, the PX and PY components are equal, and they are represented by the PX+PY component together.

As known, the electron beam is converged on the specimen in the STEM image mode. The EELS/STEM spectrum in the image mode is angularly averaged because the convergent beam eliminates the coherence of the electrons [64]. Therefore, the total oxygen DOS should be compared with the experimental spectrum. The comparison between oxygen p DOS and the measured ELNES of the oxygen K edge is shown in Fig. 4.17. The total oxygen p DOS is given by the summation of O1 and O2 p DOS weighted with the corresponding multiplicity of equivalent positions. The interpretation of the fine structures in oxygen p DOS is similar to that of SrTiO_3 . Peaks A1 and A2 are related to the hybridization of the titanium $3d$ orbitals and the oxygen $2p$ orbitals. The intensities of peaks A1 and A2 are slightly smaller than those of SrTiO_3 due to the larger bond length which reduces the Ti-O hybridization. The weak peak A2 is smeared out by the overlapping peak B1. Peaks B1 and B2 are dominated by the Ba-O bonding interactions. The calculated splitting of the peaks B1 and B2 in BaTiO_3 is about 2.0 eV compared to the splitting of about 1.0 eV in SrTiO_3 . Due to the stronger broadening of the peak B1 in BaTiO_3 , this splitting is not discriminable in the ELNES spectrum, in contrast to the well separated peaks B1 and B2 in SrTiO_3 . In comparison

Table 4.3: Unit cell parameters of bulk BaTiO_3 with a space group $P4mm$, taken from Ref. [73]. The lattice parameters are $a=3.994 \text{ \AA}$, $b=4.038 \text{ \AA}$. The muffin-tin radii R_{MT} used in the DOS calculations are given for all different atoms in units of the Bohr radius.

	x	y	z	R_{MT}
Ba	0.0	0.0	0.0	2.4
Ti	0.5	0.5	0.515	1.9
O1	0.5	0.5	-0.024	1.6
O2	0.5	0.0	0.48	1.6

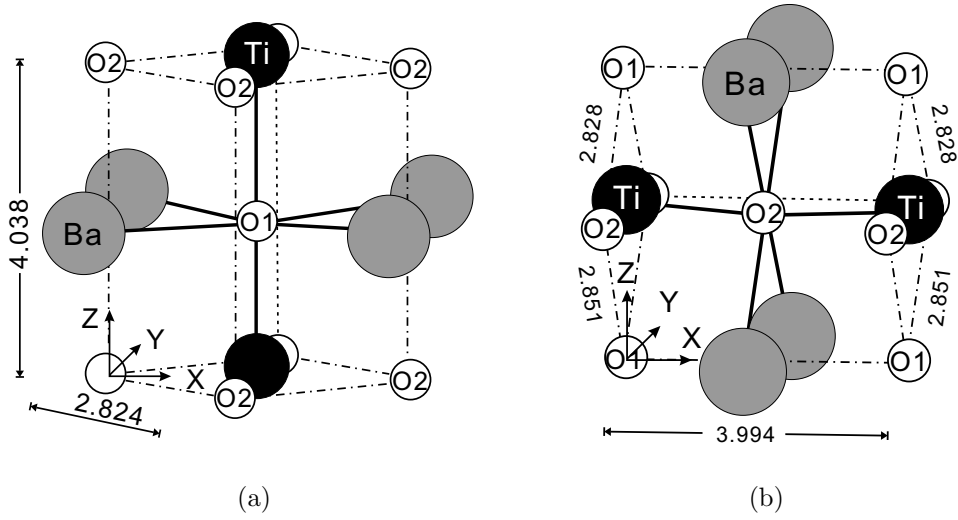


Fig. 4.15: (a) Atomic coordination of O1 site. (b) Atomic coordination of O2 site. The lateral lengths of the oxygen hexahedron are scaled in units of \AA .

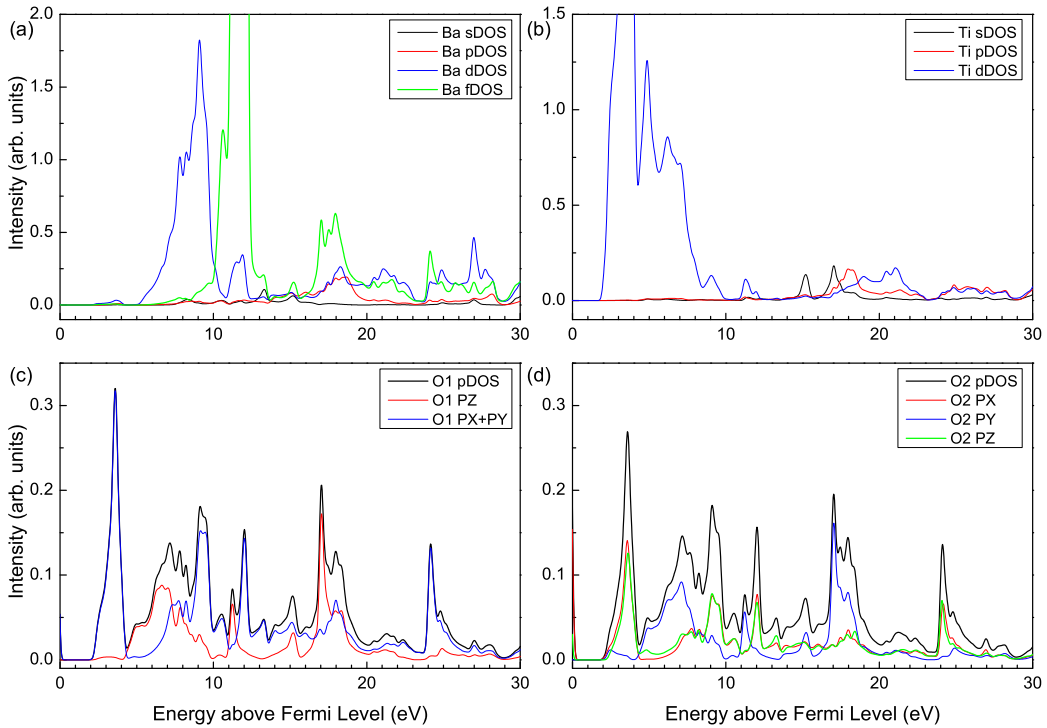


Fig. 4.16: Ground state site-projected density of states of bulk BaTiO_3 . The p DOSs of the O1 and O2 sites at $(1/2, 0, 0.48)$ are decomposed into PX, PY and PZ components. The O2 site at $(0, 1/2, 0.48)$ is equivalent to the O2 site at $(1/2, 0, 0.48)$ except a 90° rotation about the Z-axis.

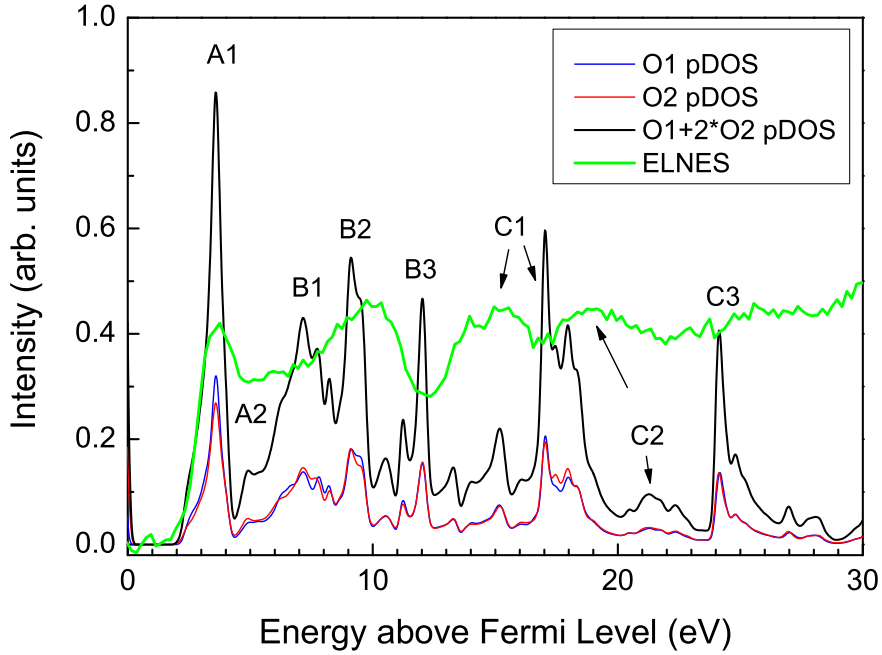


Fig. 4.17: Ground state oxygen p -projected density of states of the bulk BaTiO_3 in comparison with the ELNES of the oxygen K edge.

with SrTiO_3 , the intensity of the peak B2 is a little stronger in BaTiO_3 . This result is well consistent with the experimental finding. The small energy shift of the peaks B1 and B2 is caused by the core-hole effect. Peak B3 is mainly related to the f DOS (f -character density of states) of Ba atoms, which can be seen in Fig. 4.16(a). Since the $1s \rightarrow 4f$ transition is forbidden by the dipole selection rule, peak B3 is not present in the experimental spectrum. The interesting features in the oxygen K edge are peaks C1 and C2. The 3.8 eV-splitting of C1 and C2 is well reproduced. In comparison with the ELNES spectrum, the calculated peaks C1 and C2 are shifted to higher energy by about 2.5 eV, and the intensity of peak C2 is underestimated. The underestimated intensity of the peak C2 might be caused by the neglect of the dipole transition matrix. When the dipole selection rule is applied, the relative intensities of peaks C1 and C2 should have a better consistency with the experiment.

The oxygen p -projected density of states in bulk (P4mm), $\text{Pm}\bar{3}\text{m}$ and layer BaTiO_3 have been compared in this thesis. The lattice parameter ($a=4.009 \text{ \AA}$) of the $\text{Pm}\bar{3}\text{m}$ BaTiO_3 was determined by taking the same unit cell volume as bulk BaTiO_3 . The lattice parameters of the layer BaTiO_3 have been determined by the selected-area diffraction pattern (cf. Table 4.1). The atomic positions in the unit cell of the layer BaTiO_3 have been assumed to be same as those of bulk BaTiO_3 . The comparison is given in Fig. 4.18. One can see that the three spectra are very close except a small energy shift in the high-energy region. In comparison with bulk and the $\text{Pm}\bar{3}\text{m}$ BaTiO_3 , the oxygen p DOS of the layer BaTiO_3 is slightly shifted to higher energy by about 0.2 eV. This shift is caused by the misfit strain which compresses the lattice in the XY plane. However, this slight shift is difficult to recognize in the ELNES spectra due to the spectral broadening at the high-energy tail of the core-loss edge.

The relationship between the peaks C1-C3 and the surrounding oxygen shells can be determined following the similar procedures like for SrTiO_3 . FMS calculations in the shell-by-shell model have been done for O1 and O2 sites, respectively. The calculations have been performed from 3 up to 49 atoms. The 49-atom cluster is divided into six shells. The

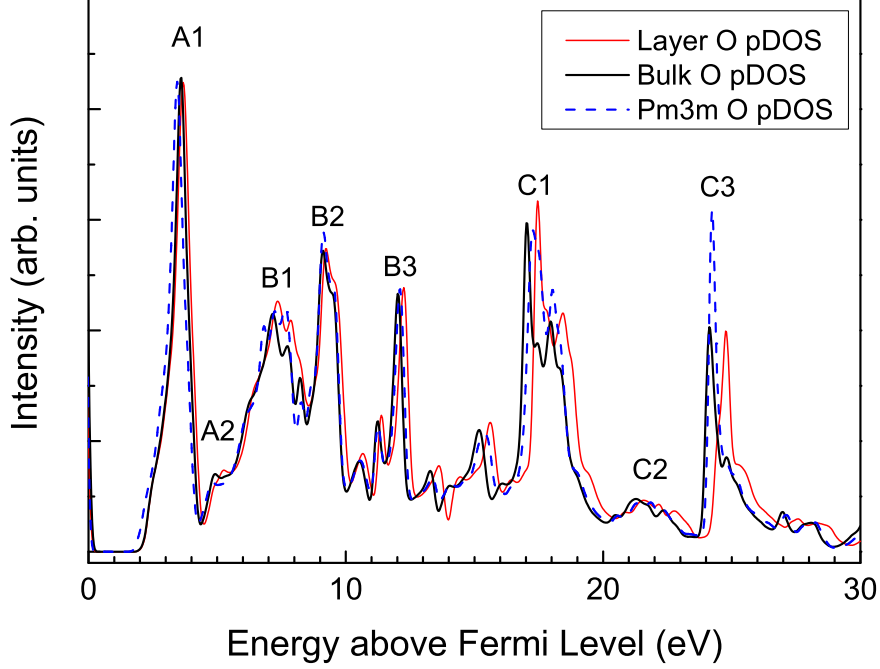


Fig. 4.18: Comparison of oxygen p DOSs in bulk ($P4mm$), $Pm\bar{3}m$ and layer BaTiO_3 . The spectra have been normalized by the intensity of peak A1.

definition of each shell is similar to that in Fig. 4.13, except the different distance to the central atom and a slight distortion of the symmetry. The details are listed in Table 4.4. The results of the FMS calculations are given in Fig. 4.19. The FMS calculation in a 169-atom cluster is given for comparison. Similar to SrTiO_3 , peak C1 can be assigned to the nearest-neighbor oxygen shell, peak C2 is assigned to the second nearest-neighbor oxygen shell and peak C2 is assigned to the third nearest-neighbor oxygen shell. The main difference between the fine structures of the O1 and O2 K edges is that the intensity of the peak A1 of the O1 K edge is higher than that of the O2 edge. This is caused by the shorter Ti-O1 bond length which enhances the pd hybridization.

Table 4.4: The definition of each shell surrounding O1 and O2 sites. The distance is given in units of \AA .

Shell	O1	Distance	O2	Distance
1 st	2 Ti	1.86-2.18	2 Ti	2.00
2 nd	4 Ba	2.83	4 Ba	2.78-2.90
3 rd	8 O2	2.83-2.85	4 O1 + 4 O2	2.82-2.85
4 th	6 O1	4.00-4.04	6 O2	4.00-4.04
5 th	8 Ti + 4 Ba	4.40-4.85	8 Ti + 4 Ba	4.40-4.87
6 th	16 O2	4.89-4.91	8 O1 + 8 O2	4.89-4.93

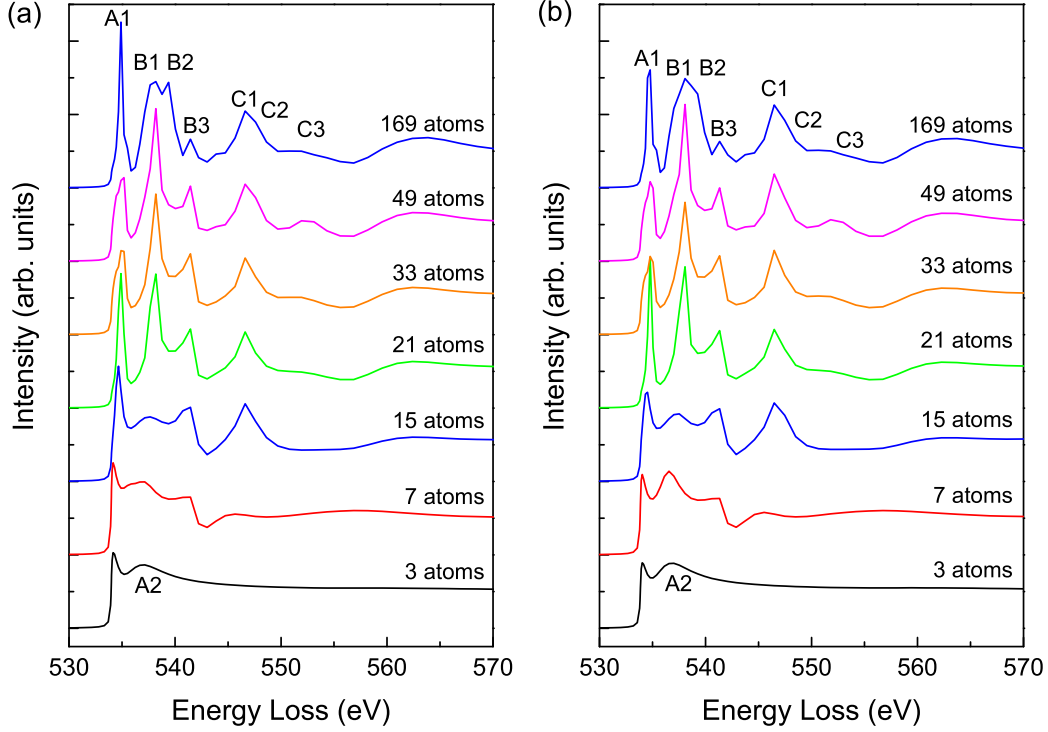


Fig. 4.19: FMS calculations of the (a) O1 and (b) O2 K edges for BaTiO_3 in shell-by-shell model. The shells are defined in Table 4.4.

4.5 Summary

High-energy resolution electron energy-loss spectroscopy has been applied to investigate $\text{BaTiO}_3/\text{SrTiO}_3$ multilayers. The near-edge fine structures are discussed based on experimental results and Ab-Initio full multiple-scattering and band-structure calculations. It reveals that the crystal-field splitting can be used to characterize the misfit strain in BaTiO_3 layers. The crystal-field splitting of the BaTiO_3 thin layer is a little larger than that of bulk BaTiO_3 due to the presence of the misfit strain. This result is confirmed by the lattice parameters of the BaTiO_3 thin layer determined by the selected-area diffraction. This finding proves that the crystal structure of the BaTiO_3 layer is compressed in the growth plane by the misfit strain.

From the increased $[\text{Ti}]/[\text{O}]$ ratio obtained, oxygen vacancies are found to preferably aggregate at the rougher upper interface of BaTiO_3 layers. Oxygen vacancy ordering occurs in the BaTiO_3 thin layer under the influence of the misfit strain. Near the lower interface, the BaTiO_3 layer is revealed to be defect free due to the presence of the misfit strain. It is concluded that the difference of dielectric properties between multilayers and bulk BaTiO_3 is dominated by the aggregation of oxygen vacancies (related to a space charges region) at the rough upper interface.

The near-edge fine structures of the multilayers are discussed based on experimental results and theoretical calculations. According to the full multiple-scattering and band-structure calculations, the fine structures of the oxygen K edge above 12 eV and the satellite structures of the Ti L_{23} edges in SrTiO_3 and BaTiO_3 are partly related to Ti-O and Sr-O or Ba-O interactions and mainly reflecting oxygen-oxygen interactions. The results give a better

understanding of the origin of the fine structures. The theoretically derived results are fairly well consistent with the experimental findings. For the oxygen K edge, the band-structure method has a better accuracy in the energy range of 0-12 eV above the Fermi level while the full multiplet-scattering method is suitable to analyze the oxygen-oxygen interactions in the higher energy range. In the different compounds with a perovskite structure, the fine structures of the oxygen K edge are very similar. The relationship between spectral features of the oxygen K edge and the coordination around the oxygen site is summarized in Table 4.5.

Table 4.5: The relationship between the fine structures of the oxygen K edge and the the surrounding coordination around the oxygen site in perovskite oxides MTiO_3 . M indicates the metal element such as Ba, Sr, Pb, Zr, etc.

Peak	Relates to
A1,A2	The nearest Ti atoms
B1,B2 and B3	The nearest M atoms
C1	The 1 st O shell
C2	The 2 nd O shell
C3	The 3 rd O shell

Chapter 5

HR-EELS Investigation of Y_2O_3 Films on Si (001) Substrate

5.1 Introduction

Interface reactions between deposited Y_2O_3 films and silicon substrates have been investigated by several authors. As suggested by Choi et al. [90], the interfacial SiO_x layer in the as-deposited Y_2O_3/Si sample is caused by the surface oxidization of the silicon substrate at the initial stage of the deposition. The interfacial SiO_x layer can be enhanced by the diffusion of oxygen from the surface in the annealing process. Many efforts to avoid the formation of the interface layer have been made by several methods, such as a lower substrate temperature, a polycrystalline silicon capping layer [15], a pre-nitridation of the silicon substrate, and a pre-deposition of a yttrium-metal-seed layer on the silicon substrate [91]. In addition to the formation of an interfacial SiO_x layer, the formation of yttrium silicates has been reported by several groups [11, 13]. However, its evidence was based on the intermediate brightness of HRTEM images. More experiments by different techniques are necessary to investigate the formation mechanism of the interface layers.

In this work, a high-resolution PEELS spectrometer (Gatan Enfina 1000) installed on a dedicated scanning transmission electron microscope (VG HB 501 UX) is used to investigate the interfacial SiO_x layer and the possible yttrium silicate layer. In contrast to the energy-filtered TEM (EFTEM), the main advantage of the EELS/STEM technique is the much higher signal intensity and the nanoscale probe size which are suitable for the analysis in nanoscale dimensions. The purpose of this experiment is to give a better understanding of the interface reactions.

5.2 Experiments

A 220 nm thick Y_2O_3 film has been deposited on Si (001) substrate by ion beam sputtering [6]. The substrate temperature was kept at 700°C during the deposition on the silicon (001) substrate. The samples investigated are as-deposited without annealing. In order to analyze the chemical composition in the interface region, a commercial $SiO_2(20\text{ nm})/Si$ wafer was prepared into a TEM specimen for acquiring reference spectra. The details of EELS specimen preparation have been given in Chapter 3. For speeding up the time-consuming ion milling process, the ion milling manually started at a higher energy (3.5 keV) and ended at a lower energy (2.0 keV). Single sector mode (specimen was thinned from only one direction or sector) was set to prevent the very thin edge from being sputtered away by the ion beam from the opposite direction. The ion milling was stopped as soon as the specimen was transparent. To minimize the spatial drift caused by the charging effect, an amorphous

carbon layer was deposited on the surface of the specimen by a High Vacuum Turbo Carbon Coater 208/C as well as the small hole was shielded from carbon coating by a thin wire. A small objective aperture with a radius of $25 \mu\text{m}$ was selected to limit the convergence semiangle to ca. 6.5 mrad . It should be noted that the convergence angle is very critical to acquire the spectra from the interface region as discussed before. The tail of electron beam with a larger convergence angle can easily excite the atoms several nanometers away from the interesting region.

5.3 Results and Discussions

Prior to the investigation of Y_2O_3 films, the Si L_{23} edges and the oxygen K edge are measured from a SiO_2 thin film (20 nm) deposited on Si(001) substrate. These spectra can be used as fingerprints of amorphous SiO_2 . A line scan across the SiO_2/Si interface was performed with a step width of 0.5 nm . Fig. 5.1 shows the STEM bright-field image and the raster image of the line scan across the interface. An abrupt interface between the oxide layer and the substrate can be seen from both images. The acquired Si L_{23} and oxygen K edges are given in Fig. 5.2. The interface spectrum of the Si L_{23} edges is significantly different from the spectra acquired from the silicon substrate and the SiO_2 film. The spectrum of the Si L_{23} edges becomes identical to the silicon or SiO_2 spectrum in the previous or next step. It means that the spatial resolution of the used EELS/STEM instruments under these conditions is better than 0.5 nm .

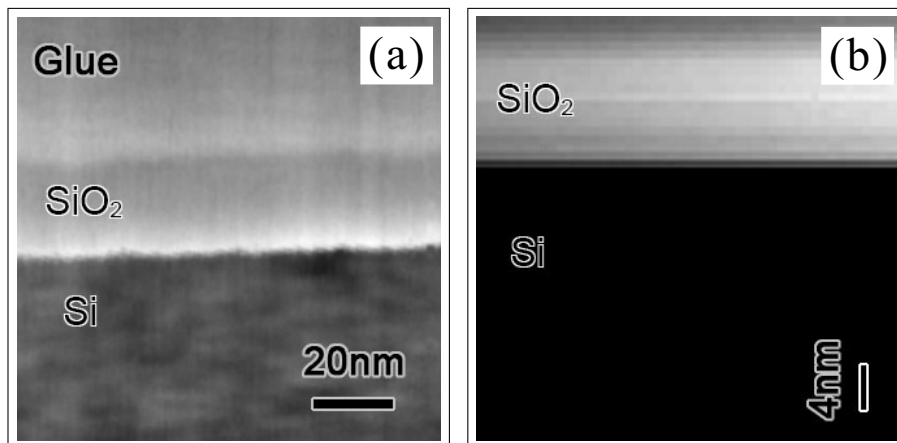


Fig. 5.1: (a) STEM bright-field image of $SiO_2(20 \text{ nm})/Si$ structures. (b) Raster image of a line scan across the SiO_2/Si interface with a scanning step of 0.5 nm .

The bright-field STEM image of the Y_2O_3/Si structure is shown in Fig. 5.3(a). An interface layer between the Y_2O_3 film and the silicon substrate is well distinguished. The selected area diffraction pattern taken from the interface region (including both Y_2O_3 film and Si substrate) is shown in Fig. 5.3(b). The indexing of diffraction pattern is given in the left-bottom and right-top insets for the silicon substrate and Y_2O_3 film, respectively. One can clearly recognize the $[111]$ growth direction of Y_2O_3 thin film. The orientation relationships between the Y_2O_3 film and the silicon (001) substrate have been reported several times by different authors [12, 90, 13, 6, 92, 91]. But their results are not consistent due to different experimental conditions. Several authors reported the growth of Y_2O_3 films along the $[111]$ direction. Other groups obtained a $[110]$ growth direction. The $[110]$ or/and $[111]$ growth directions were almost always found. According to the orientation

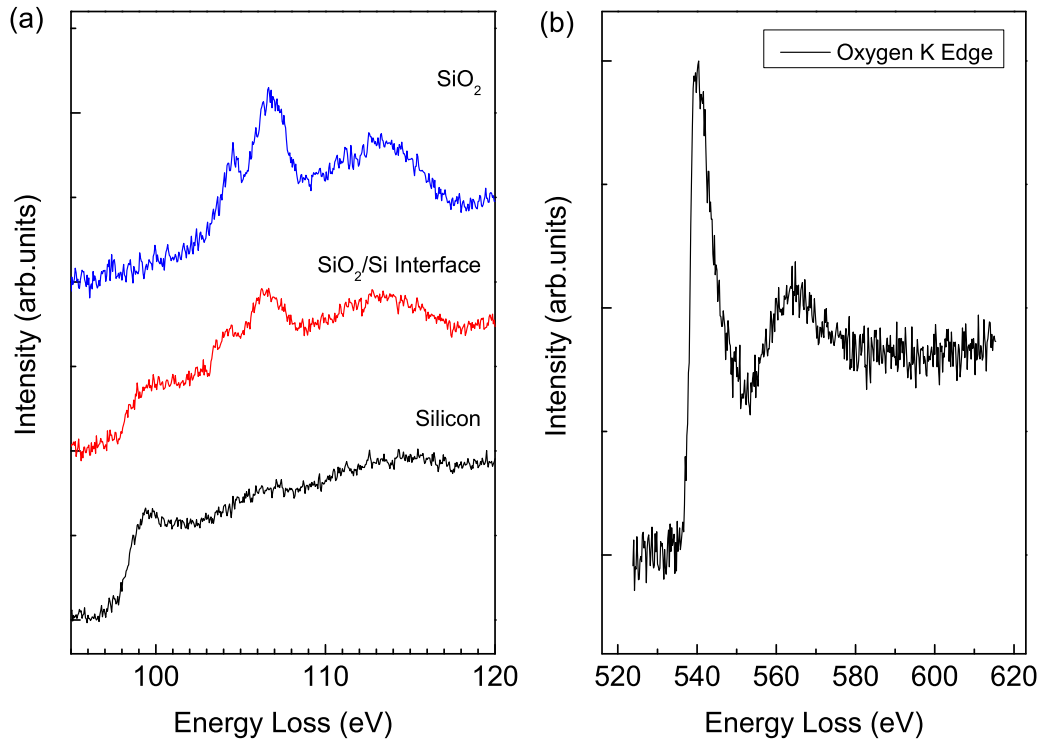


Fig. 5.2: (a) Si L₂₃ edges acquired from the silicon substrate, the SiO₂/Si interface, and the amorphous SiO₂ thin film. (b) Oxygen K edge of the amorphous SiO₂ thin film.

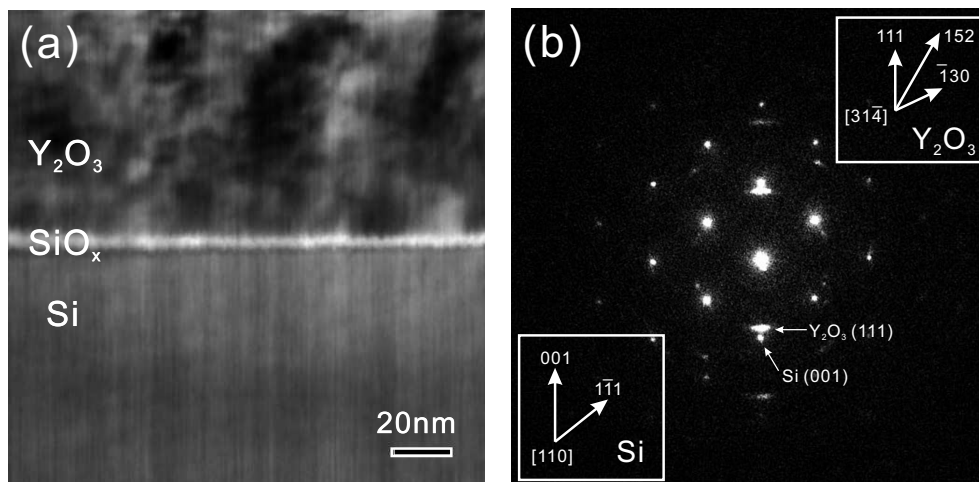


Fig. 5.3: (a) Cross-section STEM bright-field image of a 220 nm thick Y₂O₃ film deposited on Si(001) substrate. (b) Selected area diffraction pattern taken from the interface region containing the Y₂O₃ film, the interfacial SiO_x layer and the silicon substrate. The indices of the diffraction pattern are given in the insets.

relationships reported, the following description might be concluded: the $Y_2O_3(110)/Si(001)$ relationship is favorable without the presence of the interfacial SiO_x layer. In contrast, the $Y_2O_3(111)/Si(001)$ relationship is favorable with the formation of the interface layer. The reason why the (110) and (111) planes grow much faster than the other planes might be related to the surface free energy. The surface free energies of the (111) and (110) planes should be much lower than those of the other planes. Additionally, yttrium and oxygen atoms lay in the (110) and (111) planes with the right stoichiometry of 2:3, which makes the terminated surface charge-neutral. The neutral terminated planes reduce the surface free energy so that the layer-by-layer epitaxial growth model is energetic favorable in the deposition of Y_2O_3 film. Otherwise, the oxygen partial pressure is also an important factor for the crystallization of Y_2O_3 films. The ordering or aggregation of oxygen defects might influence the growth directions. As known, due to the aggregation of oxygen defects, a columnar structure of Y_2O_3 film is enhanced with increasing oxygen partial pressure [91].

The high-resolution TEM (HRTEM) image acquired from the interface layer is shown in Fig. 5.4. The [111] growth direction of the Y_2O_3 film can be easily recognized. In fact, there is a small angle between the Y_2O_3 (111) and Si (001) planes. This angle is slightly different for different Y_2O_3 grains. The grain boundaries can be seen in the right-top of the HRTEM image. The interfacial SiO_x layer is amorphous and bright with a thickness of about 3 nm. Additionally, there is a 2 nm thick layer with a intermediate brightness between the interfacial SiO_x layer and the deposited Y_2O_3 film. This finding is similar to the results of Kang et al. [13]. For simplicity, this layer will be called “intermediate layer” in the following discussion.

5.3.1 Si L_{23} Edges

The Si L_{23} edges are acquired at different positions across the Y_2O_3/Si interface by a line scan. The scanning step is about 0.5 nm. The exposure time per step is set to 1.0 s. The

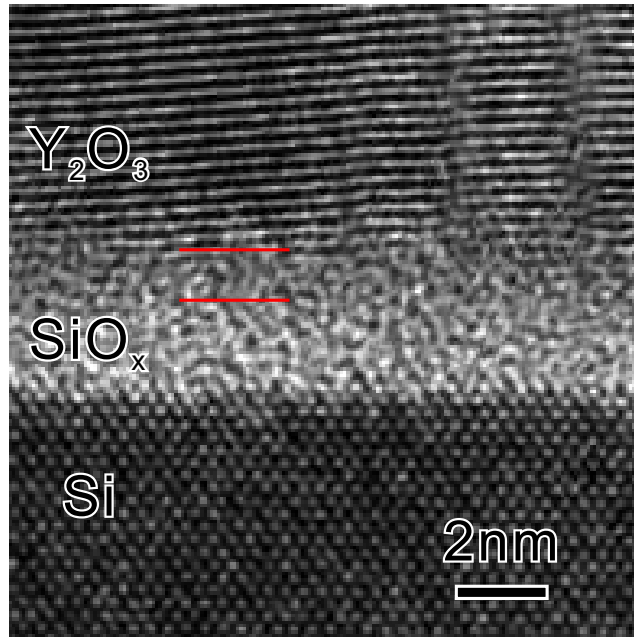


Fig. 5.4: HRTEM image of the $Y_2O_3/Si(001)$ structure. The red double lines indicate the intermediate layer between the interfacial SiO_x layer and the Y_2O_3 film.

energy dispersion is set to 0.05 eV/channel in order to acquire fine structures in a high energy resolution. The raster image of the line scan is shown in Fig. 5.5(a). The spectra are acquired from the silicon substrate to the Y_2O_3 film. The spectra corresponding to the marked positions in Fig. 5.5(a) are shown in Fig. 5.5(b). The reference spectrum of amorphous SiO_2 , taken from a 20 nm thick SiO_2 thin film deposited on Si(001) substrate, is given as a fingerprint spectrum of amorphous SiO_2 . The strong peak A1 in spectrum 1 (taken from the silicon substrate) indicates the Si-Si bonding, which can be used to monitor the presence of pure silicon in the line scan. Peaks A1 and A2 are present in the spectra taken from the silicon substrate. The energetic separation of peaks A1 and A2 is about 1.8 eV. The interpretation of peaks A1 and A2 is difficult from band-structure calculations because the formation of sp^3 hybridization leads to the dipole-allowed $p \rightarrow p$ transitions [93]. In band-structure calculations (not shown here), peaks A1 and A2 occur in s , p , and d DOSs. In the molecular orbital point of view, peaks A1 and A2 can be assigned to the electron transitions from the $2p$ orbitals to the unoccupied e_g and t_{2g} orbitals in the tetrahedral coordination, respectively.

As indicated by peak A1, the spectra taken from positions 3–5 (between the SiO_x/Si interface and the center of the SiO_x layer) possess a small contribution of silicon. In the region from the center of the interface layer to the Y_2O_3 film, there is no detectable contribution from silicon, as seen in the spectra 6–11. Note that the intensity of the small peak A1 in spectra 4–5 does not depend on the probe position. So the small portion of silicon is not caused by the tail of electron beam. It might be the residua of the chemical reaction between the silicon substrate and diffused oxygen atoms, or caused by silicon diffusion from the silicon substrate.

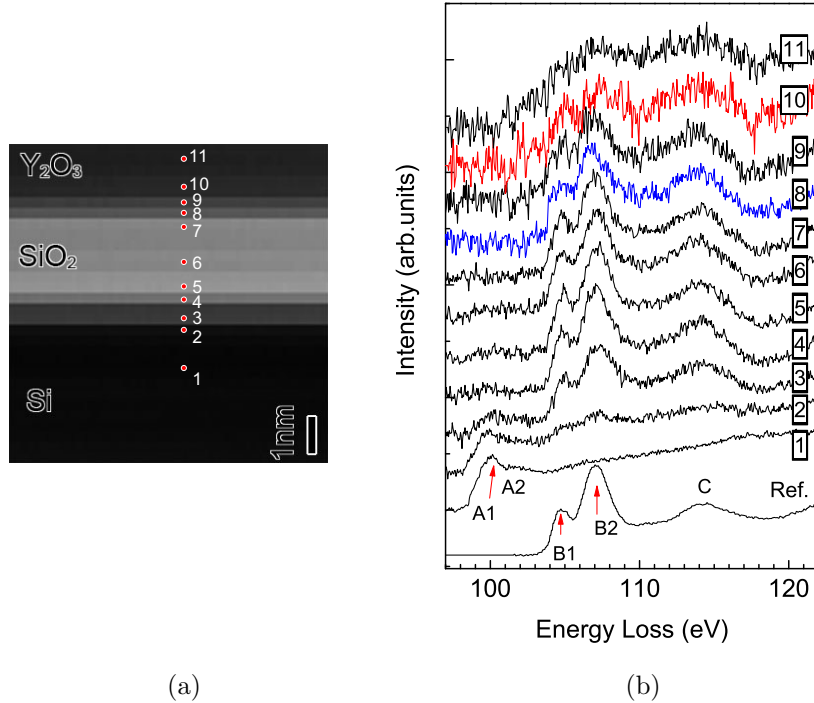


Fig. 5.5: (a) Raster image of the line scan across the interface region. (b) Si L_{23} edges taken from the different positions labeled 1-11 in the raster image (a). The reference spectrum of amorphous SiO_2 is taken from a 20 nm thick amorphous SiO_2 layer deposited on a silicon substrate.

In the interfacial SiO_x layer, features B1, B2, and C in spectra 4–7 are fairly well consistent with those in the reference spectrum of amorphous SiO_2 . Therefore, the chemical composition of the interfacial SiO_x layer can be attributed to amorphous SiO_2 . The magnified spectra from Fig. 5.5(b) are shown in Fig. 5.6. A small peak labeled C' can be found in the interfacial SiO_2 layer with respect to the reference spectrum. This peak can be clearly found in the region around the center of the interfacial SiO_x layer. According to the FMS calculations of α - SiO_2 and β - SiO_2 , the slight difference is caused by the small distortion of the tetrahedral coordination of oxygen around silicon atoms. The FMS calculations of α - SiO_2 and β - SiO_2 will be discussed later. The reacting oxygen atoms are partly from (1) the initial stage of deposition, (2) the interstitially trapped oxygen atoms during the deposition, and (3) the oxygen diffusion from the Y_2O_3 surface. As known, a SiO_x layer can be formed after annealing even in high vacuum [13]. A polycrystalline silicon capping layer deposited on the Y_2O_3 film can reduce the thickness of the interface layer [15]. These findings reveal that the origin of oxygen participating in the interface reaction is not a single one.

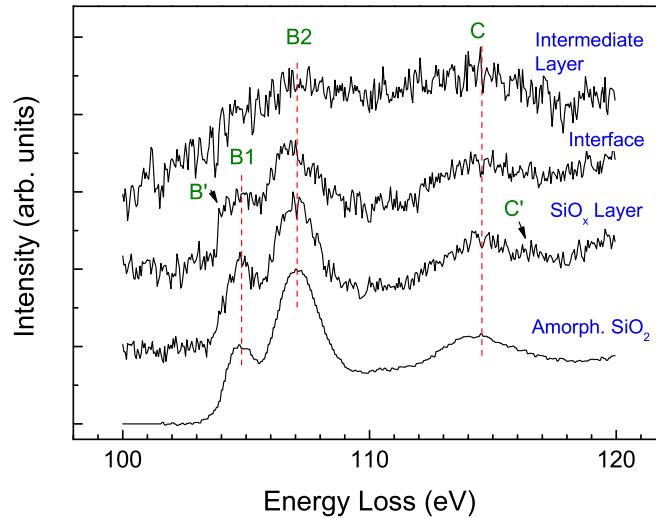


Fig. 5.6: Magnified comparison between the spectra taken from the interfacial SiO_2 layer (spectrum No.7 in Fig. 5.5b), the interface between the interfacial SiO_2 layer and the intermediate layer (spectrum No. 8), the intermediate layer (spectrum No. 11), and the reference spectrum taken from an amorphous SiO_2 layer.

In comparison with the interfacial SiO_2 spectra 4–7 in Fig. 5.5(b), significant changes can be found in the spectra 8–9 which are acquired from the interface between the interfacial SiO_2 layer and the intermediate layer. The magnified spectrum 8 is shown in Fig. 5.6. Firstly, the peak B2 of the interface spectrum is shifted to lower energy by about 0.4 eV. Since a cation with a lower valency generally has a lower energy threshold of core-loss edge [51, 94, 95], this energy shift might correspond to the aggregation of oxygen vacancies at the interface between the interfacial SiO_2 layer and the intermediate layer. The presence of oxygen vacancies causes the valency of silicon ion less than 4+. Secondly, the separation of peaks B1 and B2 is reduced to 2.0 eV with respect to the value of 2.2 eV in the SiO_2 layer. The separation of peaks B1 and B2 is caused by the oxygen coordination in a tetrahedral symmetry. Peaks B1 and B2 correspond to electron excitations from the $2p$ orbitals to the unoccupied e_g and t_{2g} orbitals, respectively. Similar to the ligand-field model for transition-metal compounds [51], the reduced separation should result from the elongated Si-O bond

length or the expanded volume of the oxygen tetrahedron. Thirdly, peak B1 is split into two peaks. The lower-energy peak is labeled B' in Fig. 5.6. The higher-energy peak uses the old label, B1. The splitting between peaks B' and B1 is about 0.5 eV. This splitting is similar to the splitting found in α -SiO₂, which has been attributed to spin-orbit splitting [96]. In the molecular orbital point of view, the separation of peaks B' and B1 originates from the distortion of oxygen tetrahedra.

The origins of peaks B' and C' can be confirmed by FMS calculations of α -SiO₂ and β -SiO₂. Since the Si-O bonding is ion-like, the Si L₂₃ edges are mainly sensitive to the four neighbor oxygen atoms in a short-distance range. The long-distance environment has little influence on the Si L₂₃ edges in the low-energy region. This result can be confirmed by FMS calculations of α -SiO₂ and β -SiO₂ in a small cluster containing only 5 atoms. The unit cell parameters of α -SiO₂ and β -SiO₂ are taken from the reported data by Angel et al. [97] and Liu et al. [98], respectively. Fig. 5.7(a) shows the coordination of silicon atoms in α -SiO₂. The silicon coordination of β -SiO₂ is similar to that of α -SiO₂, except small differences in bond lengths and bond angles. In α -SiO₂, Si is tetrahedrally bonded to four oxygen atoms with two shorter bonds (1.605 Å) and two longer bonds (1.614 Å). In β -SiO₂, the four bond lengths are equal to 1.606 Å, and the distortion of the tetrahedron is much smaller than that of α -SiO₂. The oxygen tetrahedron in β -SiO₂ can be roughly taken as a regular tetrahedron. In fact, the Si-O bond is very strong. Its bond length varies only within a small range in the nine silica polymorphs [99]. That is the basis of the so-called "rigid unit mode" (RUM) theory in the literature [100]. FMS calculations containing 5, 9 and 105 atoms are given in Fig. 5.7(b). The main peaks B2, C, and D are well reproduced by the 5-atom cluster in either α -SiO₂ or β -SiO₂. The peak positions are in fairly good agreement with the amorphous SiO₂ spectrum. A small shift to lower energy can be found in the spectrum of β -SiO₂ with respect to α -SiO₂, which is caused by the expanded volume of the oxygen tetrahedron, which leads to a weaker ligand field. In the 105-atom cluster, the

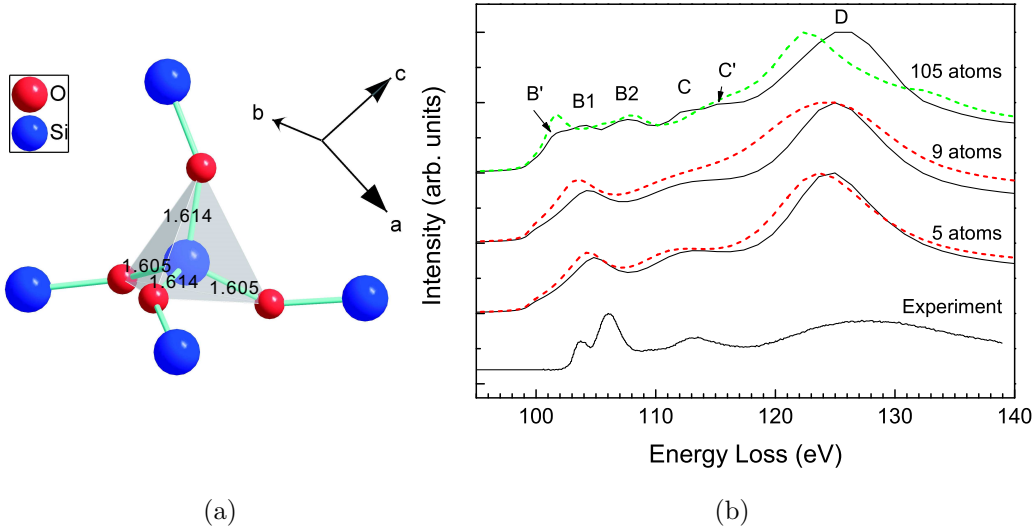
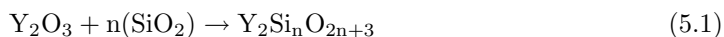


Fig. 5.7: (a) Small cluster containing 9 atoms for the FMS simulations in α -SiO₂. (b) Si L₂₃ edges calculated by the FMS method in shell-by-shell model in comparison with the experimental spectrum taken from amorphous SiO₂. The solid lines indicate the FMS calculations in α -SiO₂, and the dotted lines indicate the FMS calculations in β -SiO₂. All of the calculated spectra have been broadened by 0.4 eV.

features B' and C' are reproduced in α -SiO₂ but not in β -SiO₂. This result means that the features B' and C' originate from the distortion of oxygen tetrahedra. Features B1, B2, C, and D can be used as a fingerprint of silicon in an oxygen tetrahedron.

In Fig. 5.6, the features in the spectrum acquired from the intermediate layer are much broader than those of the other spectra. This spectrum is well consistent with the electron energy-loss spectrum recently reported by Niu et al. [14]. Note that there is no detectable contribution from silicon in the positions 6–11 (cf. Fig. 5.5b) as indicated by the peak A1. It means that yttrium silicates formed at the Y₂O₃/SiO₂ interface is not contributed from the diffusion of silicon from the silicon substrate as suggested by Stemmer et al.[15]. In other words, there should be a small peak A1 in the spectra 6–8 if yttrium silicates originates from the diffusion of silicon from the substrate. In this work, the formation of yttrium silicates is attributed to direct chemical reactions between the deposited Y₂O₃ film and the interfacial SiO₂ layer. The direct chemical reaction between Y₂O₃ and SiO₂ is known to be exothermic and entropically favorable [101]. In fact, the crystal structure of Y₂Si_nO_{2n+3} can be synthesized at 450°C, which is much lower than the deposition temperature of 700 °C [102]. In the intermediate layer yttrium silicates should result from the following chemical reaction between the Y₂O₃ film and the interfacial SiO₂ layer [103]:



during the deposition. For $n = 1$, the yttrium silicate is Y₂SiO₅, and is Y₂Si₂O₇ for $n = 2$. However, to the authors' knowledge, there is still no reported EELS or XAS investigation on the single crystal of the yttrium silicates in the literature. The experimental fingerprints of the yttrium silicates are expected to be done in the future investigations. In this work, the Ab-Initio full multiple-scattering calculations will be performed later to confirm the formation of yttrium silicates.

5.3.2 Y M₄₅ Edges

The Y M₄₅ edges have been acquired simultaneously with the Si L edges across the interfacial SiO₂ layer, as shown in Fig. 5.8. The exposure time per step is set to 1.0 s. The energy dispersion has been set to 0.2 eV/channel, so that the Y M₄₅ and Si L₂₃ edges can be acquired simultaneously. The Si L₁ edge of SiO₂ is located at about 152 eV, which overlaps with the first peak of the Y M₄₅ edges. The features of the Y M₄₅ edges, labeled A-F, are complicated due to the $3d \rightarrow 4f$ transitions. Peak positions of features A-F are about 158.5, 160.5, 162, 165, 171 and 186.5 eV, respectively. The interpretation of these fine structures based on Ab-Initio calculations will be given later.

As shown in Fig. 5.8, the intensity of peak F is very strong, which can be used to monitor the presence of yttrium. One can see that yttrium does not exist in spectra 1–7. This finding confirms that the chemical composition of the interfacial SiO_x layer is pure SiO₂ as discussed in the Si L₂₃ edges. In this work, the interfacial SiO_x layer has been assigned to the native SiO₂ formed at the initial stage of deposition. The presence of yttrium can be found in spectra 8-11 which are acquired from the intermediate layer. As discussed before, the Si L₂₃ edges can also be detectable in this intermediate layer. This finding confirms the formation of yttrium silicates in the intermediate layer.

5.3.3 O K Edge

The oxygen K edges are acquired across the interfacial SiO_x layer by the line scan method with a step of about 0.6 nm. The exposure time is set to 5 s per step in order to acquire the sufficient intensity of signals. The spectra acquired from the interfacial SiO_x layer, the intermediate layer and the deposited Y₂O₃ film are shown in Fig. 5.9. The reference spectrum taken from a 20 nm thick amorphous SiO₂ thin film is given as a fingerprint. The main features are labeled A-E in the spectrum acquired from the Y₂O₃ film. One can see

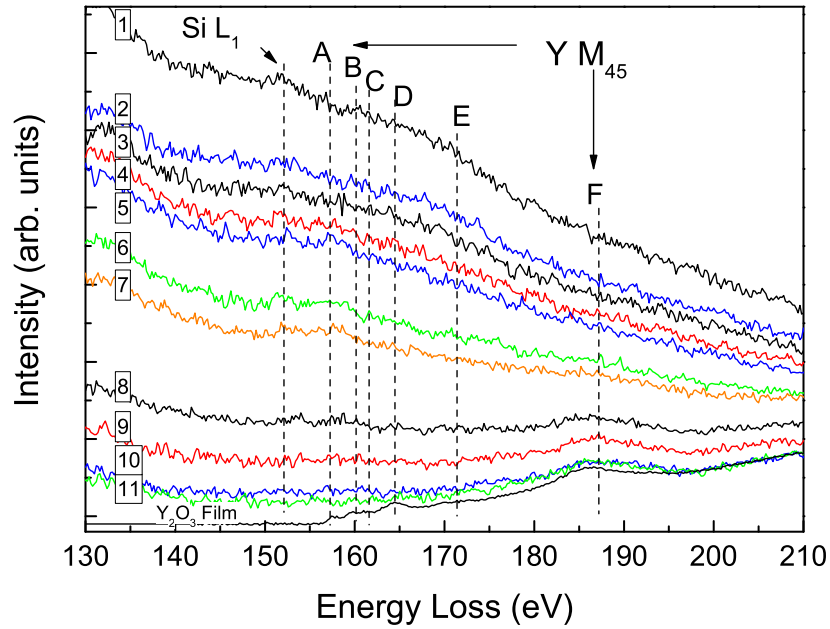


Fig. 5.8: $Y M_{45}$ edges taken from different positions labeled 1-11, corresponding to the same labels in Fig. 5.5(a). The features of the $Y M_{45}$ edges are labeled A-F.

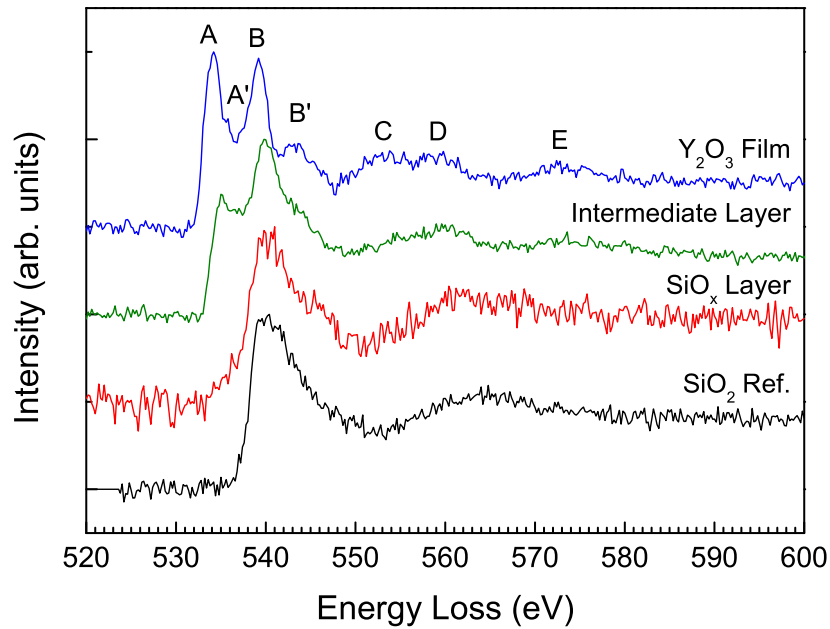


Fig. 5.9: Oxygen K edges acquired from the interfacial SiO_x layer, the intermediate layer, and the Y_2O_3 thin film. The reference spectrum was acquired from a 20 nm thick amorphous SiO_2 thin film deposited on $Si(001)$ substrate.

that the spectrum of the interfacial SiO_2 layer is almost ideally identical to the reference spectrum of amorphous SiO_2 . It confirms that the interfacial SiO_x layer is pure SiO_2 . This finding is consistent with the results of the Si L_{23} and Y M_{45} edges.

In Fig. 5.9, the oxygen K edge taken from the deposited Y_2O_3 film is strong and sharp. An increased peak A was firstly reported by Jollet et al. when they compared the X-ray absorption structures of the oxygen K edge between stoichiometric and non-stoichiometric Y_2O_3 [104]. In their work, the stoichiometric Y_2O_3 sample was heated up to $1700^\circ C$. Some of the oxygen atoms were removed from the lattice that led to a Y_2O_3 sample containing oxygen vacancies. It was found that the intensity of the peak A significantly increased in the non-stoichiometric sample. This increased peak has been interpreted by the effect of the oxygen vacancies according to theoretical calculations. The calculations of local density of states revealed that the introduction of oxygen vacancies leads to a increased peak A because of the disturbance of the octahedral oxygen coordination of yttrium atoms [105]. Molecular dynamics simulation based on the pairwise potential shows that the introduction of oxygen vacancies reduces the Y-O bond length due to the decrease of steric repulsion between the oxygen atoms [106].

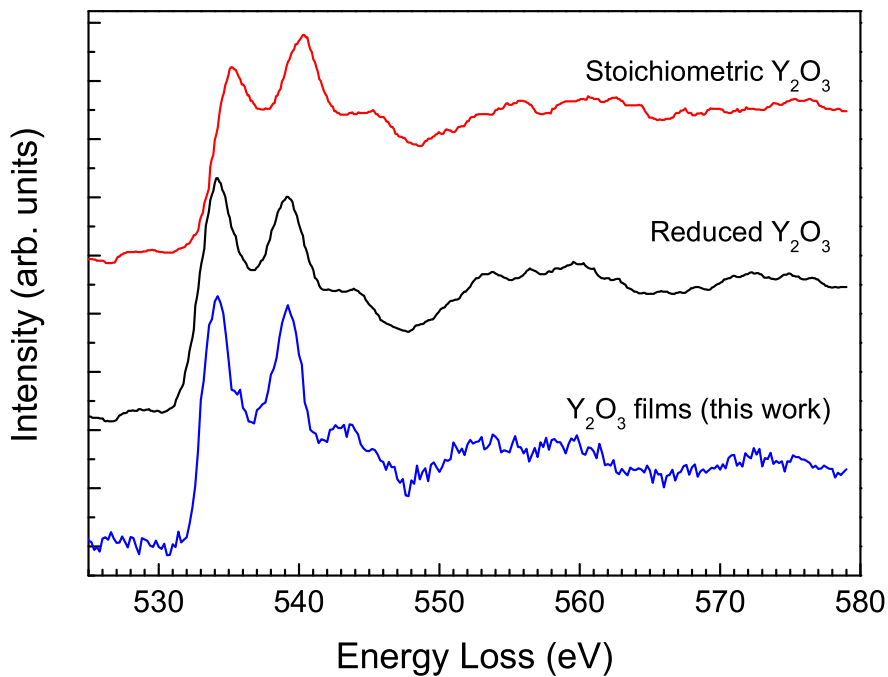


Fig. 5.10: Oxygen K edge of the deposited Y_2O_3 film in comparison with those of stoichiometric and reduced bulk Y_2O_3 redrawn from Ref. [16].

EELS investigations of the reduced Y_2O_3 have been given by Travlos et al. recently [16]. Similar to XAS results, a increased peak A was found in the reduced Y_2O_3 with respect to stoichiometric Y_2O_3 . The electron energy-loss spectra of stoichiometric and reduced Y_2O_3 have been redrawn from Ref. [16] in Fig. 5.10. They are used as reference spectra in this work. It can be seen that the oxygen K edge taken from the deposited Y_2O_3 film is fairly similar to that of the reduced Y_2O_3 . Therefore, it can be concluded that the deposited Y_2O_3 film in this work is oxygen deficient. The spectral discrepancy between this work and Ref. [16] at the high energy region is mainly caused by the removal of the background. It should be noted that the density of oxygen vacancies in the Y_2O_3 film might be very

high. In Ref. [104], 10% of the oxygen atoms have been removed. It means that five oxygen atoms were averagely removed from one unit cell of Y_2O_3 . Oxygen vacancies can order into a superstructure to create a nonstoichiometric region which is surrounded by the stoichiometric regions [16]. However, the acquired oxygen K edge of the as-deposited Y_2O_3 film used in this work is always identical to that of the reduced Y_2O_3 . This result might be interpreted by the aggregation of oxygen vacancies around the electron beam illuminated region. Oxygen vacancies might be metastable and easily moved in the as-deposited Y_2O_3 film under the influence of the electron beam.

In the spectrum taken from the intermediate layer (cf. Fig. 5.9), the intensity of peak A is significantly decreased with respect to the stoichiometric or reduced Y_2O_3 . The intensities of peaks B' and C are also significantly decreased in the intermediate layer. It is believed that this spectrum corresponds to the oxygen K edge of yttrium silicates. The O K edge of yttrium silicates will be calculated later by the FMS method.

5.4 Electron Beam Induced Chemical Reactions

Electron beam induced chemical reactions between the Y_2O_3 film and the interfacial SiO_2 layer have been found when the beam current was increased. The intention of increasing the beam current is to enhance the signal-to-noise ratio of the oxygen K edge. For this purpose, a larger objective aperture with a radius of $50 \mu m$ has been selected, and the field emission extraction voltage is also increased. Under these conditions, the beam current illuminated on the specimen increases about one order of magnitude with respect to the previous conditions. The focused electron beam is posited at the Y_2O_3 film near the interfacial SiO_2 layer. The bright-field images before and after the beam irradiation are shown in Fig. 5.11(a) and (b). The first position has been illuminated for 5 s, and the second one for 30 s. One can see that the interfacial SiO_2 layer becomes darker, and bright regions around the beam positions are formed on the Y_2O_3 side after the beam irradiation.

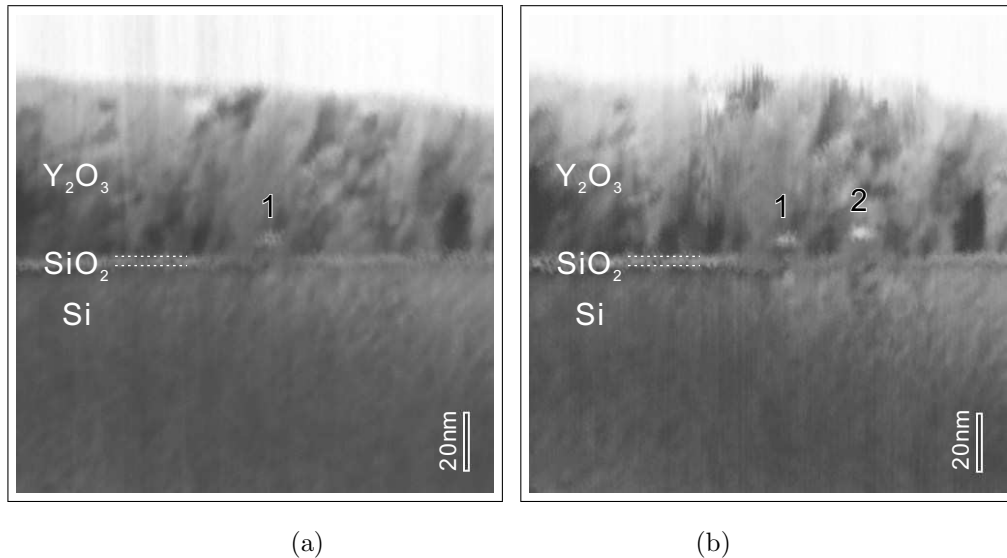


Fig. 5.11: Bright-field STEM image (a) before and (b) after the beam radiation at the position 2. The dashed double lines indicate the interfacial SiO_2 layer.

In Fig. 5.12, a HRTEM image has been acquired at the bright regions after the beam irradiation. One can see that the interface layer is reconstructed under the influence of electron beam. The reconstructed layer has the same periodic phase contrast as the silicon

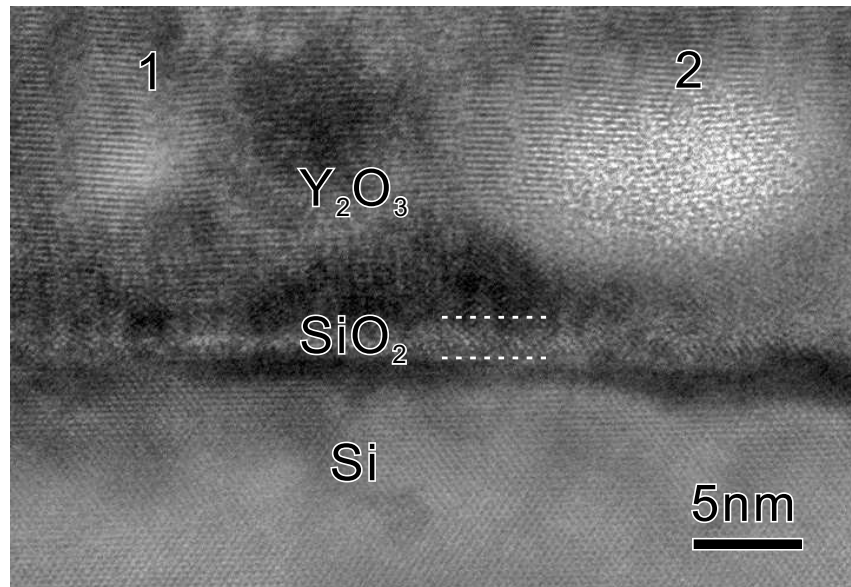


Fig. 5.12: Bright-field HRTEM image acquired from the bright regions after the beam irradiation. The dashed double lines indicate the reconstructed interface layer.

substrate. This finding is well consistent with the results of Paumier et al. [107]. The Si L_{23} and O K edges acquired from the interface layer before and after the beam irradiation are shown in Fig. 5.13. In the Si L_{23} edges, the presence of peak A1 after the beam irradiation indicates the existence of silicon in the reconstructed interface layer. This portion of silicon might diffuse from the substrate under the influence of the electron beam. The variation of the O K edge before and after the beam irradiation is very small.

As shown in Fig. 5.12, the bright regions become amorphous after the beam irradiation, and the Y_2O_3 (111) planes slightly bend to the interface layer. In order to analyze the chemical composition, the Si L_{23} and O K edges acquired from the bright region 2 are shown in Fig. 5.14. One can see that the Si L_{23} and O K edges of the bright region are very similar

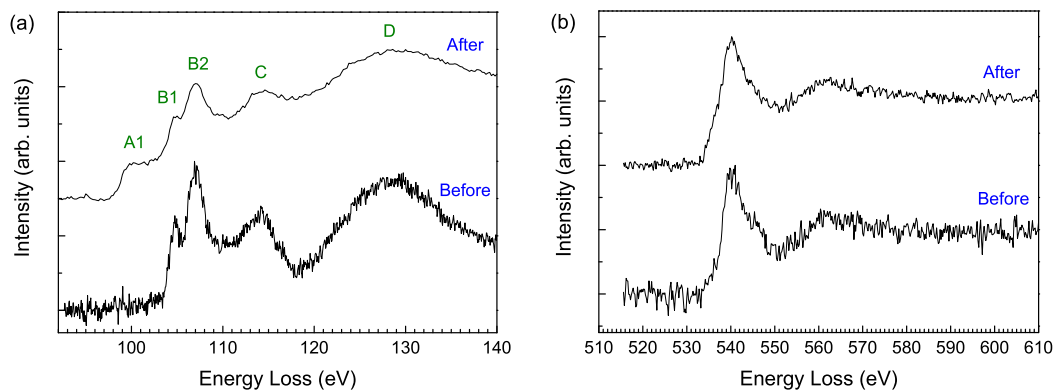


Fig. 5.13: (a) Si L_{23} edges, and (b) O K edge acquired from the interface layer before and after the beam irradiation.

to those of the intermediate layer between the deposited Y_2O_3 film and the interfacial SiO_2 layer. Therefore, yttrium silicates are formed in the bright regions. In fact, the O K edge of the bright region becomes well consistent with that of the SiO_2 after a long-term irradiation, and the chemical composition of the bright region becomes SiO_2 . These findings reveal the diffusion of SiO_2 from the interface layer into the Y_2O_3 film under the influence of the electron beam. One possible explanation of this electron-beam-induced reaction is the aggregation of high-density oxygen vacancies around the electron beam illuminated region, which makes the rigid $[SiO_4]^{4-}$ tetrahedra diffuse into the Y_2O_3 film. This chemical reaction can also be represented by the formula 5.1. As discussed above, the presence of high-density oxygen vacancies has been revealed by comparing the oxygen K edge spectra of the Y_2O_3 film with the reference spectra of the reduced and stoichiometric Y_2O_3 in Ref. [16]. The aggregation of oxygen vacancies might be related to the surface charging in the insulating specimen.

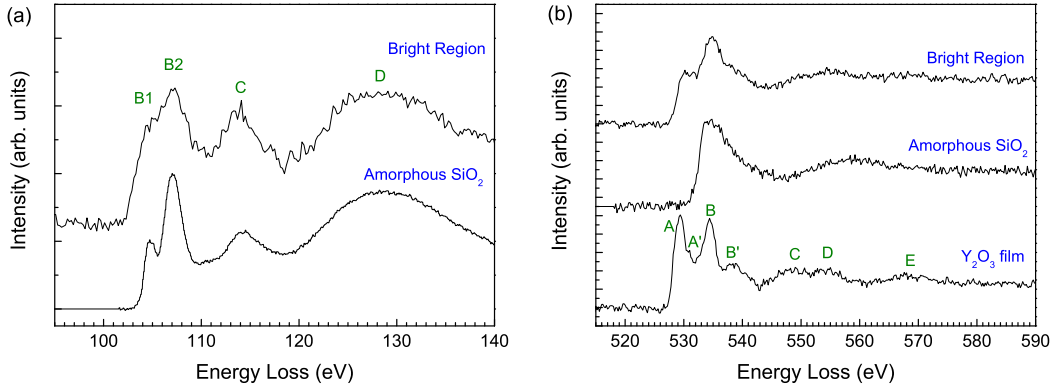


Fig. 5.14: (a) Si L_{23} edges, and (b) O K edge acquired from the bright region 2 (cf. Fig. 5.12 after the beam irradiation).

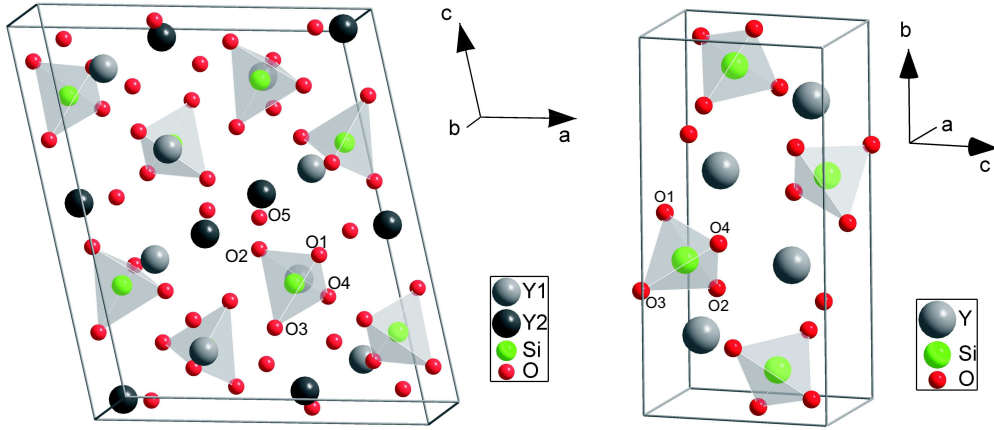
5.5 FMS Calculations of Yttrium Silicates

In order to confirm the formation of yttrium silicates in the intermediate layer, the Si L_{23} and O K edges of yttrium silicates are calculated by the FMS method. The interfacial yttrium silicates might be a mixture of $Y_2Si_nO_{2n+3}$ with different n . There are two well-established yttrium silicates at the Y_2O_3/Si interface, Y_2SiO_5 (Y-oxyorthosilicate) and $Y_2Si_2O_7$ (Y-pyrosilicate) [108, 109]. Theoretical investigations of yttrium silicates are rarely reported in the literature due to scarcely published crystal data of yttrium silicates and the computational bottleneck for such complicated systems. Although the electric structures of Y_2SiO_5 and $Y_2Si_2O_7$ have been recently calculated by the OLCAO (orthogonalized linear combinations of atomic orbitals) method [109], the partial density of states are not given, so it can not be compared with the EELS experiments. The crystal data of Y_2SiO_5 and $Y_2Si_2O_7$ are taken from Ref. [110] and Ref. [102], respectively. The lattice parameters are summarized in Table 5.1. The unit cell structures of this two yttrium silicates are sketched in Fig. 5.15.

The space group of Y_2SiO_5 is $(I 2/a)$. One unit cell contains 64 atoms in total. There are 8 inequivalent positions in a unit cell: two yttrium sites labeled Y1 and Y2, one silicon site and five oxygen sites labeled O1-O5. The Y1 site bonds to six oxygen atoms with the bond lengths ranging from 2.231 Å to 2.321 Å. The Y2 site bonds to seven oxygen atoms with the bond lengths ranging from 2.152 Å to 2.594 Å. The Si site tetrahedrally bonds to four oxygen atom (O1-O4) with the bond lengths of 1.623 Å, 1.629 Å, 1.633 Å, and 1.655 Å.

Table 5.1: Lattice parameters of Y_2SiO_5 and $Y_2Si_2O_7$ taken from Ref. [110] and Ref. [102], respectively.

	Y_2SiO_5	$Y_2Si_2O_7$
Space group	I 2/a	P 2 ₁ /c
a (Å)	10.41	4.694
b (Å)	6.721	10.856
c (Å)	12.490	5.588
β'	102.65°	96.01°


 Fig. 5.15: Unit cell structures of (a) Y_2SiO_5 and (b) $Y_2Si_2O_7$. The crystal data are taken from Ref. [110] and Ref. [102], respectively.

The O1 site bonds to three yttrium atoms and one silicon atom. Each of O2-O4 sites bonds to two yttrium atoms and one silicon atom. The O5 site bonds to four yttrium atoms.

The space group of $Y_2Si_2O_7$ is (P 2₁/c). One unit cell contains 22 atoms in total. There are 6 inequivalent positions in a unit cell: one yttrium site, one silicon site and four oxygen sites labeled O1-O4. The yttrium site bonds to six oxygen atoms with the bond lengths ranging from 2.250 Å to 2.328 Å. The Si site tetrahedrally bonds to four oxygen atoms (O1-O4) with the bond lengths of 1.631 Å, 1.622 Å, 1.616 Å, and 1.637 Å. The O1 site bonds to two silicon atoms, which connects the two silicon-oxygen tetrahedron. Each of O2-O4 sites bonds to two yttrium atoms and one silicon atom.

In this work, the Si L₂₃ and O K edges of both yttrium silicates have been calculated by the Ab-Initio FMS code Feff8.20 [80]. All the FMS calculations are performed in a sufficiently large cluster with a radius of 7.1 Å which contains 115 atoms. The convergence of the calculations has been verified by calculating the near-edge structures shell by shell. The silicon L₃ and L₂ edges result from the electron transitions from the 2P_{3/2} and 2P_{1/2} states to the unoccupied density of states above the Fermi energy, respectively. Due to the small energy splitting (about 1.0 eV) and the spectral broadening, the silicon L₃ and L₂ edges are strongly overlapped. In the FMS calculations of the Si L₂₃ edges, the L₃ and L₂ edges were individually calculated with the core-hole effect. They were weighted by the corresponding number of states (L₃:4, L₂:2). The summation of the weighted L₃ and L₂ edges were used to compare with the experimental spectrum. The comparison is given in Fig. 5.16(a). The calculated spectra have been broadened by 0.4 eV to simulate the instrumental broadening. One can see that the calculated Si L₂₃ edges of Y_2SiO_5 and $Y_2Si_2O_7$ are fairly

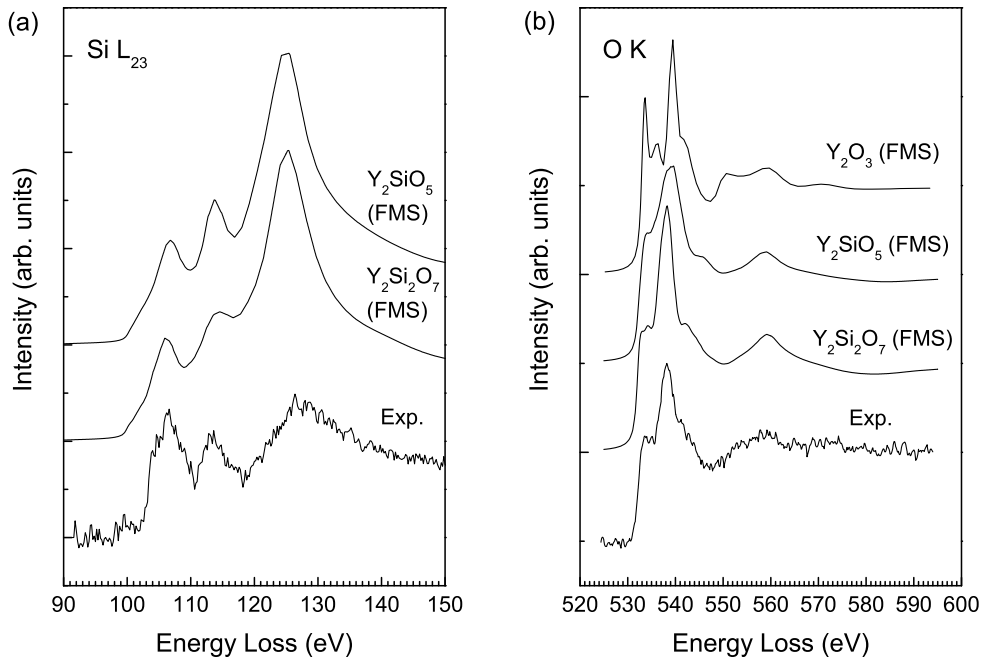


Fig. 5.16: Si L_{23} edges (a) and O K edge (b) of yttrium silicates simulated by the FMS method (Feff8.20) in comparison with experimental spectra acquired from the intermediate layer between the deposited Y_2O_3 film and the interfacial SiO_2 layer.

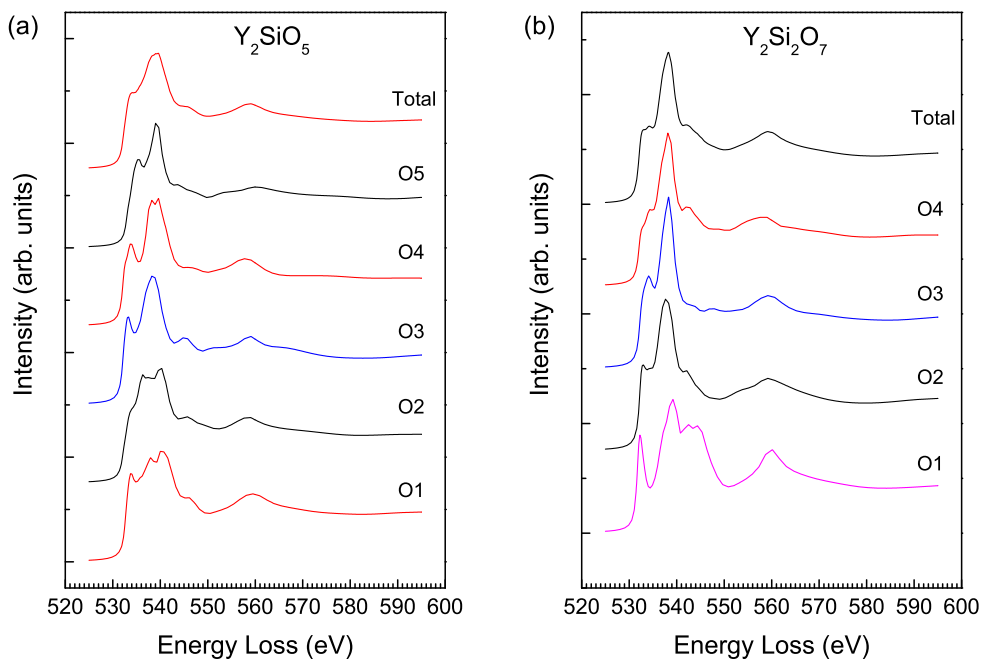


Fig. 5.17: The K edge of each inequivalent oxygen in (a) Y_2SiO_5 and (b) $Y_2Si_2O_7$.

well consistent with the EEL spectrum acquired from the intermediate layer between the deposited Y_2O_3 film and the interfacial SiO_2 layer.

As described above, there are five inequivalent oxygen sites (labeled O1-O5) in Y_2SiO_5 and four (labeled O1-O4) in $Y_2Si_2O_7$. In the FMS calculations, the K edge of each inequivalent oxygen site has been individually calculated with a 0.4 eV broadening, as shown in Fig. 5.17. Then they are weighed by the corresponding number of atoms in the unit cell. The summation of the oxygen K edges is used to compare with the EEL spectrum taken from the intermediate layer. The comparison is given in Fig. 5.16(b). The calculated oxygen K edge of bulk Y_2O_3 is given for comparison. The details of the FMS calculations of bulk Y_2O_3 will be given later. The experimental spectrum is revealed to be very close to the theoretical spectrum of $Y_2Si_2O_7$. This is very likely to mean that the chemical compositions of the intermediate layer are mainly dominated by $Y_2Si_2O_7$ due to a lower synthesis energy. In fact, the synthesis of crystalline $Y_2Si_2O_7$ has been achieved at a temperature as low as 365°C [111].

5.6 Ab-Initio Calculations of Y_2O_3

The partial density of states of Y_2O_3 has been calculated in comparison with the EEL spectrum. Prior to the calculations of the partial density of states, atomic positions in the unit cell were optimized by minimizing the total energy of the unit cell. The optimized crystal data are given in Table 5.2. As shown in Fig. 5.18, the bulk Y_2O_3 has a bixbyite structure with the space group $Ia\bar{3}(206)$. There are two inequivalent positions for yttrium atoms, labeled Y1 and Y2, respectively. Y1 sites are surrounded by six oxygen atoms in a strongly distorted octahedral symmetry. The lattice parameters of bulk Y_2O_3 were taken from the Ref. [112]. The Y1-O bond lengths are in the range of 2.225–2.323 Å. The Y2 sites are also surrounded by six oxygen atoms but in a slightly distorted octahedral symmetry. The O-Y2-O angles are 80.2° and 99.8°. The Y2-O bond lengths have an equal value, 2.294 Å. The crystal structure of Y_2O_3 is fairly complicated. One unit cell contains 80 atoms in total including 24 Y1, 8 Y2, and 48 oxygen atoms.

In band structure calculations, 1000 k-points were taken into account in the irreducible Brillouin zone. The local density of states of the Y1, Y2 and O sites are summarized in Fig.

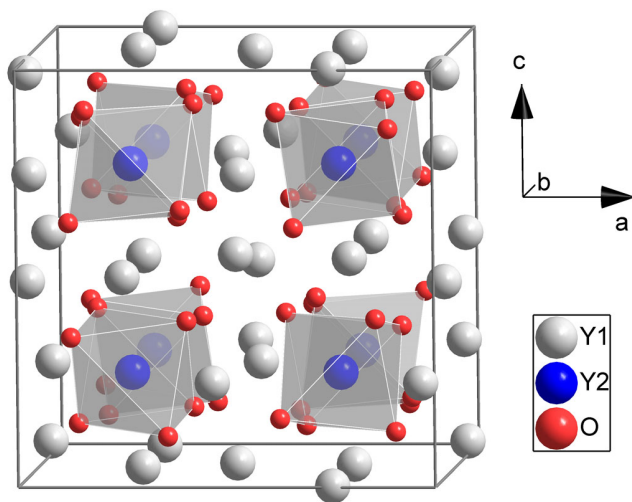


Fig. 5.18: Unit cell structure of bulk Y_2O_3 . The two inequivalent positions for yttrium atoms are labeled Y1 and Y2.

Table 5.2: Optimized crystal structure data of bulk Y_2O_3 by minimizing the total energy of the unit cell. The crystal data were originally taken from Ref. [112]. The lattice parameter is $a=10.604 \text{ \AA}$. The muffin-tin radii R_{MT} used in the FLAPW calculations are given in units of the Bohr radius.

	x	y	z	R_{MT}
Y1	0.9668	0.0	1/4	2.2
Y2	1/4	1/4	1/4	2.2
O	0.3907	0.1522	0.3802	2.0

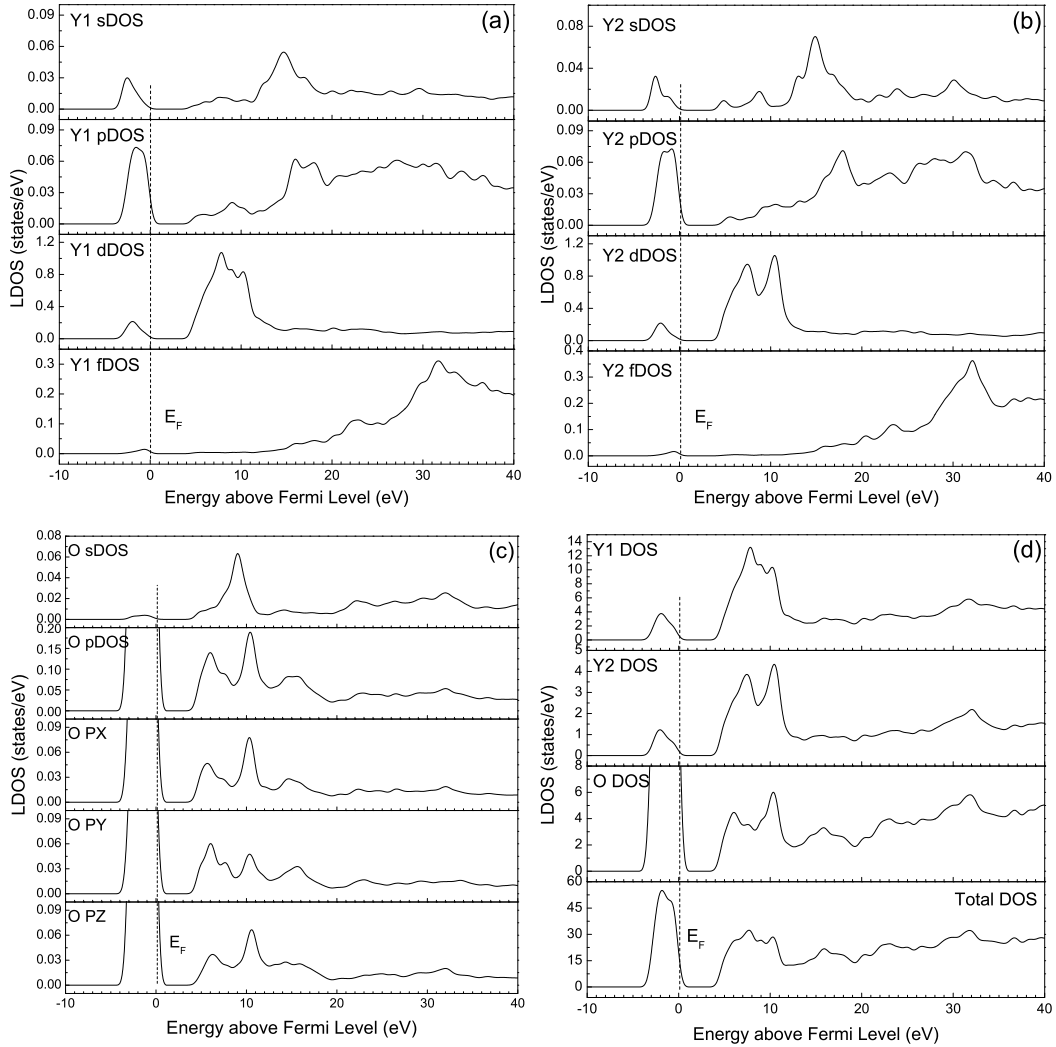


Fig. 5.19: Partial density of states of (a) Y1, (b) Y2 and (c) O calculated by the FLAPW method in Y_2O_3 . The total density of states are given in (d).

5.19(a), (b) and (c), respectively. The total density of states is given in Fig. 5.19(d). The calculated band gap of bulk Y_2O_3 is about 5.0 eV, which is a little less than the experimental value of 5.6 eV [113] due to the one-electron approximation in the DFT method. In spite of the band structure method usually gives the higher accuracy with respect to the FMS method, the relationship between the fine structures and the crystal structure can not be given directly. For this reason, the FMS calculations of Y_2O_3 have been performed for the Y M_5 and O K edges.

5.6.1 Y M_{45} Edges

Band-Structure Method

The electron configuration of yttrium is $1s^2 2s^2 2p^6 3s^2 3p^6 3d^{10} 4s^2 4p^6 5d^1 6s^2$. In Y_2O_3 , the three $5d^1 6s^2$ valence orbitals are hybridized to bond with the six oxygen atoms. According to the dipole-selection rule, the Y M_{45} edges arise from the $3d \rightarrow 4f$ transition. In comparison with the EEL spectrum of Y M_{45} edges acquired from the deposited Y_2O_3 film, the unoccupied yttrium f DOS is shown in Fig. 5.20. The Y1 and Y2 f DOS have been broadened by 0.4 eV to simulate the intrinsic and instrumental broadenings. The total yttrium f DOS is composed by summing up the contributions of Y1 and Y2 atoms, weighted by the corresponding number of atoms (Y1:Y2=3:1) in the unit cell. The main features are labeled A, B, C, and D. One can see that the total yttrium f DOS is fairly well consistent with the experimental Y M_{45} edges. The slightly increased intensity of peak B in the EEL spectra might be related to the presence of oxygen vacancies in the Y_2O_3 film. Peaks C and D of Y1 f DOS are much broader than those of Y2 DOS due to the stronger distortion of the oxygen coordination (cf. Fig. 5.19(a) and (b)). The pre-edge of Y f DOS in the range of 5-15 eV has been magnified in the inset. Some weak features are found, and the theoretical f DOS is in a good agreement with the ELNES spectrum. This part of spectrum may be important in view of dielectric properties of deposited Y_2O_3 film since it is close to the Fermi level.

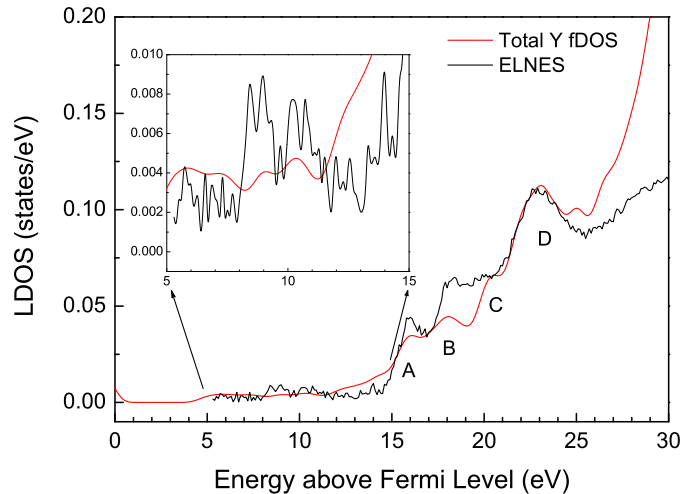


Fig. 5.20: Comparison between the calculated yttrium f DOS and the ELNES of the yttrium M_{45} edges acquired from the deposited Y_2O_3 film. The main features are labeled A, B, C, and D. The magnified pre-edge (5-15 eV) of the yttrium M_{45} edges is shown in the inset.

FMS Method

In order to associate the fine structures of the Y M_{45} edges with the crystal structure, full multiple-scattering calculations need to be performed. FMS calculations for the core-loss edges of the M series have been scarcely reported, because the atom-size effect usually leads to a bad accuracy. In this work, the Y M_{45} edges have been calculated by the Feff8.20 code which is based on the curved-wave theory [34], in which the effect of the atom size has been taken into account. Due to the distortion of the oxygen octahedron around the Y2 site, which is much smaller than that of the Y1 site, the crystal structure analysis by the Y2 M_{45} edges is a little easier. The Y2 M_5 edge is calculated in the shell-by-shell model. For the M_4 edge, the fine structures are same as the M_5 edge except a small shift towards higher energy. The FMS calculations have been performed up to five shells around the Y2 atom. The five FMS shells containing 37 atoms are sketched in Fig. 5.21. The definitions of the five shells are described as follows. The first shell contains six nearest-neighbor oxygen atoms. The six oxygen atoms are octahedrally coordinated around the Y2 site. The distance from this shell to the central Y2 atom is 2.294 Å. The second shell contains 6 yttrium atoms in the (111) plane. Each yttrium bonds to two oxygen atoms of the first shell. This means that the Y-O bonding in the (111) plane is a little stronger than in other planes. This is the reason why the growth direction is usually along the [111] direction. The distance from the second shell to the central Y2 atom is 3.512 Å. The third shell also contains six yttrium atoms. Each yttrium atom bonds to one oxygen atom of the first shell. The distance from this shell to the central yttrium atom is 4.003 Å. The fourth shell contains six oxygen atoms with a distance of 4.190 Å to the central atom. The fifth shell contains 12 oxygen atoms, among them six oxygen atoms with a distance of 4.30 Å and the other with a distance of 4.735 Å to the central yttrium atom.

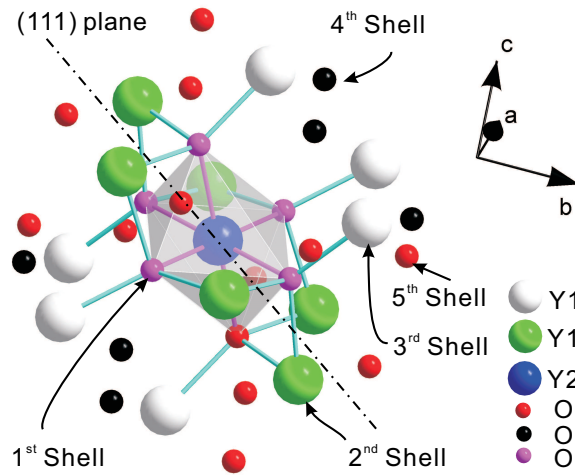


Fig. 5.21: (The definitions of the five-shell cluster containing 37 atoms around the Y2 site.

The calculated results are given in Fig. 5.22. The features are labeled A-F which have been defined in Fig. 5.8. The FMS calculations are summarized in the following. Peak A and the strongest peak F are well reproduced in the 7-atom spectrum. These two peaks are related to the nearest-neighbor oxygen atoms, i.e., the Y-O chemical bonding. Peaks B and C relate to the backscattering at the fifth shell. As mentioned above, the fifth shell contains two subshells. One subshell has a distance of 4.30 Å and the other one has the distance of 4.735 Å to the central atom. The two subshells correspond to the splitting of peaks B and C. Peak D is mainly related to the backscattering at the third shell. The Y2-Y1 interaction

is normal to the (111) plane. A small part of peak D arises from the backscattering at the second shell. The six yttrium atoms are lying in the (111) plane. It indicates that the Y2-Y1 interaction in the (111) plane is weak due to the screening of the strong Y-O interaction in this plane. Peak E is related to the backscattering at the fourth shell.

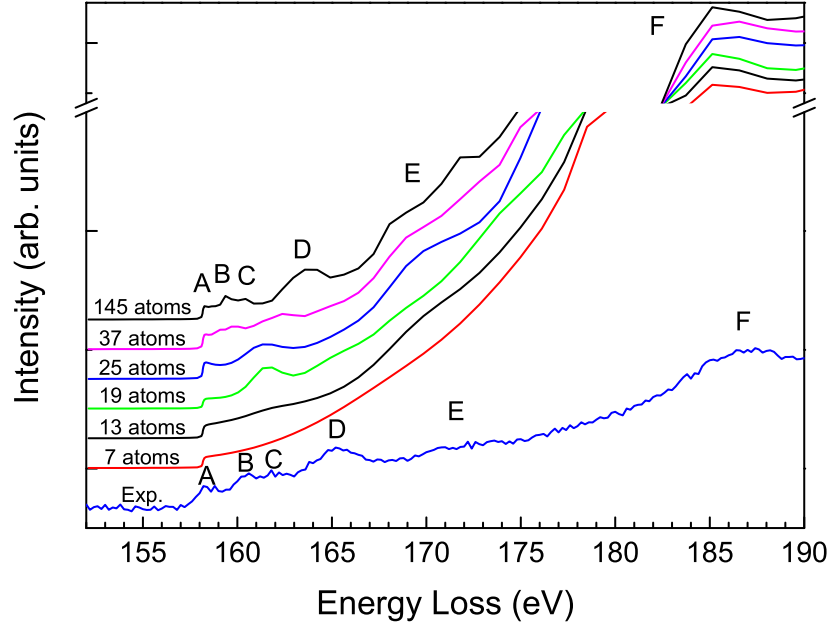


Fig. 5.22: $Y_2 M_5$ edge calculated by the FMS method in the shell-by-shell model. The label of spectrum indicates the total number of atoms in the FMS cluster.

5.6.2 O K Edge

Band-Structure Method

Fig. 5.23 shows the calculated oxygen p DOS together with the experimental spectra taken from the deposited Y_2O_3 film in this work and the stoichiometric bulk Y_2O_3 redrawn from Ref. [16]. The calculated p DOS has been broadened by 0.4 eV for taking into account intrinsic and instrumental broadenings. The spectra have been aligned at the peak B. The theoretical oxygen p DOS is excellently consistent with the experimental spectra even with the very weak peak A'. Peaks A and B correspond to the t_{2g} and e_g orbitals of the yttrium atoms. According to the orientation-projected DOS of oxygen in Fig. 5.19(c), the oxygen p DOS is not isotropic in the X, Y, and Z directions. Peak A in the PY DOS is slightly stronger than in the PX and PZ DOS. Peak A' is a little stronger in the PY DOS. Peak B is stronger in the PX and PZ DOS than in the PZ DOS. Peak B' is slightly stronger in the PY DOS. Due to the different orientations of the oxygen octahedra in bulk Y_2O_3 , the features A-E are present in all the PX, PY, and PZ DOS. The well separated t_{2g} and e_g orbitals can be seen in the Y2 d DOS because the Y2 atom is lying in the center of the nearly perfect oxygen octahedron. In the Y1 d DOS, this separation is slightly smeared out by the strong distortion of the oxygen octahedron. Peaks A' and B' correspond to the energy splitting induced by the distortion of the oxygen octahedron.

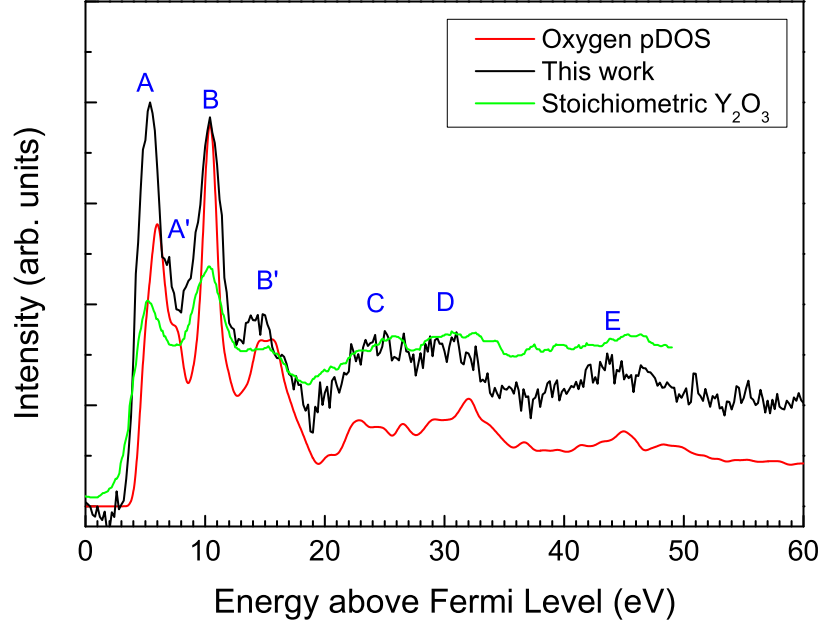


Fig. 5.23: Comparison between ground state oxygen p DOS, ELNES of the oxygen K edge in the deposited Y_2O_3 film and stoichiometric bulk Y_2O_3 redrawn from Ref. [16].

FMS Method

The oxygen K edge has been also calculated by the FMS method in the shell-by-shell model. In this work, the cluster surrounding the oxygen atom with a radius of 5.0 Å has been divided into four shells. The atomic structure of FMS shells is not sketched here due to the difficult separation. The definition of the shells is described as follows. The first shell contains three Y1 and one Y2 atoms which are tetrahedrally coordinating around the oxygen atom. The distance from this shell to the central oxygen atom is varying from 2.225 Å to 2.323 Å. The second shell contains 12 oxygen atoms with a distance range of 2.903-3.889 Å. The third shell contains 12 yttrium atoms with the distance from 4.019 Å to 4.976 Å. The fourth shell contains 9 oxygen atoms with a distance range of 4.285-4.858 Å to the central oxygen atom.

In comparison with the oxygen p DOS, the FMS calculation results are given in Fig. 5.24. The oxygen p DOS has been aligned at the peak B. All of the fine structures are well reproduced in the 38-atom cluster. The degenerated peaks A-A', B-B' and C-D are already reproduced in the 5-atom cluster. These degenerated peaks are split into two peaks in the crystal field of the second shell (12 oxygen atoms). Peaks A and B are attributed to the tetrahedral environment of the oxygen atoms. That is the reason why the oxygen K edge structures of Sc_2O_3 and La_2O_3 are similar to that of Y_2O_3 [114]. The two peaks are caused by the $2p - 4d$ hybridization between the O and Y atoms. Peak A corresponds to the t_{2g} orbitals which point to the center of the tetrahedral surfaces. Peak B is related to the e_g orbitals which point to the ligand yttrium atoms. Since the four surrounding yttrium atoms are inequivalent in the multiple scattering model, the t_{2g} and e_g orbitals split into two components corresponding to peaks A-A' and B-B'. The splitting of e_g orbitals is much stronger than that of the t_{2g} orbitals. Peak E dominantly arises from the backscattering at the fourth shell.

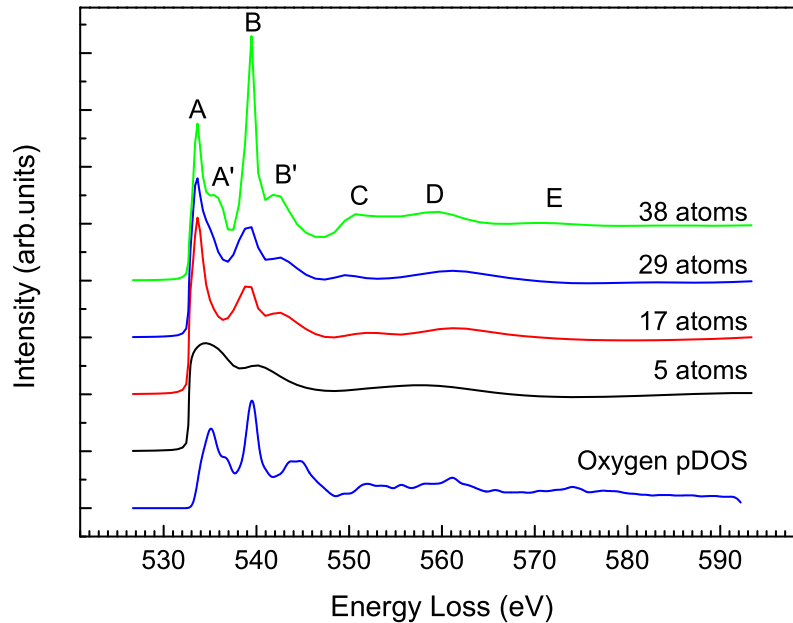


Fig. 5.24: The results of FMS calculations in the shell-by-shell model.

5.7 Summary

The fine structures of the Y M_{45} , Si L_{23} and O K edges have been investigated across the $Y_2O_3/SiO_x/Si$ interfaces by high-resolution EELS. The interfacial SiO_x layer between the deposited Y_2O_3 film and the silicon substrate is nearly pure amorphous SiO_2 . This SiO_2 layer is attributed to native SiO_2 formed at the initial stage of deposition. In the region close to the SiO_2/Si interface, small contribution of silicon is detected. It has been assigned to the diffusion of silicon from the silicon substrate during the deposition. An intermediate layer between the deposited Y_2O_3 film and the interfacial SiO_2 layer has been found in the HRTEM image. The chemical compositions of this intermediate layer are revealed to be yttrium silicates. The formation of yttrium silicates in the intermediate layer has been interpreted by the direct chemical reactions between the deposited Y_2O_3 film and the interfacial SiO_2 layer during deposition. Chemical reactions between the Y_2O_3 film and the interfacial SiO_2 layer are found to be induced by the electron beam irradiation. According to the EELS and HRTEM results, it is revealed that the interface SiO_2 can diffuse into the Y_2O_3 film to form yttrium silicates under the influence of the electron beam. The interfacial SiO_2 layer is reconstructed into silicon after the beam irradiation. The formation of yttrium silicates is confirmed by the FMS calculations of the Si L_{23} and O K edges. Additionally, in comparison with the reference spectrum from bulk Y_2O_3 , the as-deposited Y_2O_3 film is oxygen deficient.

The interpretations of these fine structures have been given according to Ab-Initio calculations. In the Ab-Initio calculations, the combination of the band-structure method and the full multiple-scattering method has been performed to give clear interpretations for these fine structures. Both the band-structure calculations and the FMS calculations are in excellent agreement with the ELNES of the core-level edges. The relationship between the fine structures and the crystal structure has been revealed by comparing theoretical and experimental results. In general, the lower-energy region in the EEL spectrum of the oxide compounds is dominated by the chemical bonding along with the cation-anion orbital hybridization. The higher-energy region in the ELNES is dominated by the oxygen-oxygen interactions. For the

oxygen K edge, the ground-state partial density of states is in excellent consistency with the ELNES up to at least 40 eV above the Fermi level. The core-hole effect is strongly screened by the valence electrons. Moreover, the ground state yttrium f DOS shows a fairly good agreement with the ELNES of the Y M_{45} edges. This result means that the core-hole effect of the Y M_{45} edges can also be neglected. FMS calculations for the Y M_{45} edges have been accomplished, and a good agreement with the ELNES spectrum is obtained.

Moreover, according to theoretical calculations, the Y-O interactions in the (111) plane are revealed to be stronger than in the other planes. This finding gives a reasonable explanation of the generally reported [111] growth direction with a native SiO_2 layer presented in the initial stage of the deposition. However, the [110] growth direction should be related to the lattice matching when the native SiO_2 layer is absent.

In principle, Ab-Initio calculations of reduced Y_2O_3 can be performed. Due to the high density of the oxygen vacancies in reduced Y_2O_3 , several oxygen vacancies may be present in one unit cell. The relaxation of the atomic structure can be done by minimizing the atomic force acting on each atom. However, due to the complexity of the of Y_2O_3 unit cell, the introduction of one oxygen vacancy will reduce the space group from (I A 3) to (P 1). That causes plenty of inequivalent positions, which makes the accurate Ab-Initio calculations very time-consuming. Otherwise, several oxygen vacancies have to be introduced into one unit cell of Y_2O_3 when the density of oxygen vacancies is high. For example, five oxygen vacancies need to be introduced for modeling the 10%-oxygen-reduced sample. There are lot of choices to build the atomic model for the reduced Y_2O_3 . The computational bottleneck is mainly caused by the optimization of the oxygen vacancy structure. Molecular dynamics calculations might be helpful to overcome the computational bottleneck by semi-empirical potentials [106, 115], but the accuracy will be sacrificed.

Chapter 6

Summary and Conclusion

Ferroelectric thin films ($\text{BaTiO}_3/\text{SrTiO}_3$ multilayers and $\text{Y}_2\text{O}_3/\text{Si}$ films) have been investigated by high-resolution electron energy-loss spectroscopy. The EELS experiments mainly concentrate on the interface between the deposited thin film and the substrate. Various experimental parameters, which have strong effects on the acquisition of reliable electron energy-loss spectra from the interface, were discussed and evaluated. Three Ab-Initio methods (full multiple-scattering, band-structure, and ligand field atomic-multiplet) for the calculation of the energy-loss near edge structures have been compared to show their advantages and shortages. These theoretical methods were combined to give the relationship between the fine structures and the crystal structure. The main experimental and theoretical results are given in the following description.

(1) The effects of various experimental parameters on the electron energy-loss spectra acquired from interfaces have been theoretically and experimentally discussed. The electron beam convergence angle and the orientation of the interface are revealed to be very important for the acquisition of reliable spectra from the interfaces or very thin layers. A large convergence angle and/or incident angle between the electron beam and the interface plane would smear out some fine structures in the high-resolution EEL spectrum. These effects on the EELS fine structures have been estimated by simple models.

(2) The high-resolution EELS has been applied to investigate $\text{BaTiO}_3/\text{SrTiO}_3$ multilayers. The aggregation of oxygen vacancies has been found at the upper interface of the BaTiO_3 layer, which is caused by oxygen vacancy ordering under the influence of misfit strain. This finding proved helpful to interpret the dielectric properties of the $\text{BaTiO}_3/\text{SrTiO}_3$ multilayers. The lower interface of the BaTiO_3 layer is found to be defect free due to the strong misfit strain induced by the lattice mismatch. The crystal-splitting in the Ti L_{23} edges is suggested as an indicator of the strength of the misfit strain at the interface. Moreover, the lattice parameters of the BaTiO_3 thin layer have been determined by selected area diffraction, which confirms the presence of strong misfit strains.

(3) The high- κ gate dielectric $\text{Y}_2\text{O}_3/\text{Si}(001)$ structure has been investigated by the high-resolution EELS and HRTEM. The findings reveal that the chemical composition of the interface layer between the deposited Y_2O_3 film and the silicon substrate is nearly pure amorphous SiO_2 . Evidences for the formation of yttrium silicates at the $\text{Y}_2\text{O}_3/\text{SiO}_2$ interface have been given by the electron energy-loss near edge structures. The formation mechanism of yttrium silicates has been revealed to be caused by direct chemical reactions between the deposited Y_2O_3 film and the interfacial SiO_2 layer. The as-deposited Y_2O_3 film was revealed to be oxygen deficient.

(4) The electron-beam-induced diffusion of interfacial SiO_2 has been found in the $\text{Y}_2\text{O}_3/\text{Si}(001)$ structure. The interfacial SiO_2 was revealed to diffuse into the Y_2O_3 film to form yttrium silicates under the influence of the electron beam irradiation. The diffusion of SiO_2 has been interpreted by the aggregation of the high-density of oxygen vacancies around the electron beam illuminated region. This aggregation makes the rigid $[\text{SiO}_4]^{4-}$ tetrahedra diffuse into the Y_2O_3 film.

(5) The formation of yttrium silicate has been confirmed by the FMS calculations. The Si L_{23} and O K edges of Y_2SiO_5 and $\text{Y}_2\text{Si}_2\text{O}_7$ have been calculated, respectively. The theoretical spectra are consistent with the experimental spectra.

(6) In bulk Y_2O_3 , FMS calculations revealed the Y-O bonding in the (111) plane to be stronger than in other planes, which reduces the surface free energy of this plane and makes the growth easier. This finding gives a reasonable explanation of the generally reported [111] growth direction when a native SiO_2 layer is present in the initial stage of the deposition. The [110] growth direction is explained by the lattice match with the silicon substrate when the native SiO_2 layer is absent at the interface.

(7) According to the full multiple-scattering calculations, the backscattering from oxygen atoms along chemical bonding directions is found to be much stronger than that from the other oxygen atoms. This finding has been found in several oxide compounds, such as SrTiO_3 , BaTiO_3 , and Y_2O_3 , etc., by the shell-by-shell FMS calculations of the oxygen K edge.

(8) The core-loss near edge structures of the rutile TiO_2 , SrTiO_3 , BaTiO_3 , $\alpha\text{-SiO}_2$, $\beta\text{-SiO}_2$, and Y_2O_3 have been simulated by both the full multiple-scattering and band-structure methods. In the former method, shell-by-shell calculations have been performed. Using the latter method, the site-projected partial density of states above the Fermi level have been calculated. The combination of the full multiplet-scattering and band-structure methods has been applied to give a clear relationship between the fine structures of the ELNES spectrum and the crystal structure surrounding the absorbing atom.

(9) In the oxide compounds, the low-energy region of the ELNES spectrum was shown to be dominated by cation-oxygen interactions, and the high-energy region is interpreted by oxygen-oxygen interactions. The Ab-Initio calculations reveal that the core-hole effect on the oxygen K edge is neglectable due to the screen of valence electrons.

Bibliography

- [1] A. Visinoiu, R. Scholz, S. Chattopadhyay, M. Alexe, and D. Hesse. Formation of epitaxial BaTiO₃/SrTiO₃ multilayers grown on Nb-doped SrTiO₃ (001) substrates. *Jpn. J. Appl. Phys.*, 41:6633–6638, 2002.
- [2] A. Visinoiu, M. Alexe, H. N. Lee, D. N. Zakharov, A. Pignolet, D. Hesse, and U. Gösele. Initial growth stages of epitaxial BaTiO₃ films on vicinal SrTiO₃ (001) substrate surfaces. *J. Appl. Phys.*, 91:10157–10162, 2002.
- [3] <http://www.intel.com/design/pentium4/guides/300564.htm>.
- [4] R. Chau, B. Boyanov, B. Doyle, M. Doczy, S. Datta, S. Harelund, B. Jin, J. Kavalieros, and M. Metz. Silicon nano-transistors for logic applications. *Physica E: Low-dimensional Systems and Nanostructures*, 19:1–5, 2003.
- [5] H. N. Lee, Y. T. Kim, and S. H. Choh. Characteristics of Pt/SrBi₂Ta₂O₉/Y₂O₃/Si ferroelectric gate capacitors. *J. Korean Phys. Soc.*, 34:454, 1999.
- [6] R. J. Gaboriaud, F. Pailloux, P. Guerin, and F. Paumier. Yttrium sesquioxide, Y₂O₃, thin films deposited on Si by ion beam sputtering: microstructure and dielectric properties. *Thin Solid Films*, 400:106–110, 2001.
- [7] G. A. Botton, J. A. Gupta, D. Landheer, J. P. McCaffrey, G. I. Sproule, and M. J. Graham. Electron energy loss spectroscopy of interfacial layer formation in Gd₂O₃ films deposited directly on Si(001). *Appl. Phys.*, 91:2921–2928, 2002.
- [8] S. Stemmer, J.-P. Maria, and A. I. Kingon. Structure and stability of La₂O₃/SiO₂ layers on Si(001). *Appl. Phys. Lett.*, 79:102–104, 2001.
- [9] G. B. Alers, D. J. Werder, Y. Chabal, H. C. Lu, E. P. Gusev, E. Garfunkel, T. Gustafsson, and R. S. Urdahl. Intermixing at the tantalum oxide/silicon interface in gate dielectric structures. *Appl. Phys. Lett.*, 73:1517–1519, 1998.
- [10] R. N. Sharma and A. C. Rastogi. Structure and composition of interfacial silicon oxide layer in chemical vapor deposited Y₂O₃-SiO₂ bilayer dielectrics for metal-insulator-semiconductor devices. *J. Appl. Phys.*, 76:4215–4224, 1994.
- [11] M. Gurvitch, L. Manchanda, and J. M. Gipson. Study of thermally oxidized yttrium films on silicon. *Appl. Phys. Lett.*, 51:919, 1987.
- [12] S. C. Choi, M. H. Cho, S. W. Whangbo, C. N. Whang, C. E. Hong, N. Y. Kim, J. S. Jeon, S. I. Lee, and M. Y. Lee. Heteroepitaxial growth of Y₂O₃ films on Si(100) by reactive ionized cluster beam deposition. *Nuclear Instruments and Methods in Physics Research B*, 121:170–174, 1997.
- [13] S.-K. Kang, D.-H. Ko, E.-H. Kim, M. H. Cho, and C. Whang. Interfacial reactions in the thin film Y₂O₃ on chemically oxidized Si(100) substrate systems. *Thin Solid Films*, 353:8–11, 1999.

-
- [14] D. Niu, R. W. Ashcraft, Z. Chen, S. Stemmer, and G. N. Parsons. Electron energy-loss spectroscopy analysis of interface structure of yttrium oxide gate dielectrics on silicon. *Appl. Phys. Lett.*, 81:676–678, 2002.
- [15] S. Stemmer, D. O. Klenov, Z. Chen, D. Niu, R. W. Ashcraft, and G. N. Parsons. Reactions of Y_2O_3 films with (001) Si substrates and with polycrystalline Si capping layers. *Appl. Phys. Lett.*, 81:712–714, 2002.
- [16] A. Travlos, N. Boukos, G. Apostolopoulos, and A. Dimoulas. Oxygen vacancy ordering in epitaxial layers of yttrium oxide on Si(001). *Applied Physics Letters*, 82:4053–4055, 2003.
- [17] W. Grogger, F. Hofer, B. Kraus, I. Rom, W. Sitte, and P. Warbichler. EFTEM and EELS analysis of a Pt/NiO interface. *Mikrochim. Acta*, 133:125–129, 2000.
- [18] P. Moreau, N. Brun, C. A. Walsh, C. Colliex, and A. Howie. Relativistic effects in electron-energy-loss-spectroscopy observations of the Si/SiO₂ interface plasmon peak. *Phys. Rev. B*, 56:6774, 1997.
- [19] R. Brydson, J. Bruley, H. Müllejans, C. Scheu, and M. Rühle. Modelling the bonding at metal-ceramic interfaces using PEELS in the STEM. *Ultramicroscopy*, 59:81–92, 1995.
- [20] M. Kim, G. Duscher, N. D. Browning, K. Sohlberg, S. T. Pantelides, and S. J. Pennycook. Nonstoichiometry and the electrical activity of grain boundaries in SrTiO₃. *Phys. Rev. Lett.*, 86:4056, 2001.
- [21] S. B. Lee, W. Sigle, and M. Rühle. Investigation of grain boundaries in abnormal grain growth structure of TiO₂-excess BaTiO₃ by TEM and EELS analysis. *Acta Materialia*, 50:2151–2162, 2002.
- [22] S. Stemmer, S. K. Streiffer, N. D. Browning, C. Basceri, and A. I. Kingonbrowning. Grain boundaries in barium strontium titanate thin films: Structure, chemistry and influence on electronic properties. *Interface Science*, 8:209–221, 2000.
- [23] Z. Zhang, W. Sigle, and M. Rühle. Atomic and electronic characterization of the a[100] dislocation core in SrTiO₃. *Phys. Rev. B*, 66:094108, 2002.
- [24] Z. L. Zhang, W. Sigle, W. Kurtz, and M. Rühle. Electronic and atomic structure of a dissociated dislocation in SrTiO₃. *Phys. Rev. B*, 66:214112, 2002.
- [25] L. V. Azároff. Theory of extended fine structure of X-ray absorption edges. *Rev. Mod. Phys.*, 35:1012–1022, 1963.
- [26] H. Fricke. The K-characteristic absorption frequencies for the chemical elements magnesium to chromium. *Phys. Rev.*, 16:202–215, 1920.
- [27] R. de L. Kronig. *Z. Physik*, 70:317–323, 1931.
- [28] R. de L. Kronig. *Z. Physik*, 75:191–210, 1932.
- [29] D. K. Saldin and Y. Ueda. Dipole approximation in electron-energy-loss spectroscopy: L-shell excitations. *Phys. Rev. B*, 66:5100–5109, 1992.
- [30] D. E. Sayers, F. W. Lytle, and E. A. Stern. Point scattering theory of X-ray absorption fine structure. *Advances in X-ray analysis*, 13:248, 1970.
- [31] D. E. Sayers and E. A. Stern. New technique for investigating noncrystalline structures: Fourier analysis of the extended X-ray-absorption fine structure. *Phys. Rev. Lett.*, 27:1204–1207, 1971.

-
- [32] P. A. Lee and J. B. Pendry. Theory of the extended X-ray absorption fine structure. *Phys. Rev. B*, 11:2795–2811, 1975.
- [33] J. B. Pendry. Theory of averaged low energy electron diffraction data. *J. Phys. C: Solid State Phys.*, 5:2567–2578, 1972.
- [34] J. J. Rehr and R. C. Albers. Scattering-matrix formulation of curved-wave multiple-scattering theory: Application to X-ray-absorption fine structures. *Phys. Rev. B*, 41:8139–8149, 1990.
- [35] C. A. Ashley and S. Doniach. Theory of extended X-ray absorption edge fine structure (EXAFS) in crystalline solids. *Phys. Rev. B*, 11:1279, 1975.
- [36] J. J. Rehr and R. C. Albers. Theoretical approaches to X-ray absorption fine structure. *Rev. Mod. Phys.*, 72:621–654, 2000.
- [37] A. L. Ankudinov, B. Ravel, J. J. Rehr, and S. D. Conradson. Real-space multiple-scattering calculation and interpretation of X-ray-absorption near-edge structure. *Phys. Rev. B*, 58:7565–7576, 1998.
- [38] W. L. Schaich. Comment on the theory of extended X-ray-absorption fine structure. *Phys. Rev. B*, 8:4028–4032, 1973.
- [39] P. Hohenberg and W. Kohn. Inhomogeneous electron gas. *Phys. Rev.*, 136:B864, 1964.
- [40] W. Kohn and L. J. Sham. Self-consistent equations including exchange and correlation effects. *Phys. Rev.*, 140:A1133–A1138, 1965.
- [41] K. Ohno, K. Esfarjani, , and Y. Kawazoe. *Computational Materials Science*. Springer, Berlin, 1999.
- [42] P. Blaha, K. Schwarz, G. K. H. Madsen, D. Kvasnicka, and J. Luitz. *WIEN2k, An Augmented Plane Wave + Local Orbitals Program for Calculating Crystal Properties*. Techn. Universität Wien, Austria, 2001.
- [43] J. P. Perdew and Y. Wang. Accurate and simple analytic representation of the electron-gas correlation energy. *Phys. Rev. B*, 45:13244–13249, 1992.
- [44] J. P. Perdew, K. Burke, and M. Ernzerhof. Generalized gradient approximation made simple. *Phys. Rev. Lett.*, 77:3865–3868, 1996.
- [45] R. D. Cowan. *The Theory of Atomic Structure and Spectra*. University of California Press, Berkeley, 1981.
- [46] T. Yamaguchi, S. Shibuya, and S. Sugano. Inner-core excitation spectra of transition-metal compounds: I. p-XPS. *J. Phys. C*, 15:2625–2639, 1982.
- [47] B. T. Thole, G. van der Laan, and G. A. Sawatzky. Strong magnetic dichroism predicted in the $M_{4,5}$ X-ray absorption spectra of magnetic rare-earth materials. *Phys. Rev. Lett.*, 55:2086–2088, 1985.
- [48] G. van der Laan and B. T. Thole. Strong magnetic X-ray dichroism in 2p absorption spectra of 3d transition-metal ions. *Phys. Rev. B*, 43:13401, 1991.
- [49] D. J. Newman and B. K. C. Ng. *Crystal Field Handbook*. Cambridge University Press, Cambridge, 2000.
- [50] A. Mirone and M. Sacchi. Ligand-field atomic-multiplet calculations for arbitrary symmetry. *Phys. Rev. B*, 61:13540–13544, 2000.

-
- [51] F. M. F. de Groot, J. C. Fuggle, B. T. Thole, and G. A. Sawatzky. $L_{2,3}$ X-ray-absorption edges of d^0 compounds: K^+ , Ca^{2+} , Sc^{3+} , and Ti^{4+} in O_h (octahedral) symmetry. *Phys. Rev. B*, 41:928–937, 1990.
- [52] P. H. Bultner. *Point Group Symmetry, Applications, Methods, and Tables*. Plenum, New York, 1981.
- [53] S. C. Abrahams and J. L. Bernstein. Rutile: Normal probability plot analysis and accurate measurement of crystal structure. *J. Chem. Phys.*, 55:3206–3211, 1971.
- [54] F. M. F. de Groot. X-ray absorption and dichroism of transition metals and their compounds. *J. Elect. Spec. Rel. Phenom.*, 67:529–622, 1994.
- [55] F. M. F. de Groot, J. Faber, J. J. M. Michiels, M. T. Czyzyk, M. Abbate, and J. C. Fuggle. Oxygen 1s X-ray absorption of tetravalent titanate oxides: A comparison with single-particle calculations. *Phys. Rev. B*, 48:2074–2080, 1993.
- [56] K. Lie, R. Brydson, and H. Davock. Band structure of TiB_2 : Orientation-dependent EELS near-edge fine structure and the effect of the core hole at the B K edge. *Phys. Rev. B*, 59:5361–5367, 1998.
- [57] M. Nelhiebel, P.-H. Louf, P. Schattschneider, P. Blaha, K. Schwarz, and B. Jouffrey. Theory of orientation-sensitive near-edge fine-structure core-level spectroscopy. *Phys. Rev. B*, 59:12807–12814, 1999.
- [58] C. Hébert-Souche, P.-H. Louf, P. Blaha, M. Nelhiebel, J. Luitz, P. Schattschneider, K. Schwarz, and B. Jouffrey. The orientation-dependent simulation of ELNES. *Ultramicroscopy*, 83:9–16, 2000.
- [59] P. A. van Aken, Z. Y. Wu, F. Langenhorst, and F. Seifert. ELNES spectroscopy and XANES calculations of the O K edge: Orientation dependence and effects of protons in $Mg(OH)_2$. *Phys. Rev. B*, 60:3815–3820, 1999.
- [60] P. Schattschneider, C. Hébert, and B. Jouffrey. Orientation dependence of ionization edges in EELS. *Ultramicroscopy*, 86:343–353, 2001.
- [61] L. A. K. Dominik and R. K. MacCrone. Dielectric relaxation of hopping electrons in reduced rutile, TiO_2 . *Phys. Rev.*, 156:910–913, 1967.
- [62] S. G. Christov. Adiabatic polaron theory of electron hopping in crystals: A reaction-rate approach. *Phys. Rev. B*, 26:6918–6935, 1982.
- [63] C. Zhang, G. Gumbs, and N. Tzoar. Theory of hopping rate of localized charge particles in metals: Electron scattering. *Phys. Rev. B*, 43:1463–1470, 1991.
- [64] R. F. Egerton. *Electron Energy-Loss Spectroscopy in the Electron Microscope (2ed)*. Plenum Press, New York and London, 1996.
- [65] B. Arnold, D. Lohse, H.-D. Bauer, T. Gemming, K. Wetzig, and K. Binder. Surface damages on fib prepared TEM-specimens: Possibilities of avoidance and removal. *Microsc. Microanal.*, 9:140, 2003.
- [66] R. J. Gaboriaud, F. Pailloux, P. Guerin, and F. Paumier. Yttrium oxide thin films, Y_2O_3 , grown by ion beam sputtering on Si. *J. Phys. D: Appl. Phys.*, 33:2884–2889, 2000.
- [67] D. B. Williams and C. B. Carter. *Transmission Electron Microscopy*. Plenum Press, New York, 1996.

-
- [68] C. J. Rossouw, L. J. Allen, S. D. Findlay, and M. P. Oxley. Channelling effects in atomic resolution STEM. *Ultramicroscopy*, 96:299–312, 2003.
- [69] J. F. Scott, M. Alexe, N. D. Zakharov, A. Pignolet, C. Curran, and D. Hesse. Nano-phase sbt-family ferroelectric memory. *Integrated Ferroelectrics*, 21:1–14, 1998.
- [70] D. E. Kotecki, J. D. Baniecki, H. Shen, R. B. Laibowitz, K. L. Saenger, J. J. Lian, T. M. Shaw, S. D. Athavale, C. C. Jr., P. R. Duncombe, M. Gutsche, G. Kunkel, Y. J. Park, Y. Y. Wang, and R. Wise. (Ba,Sr)TiO₃ dielectrics for future stacked-capacitor dram. *IBM J. Res. Develop.*, 43(3):367, 1999.
- [71] Y. Yoneda, K. Sakaue, and H. Terauchi. Dielectric investigation of BaTiO₃ thin-film capacitor. *Jpn. J. Appl. Phys.*, 39:4839–4842, 2000.
- [72] G. M. Meyer, R. J. Nelmes, and J. Hutton. High-resolution (direct space) studies of anharmonic motion associated with the structural phase transition in SrTiO₃. *Ferroelectrics*, 21:461–462, 1978.
- [73] H. T. Evans. The crystal structure of tetragonal barium titanate. *Acta Cryst.*, 4:377, 1951.
- [74] M. E. Lines and A. M. Glass. *Principles and Applications of Ferroelectrics Related Materials*. Oxford, Clarendon, 1977.
- [75] R. D. Leapman and L. A. Grunes. Anomalous L₃ / L₂ white-line ratios in the 3d transition metals. *Phys. Rev. Lett.*, 45:397–401, 1980.
- [76] B. T. Thole and G. van der Laan. Branching ratio in X-ray absorption spectroscopy. *Phys. Rev. B.*, 38:3158–3171, 1988.
- [77] R. H. Buttner and E. N. Maslen. Structural parameters and electron difference density in BaTiO₃. *Acta Cryst. B*, 48:764–769, 1992.
- [78] A. Strecker, U. Salzberger, and J. Mayer. *Prakt. Metallogr.*, 30:482, 1993.
- [79] R. Door and D. Gängler. Multiple least-squares fitting for quantitative electron energy-loss spectroscopy an experimental investigation using standard specimens. *Ultramicroscopy*, 58:197–210, 1995.
- [80] A. L. Ankudinov, C. E. Bouldin, J. J. Rehr, J. Sims, and H. Hung. Parallel calculation of electron multiple scattering using lanczos algorithms. *Phys. Rev. B*, 65:104107, 2002.
- [81] R. D. Leapman, L. A. Grunes, and P. L. Fejes. Study of the l₂₃ edges in the 3d transition metals and their oxides by electron-energy-loss spectroscopy with comparisons to theory. *Phys. Rev. B*, 26:614–635, 1982.
- [82] K. Okada and A. Kotani. Theory of core level X-ray photoemission and photoabsorption in Ti compounds. *J. Elect. Spec. Rel. Phenom.*, 62:131–140, 1993.
- [83] C. R. Natoli, M. Benfatto, C. Brouder, M. F. R. López, and D. L. Foulis. Multichannel multiple-scattering theory with general potentials. *Phys. Rev. B*, 42:1944–1968, 1990.
- [84] F. M. F. de Groot, M. Grioni, J. C. Fuggle, J. Ghijsen, G. A. Sawatzky, and H. Petersen. Oxygen 1s X-ray-absorption edges of transition-metal oxides. *Phys. Rev. B*, 40:5715–5723, 1989.
- [85] J. V. Mantese, N. W. Schubring, A. L. Micheli, and A. B. Catalan. Ferroelectric thin films with polarization gradients normal to the growth surface. *Appl. Phys. Lett.*, 67:721–723, 1995.

-
- [86] I. Levin, R. D. Leapman, and D. L. Kaiser. Microstructure and chemistry of non-stoichiometric (Ba,Sr)TiO₃ thin films deposited by metalorganic chemical vapor deposition. *J. Mater. Res.*, 15:1433–1436, 2000.
- [87] R. Klie, Y. Ito, S. Stemmer, and N. Browning. Observation of oxygen vacancy ordering and segregation in perovskite oxides. *Ultramicroscopy*, 86:289–302, 2001.
- [88] J. F. Scott and M. Dawber. Oxygen-vacancy ordering as a fatigue mechanism in perovskite ferroelectrics. *Appl. Phys. Lett.*, 76:3801, 2000.
- [89] M. Arai, S. Kohiki, H. Yoshikawa, S. Fukushima, Y. Waseda, and M. Oku. Photoelectron energy-loss functions of SrTiO₃, BaTiO₃, and TiO₂: Theory and experiment. *Phys. Rev. B*, 65:085101, 2002.
- [90] S. C. Choi, M. H. Cho, S. W. Whangbo, C. N. Whang, S. B. Kang, S. I. Lee, and M. Y. Lee. Epitaxial growth of Y₂O₃ films on Si(100) without an interfacial oxide layer. *Appl. Phys. Lett.*, 71:903–905, 1997.
- [91] D.-G. Lim, D.-J. Kwak, and J. Yi. Improved interface properties of yttrium oxide buffer layer on silicon substrate for ferroelectric random access memory applications. *Thin Solid Films*, 422:150–154, 2002.
- [92] A. Dimoulas, G. Vellianitis, A. Travlos, V. Ioannou-Souglерidis, and A. G. Nasiopoulou. Structural and electrical quality of the high- κ dielectric Y₂O₃ on Si(001): Dependence on growth parameters. *J. Appl. Phys.*, 92:426–431, 2002.
- [93] P. L. Hansen, R. Brydson, and D. W. McComb. p \rightarrow p-like transitions at the silicon L_{2,3}-edges of silicates. *Microscopy Microanalysis Microstructures*, 3:213–219, 1992.
- [94] X. W. Lin, Y. Y. Wang, and V. P. Dravid. Valence states and hybridization in vanadium oxide systems investigated by transmission electron-energy-loss spectroscopy. *Phys. Rev. B*, 47:3477–3481, 1993.
- [95] P. E. Batson. Atomic resolution analytical microscopy. *IBM J. Res. Develop.*, 44:477–487, 2000.
- [96] L. A. J. Garvie, P. Rez, J. R. Alvarez, P. R. Busech, A. J. Craven, and R. Brydson. Bonding in alpha-quartz (SiO₂): A view of the unoccupied states. *American Mineralogist*, 85:732–738, 2000.
- [97] R. J. Angel, D. R. Allan, R. Miletich, and L. W. Finger. The use of quartz as an internal pressure standard in high-pressure crystallography. *J. Appl. Cryst.*, 30:461–466, 1997.
- [98] F. Liu and S. H. Garofalini. First-principles study of crystalline silica. *Phys. Rev. B*, 49:12528–12534, 1994.
- [99] N. R. Keskar and J. R. Chelikowsky. Structural properties of nine silica polymorphs. *Phys. Rev. B*, 46:1–13, 1992.
- [100] M. T. Dove, A. P. Giddy, and V. Heine. Rigid unit mode model of displacive phase transitions in framework silicates. *Trans. Amer. Cryst. Assoc.*, 27:65–74, 1993.
- [101] J. Liang, A. Navrotsky, T. Ludwig, H. Seifert, and F. Aldinger. Enthalpy of formation of rare-earth silicates Y₂SiO₅ and Yb₂SiO₅ and N-containing silicate Y₁₀(SiO₄)⁶N₂. *J. Mater. Res.*, 14:1181–1185, 1999.
- [102] N. I. Leonyuk, E. L. Belokoneva, G. Bocelli, L. Righi, E. V. Shvanskii, R. V. Henrykhson, N. V. Kulman, and D. E. Kozhbahteeva. Crystal growth and structural refinements of the Y₂SiO₅, Y₂Si₂O₇ and LaBSiO₅ single crystals. *Cryst. Res. Technol.*, 34:1175–1182, 1999.

-
- [103] M. Copel, M. Gribelyuk, and E. Gusev. Characterization of silicate/Si(001) interfaces. *Applied Physics Letters*, 81:4227–4229, 2002.
- [104] F. Jollet, C. Noguera, N. Thromat, M. Gautier, and J. P. Duraud. Electronic structure of yttrium oxide. *Phys. Rev. B*, 42:7587–7595, 1990.
- [105] F. Jollet, C. Noguera, M. Gautier, N. Thromat, and J. P. Duraud. *J. Am. Ceram. Soc.*, 74:358, 1991.
- [106] L. J. Alvarez, M. A. S. Miguel, and J. A. Odriozola. Effects of nonstoichiometry in the melting process of Y_2O_3 from molecular dynamics simulations. *Phy. Rev. B*, 59:11303–11307, 1999.
- [107] F. Paumier and R. J. Gaboriaud. Interfacial reactions in Y_2O_3 thin films deposited on Si(100). *Thin Solid Films*, 441:307–310, 2003.
- [108] N. I. Leonyuk, E. L. Belokoneva, G. Bocelli, L. Righi, E. V. Shvanskii, R. V. Henrykhson, N. V. Kulman, and D. E. Kozhbakhteeva. High-temperature crystallization and X-ray characterization of Y_2SiO_5 , $Y_2Si_2O_7$ and $LaBSiO_5$. *J. Cryst. Growth*, 205:361–367, 1999.
- [109] W. Y. Ching, L. Ouyang, and Y.-N. Xu. Electronic and optical properties of Y_2SiO_5 and $Y_2Si_2O_7$ with comparisons to α - SiO_2 and Y_2O_3 . *Phys. Rev. B*, 67:245108, 2003.
- [110] B. A. Maksimov, V. V. Ilyukhin, Y. A. Kharitonov, and N. V. Belov. Crystal structure of yttrium oxyorthosilicate Y_2SiO_5 , dual function of yttrium. *Kristallografiya*, 15:926–933, 1970.
- [111] A. I. Becerro, M. Naranjo, A. C. Perdigón, and J. M. Trillo. Hydrothermal chemistry of silicates: Low-temperature synthesis of y -yttrium disilicate. *J. Am. Ceram. Soc.*, 86:1592–1594, 2003.
- [112] A. Bartos, K. P. Lieb, M. Uhrmacher, and D. Wiarda. Refinement of atomic positions in bixbyite oxides using perturbed angular correlation spectroscopy. *Acta Cryst. B*, 49:165–169, 1993.
- [113] S. Zhang and R. Xiao. Yttrium oxide films prepared by pulsed laser deposition. *J. Appl. Phys.*, 83:3842–3848, 1998.
- [114] C. C. Ahn and O. L. Krivanek. *EELS Atlas (Gatan Inc.)*. 1983.
- [115] A. B. Belonoshko, G. Gutierrez, R. Ahuja, and B. Johansson. Molecular dynamics simulation of the structure of yttria Y_2O_3 phases using pairwise interactions. *Phys. Rev. B*, 64:184103, 2001.

Acknowledgements

First of all I am grateful to Priv.-Doz. Dr. Hartmut S. Leipner and Prof. Dr. Hans-Reiner Höche for giving me the opportunity to study the interesting EELS technique. I would like to express my special appreciation to Priv.-Doz. Dr. Hartmut S. Leipner, my supervisor, for his constant guidance and encouragement during the past three years. This work was part of the Graduiertenkollog 415 “Defektstrukturbestimmte physikalische Eigenschaften”. I thank the Deutsche Forschungsgemeinschaft for financial support.

I am also grateful to Priv.-Doz. Dr. Dietrich Hesse and his co-workers in the Max-Planck Institute of Microstructure Physics Halle for providing me the fascinating ferroelectric-film specimens and the fruitful discussions on the experimental results. Especially, I would like to thank Dr. Alina Visinoiu for providing me the promising BaTiO₃/SrTiO₃ multilayers, thank Dr. Stephan Senz for his introduction on wafer bonding technique, and thank Dr. Marin Alexe for his discussion on multilayers.

I greatly appreciate Dr. Frank Heyroth and Frank Syrowatka for their great help in the preparation of the STEM specimens and the EELS/STEM experiments. Without them, no experiments could have been done. I would like to thank Dr. Thomas Höche (Leibniz-Institut für Oberflächen-modifizierung, Leipzig) for his fruitful comments on EELS experiments and his careful review of this thesis.

I thank Prof. Dr. Wolfram Hergert and Christian Heiliger for providing me the experimental result of rutile and their fruitful discussions on the theoretical calculations of electron energy-loss near edge structure.

I would like to thank Prof. Rolly J. Gaboriaud and Dr. Fabien Paumier in Université de Poitiers in France for providing the Y₂O₃/Si sample.

Many thanks to all of my colleagues at the Center of Materials Science for their general supports.

Finally, I would like to dedicate this thesis to my parents and my lovely wife Zhaoping Zheng for their love, patience and encouragement.

Curriculum Vitae

Family name: Zhang
Given name: Jingmin
Date of birth: 08.12.1973
Birth Place: Shandong
Nationality: China
Marital status: Married

1981–1986, Elementary school, Shandong, China
1986–1989, Junior high school, Shandong, China
1989–1992, Senior high school, Shandong, China
1992–1996, Bachelor study of physics, Wuhan University, China
1996–1999, Master study of physics at the positron laboratory, Wuhan University, China
Thesis: Microstructures of Segmented Copolymers Studied by Positron Spectroscopy
1999–2001, Network Engineer in CVICSE software corporation, China
2001–present, Ph.D study on electron energy-loss spectroscopy, Martin-Luther-Universität Halle-Wittenberg, Germany
Thesis: Application of Electron Energy-Loss Spectroscopy to Ferroelectric Thin Films

Erklärung

Hiermit erkläre ich an Eides Statt, dass ich die vorliegende Arbeit selbständig und ohne fremde Hilfe verfasst und nur die angegebenen Quellen und Hilfsmittel verwendet habe. Ergebnisse anderer wissenschaftlicher Arbeiten wurden als solche gekennzeichnet. Diese Arbeit wurde bisher weder im In- noch im Ausland in gleicher oder ähnlicher Form in einem Prüfungsverfahren vorgelegt. Ich erkläre hiermit, dass ich mich bis zu dem jetzigen Zeitpunkt noch nie um einen Doktorgrad beworben habe.

Halle (Saale), December 2004

Jingmin Zhang